

# PENNSTATE



## DEPARTMENT OF PHYSICS

PSU LEPS 96/09

### I. FINAL TECHNICAL REPORT

AFOSR GRANT F49620-94-1-0223

April 1, 1994-March 31, 1996

Gerald A. Smith

Principal Investigator

May 31, 1996

## LABORATORY FOR ELEMENTARY PARTICLE SCIENCE

303 OSMOND LABORATORY

UNIVERSITY PARK, PA 16802

DISTRIBUTION STATEMENT 3

Approved for public release

with unlimited distribution

# DISCLAIMER NOTICE



**THIS DOCUMENT IS BEST QUALITY AVAILABLE. THE COPY FURNISHED TO DTIC CONTAINED A SIGNIFICANT NUMBER OF PAGES WHICH DO NOT REPRODUCE LEGIBLY.**

PSU LEPS 96/09

I. FINAL TECHNICAL REPORT

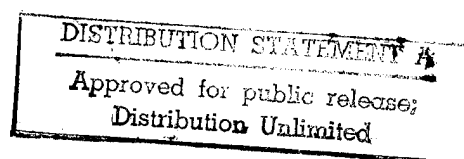
AFOSR GRANT F49620-94-1-0223

April 1, 1994-March 31, 1996

Gerald A. Smith

Principal Investigator

May 31, 1996



# REPORT DOCUMENTATION PAGE

Form Approved

OMB No. 0704-0188

Public reporting burden for this collection of information is estimated to average 1 hour per response, including the time for reviewing instructions, searching existing data sources, gathering and maintaining the data needed, and completing and reviewing the collection of information. Send comments regarding this burden estimate or any other aspect of this collection of information, including suggestions for reducing this burden, to Washington Headquarters Services, Directorate for Information Operations and Reports, 1215 Jefferson Davis Highway, Suite 1204, Arlington, VA 22202-4302, and to the Office of Management and Budget, Paperwork Reduction Project (0704-0188), Washington, DC 20503.

1. AGENCY USE ONLY (Leave blank) 2. REPORT DATE 3. REPORT TYPE AND DATES COVERED  
FINAL REPORT 01 Apr 94 - 31 Mar 96

4. TITLE AND SUBTITLE  
Storage and Transport of Antiprotons  
5. FUNDING NUMBERS  
61102F  
2301/DS

6. AUTHOR(S)  
Professor Gerald Smith

7. PERFORMING ORGANIZATION NAME(S) AND ADDRESS(ES)  
Laboratory for Elementary Particles Science  
Department of Physics  
Pennsylvania State University  
303 Osmond Laboratory  
University Park, PA 16802

AFOSR-TR-96

0297

9. SPONSORING/MONITORING AGENCY NAME(S) AND ADDRESS(ES)  
AFOSR/NE  
110 Duncan Avenue Suite B115  
Bolling AFB DC 20332-0001

10. SPONSORING/MONITORING AGENCY REPORT NUMBER

F49620-94-1-0223

11. SUPPLEMENTARY NOTES

19960618 063

12a. DISTRIBUTION/AVAILABILITY STATEMENT

APPROVED FOR PUBLIC RELEASE: DISTRIBUTION UNLIMITED

12b. DISTRIBUTION CODE

13. ABSTRACT (Maximum 200 words)

The objective of this research is to trap large numbers of antiprotons at CERN and transport them in a portable Penning trap to research sites where they are needed. Accomplishments to date involve the trapping of a million antiprotons, a factor of ten more than previously achieved, cooling of the antiprotons by interaction with electrons, and retaining them in the (non portable) trap for up to one-half hour. A portable Penning trap has been designed and built and is in the final stages of testing prior to use. This trap has been "buttoned up", and external pumping to the trap has resulted in a vacuum of approximately ten-to-the-negative-eighth torr. First cool-down with nitrogen and helium is planned for the very near future, followed by electron and hydrogen storage tests.

DTIC QUALITY INSPECTED 4

14. SUBJECT TERMS

15. NUMBER OF PAGES

16. PRICE CODE

17. SECURITY CLASSIFICATION OF REPORT  
UNCLASSIFIED

18. SECURITY CLASSIFICATION OF THIS PAGE  
UNCLASSIFIED

19. SECURITY CLASSIFICATION OF ABSTRACT  
UNCLASSIFIED

20. LIMITATION OF ABSTRACT

## II. SCIENTIFIC OBJECTIVES AND APPROACH

The objectives of this work are to trap antiprotons in large numbers and transport them to the Phillips Laboratory, Kirtland AFB, NM and deliver them to a target compressed at the SHIVA Star facility. The primary goal is demonstration of antiproton-catalyzed microfission. The approach of this experiment is outlined in three previous publications from our group, found in Appendices I-III.

## III. STATUS OF EFFORT

Trapping of large numbers of antiprotons at CERN during 1994, 1995 and 1996 to date has exceeded our greatest expectations. One million antiprotons have been routinely captured, electron cooled and held for periods of up to one-half hour.

An anomalously low annihilation rate of trapped and cooled antiprotons has been observed. This result has been recently published (Phys. Lett. A214, 279 (1996)), and is found in Appendix IV. The possible implications of this are very important, e.g. at no expense to storage lifetime, portable traps may not require cryogenic surroundings, considerably lessening the cost and size of the trap.

Development of the portable trap is on schedule. The trap has been "buttoned up", and external pumping to the trap has resulted in a vacuum of approximately  $10^{-8}$  torr. First cool-down with nitrogen and helium is planned for the very near future, followed by electron and hydrogen storage tests. Subject to availability of SHIVA Star, injection tests at SHIVA Star with antiprotons would be possible in 1997.

Implosion tests with/without targets done in 1994/5 at SHIVA Star have been very successful. A final set of tests is planned this summer, where especially sensitive components of the injection line will be tested under actual firing conditions.

## IV. ACCOMPLISHMENTS/NEW FINDINGS

### (a) PORTABLE ANTIPROTON TRAP

We have designed a unique, low weight and low cost trap. It is unique because for the first time permanent SmCo magnets will be used in a cold Penning trap. This system is far more robust, i.e. not vulnerable to quenches arising from mechanical forces created during moving operations, than the customary superconducting solenoid used in Penning traps. Although the on-axis field has two zeros, each symmetrically positioned around the geometrical center of the trap, our beam optics computations show that for both injection and ejection antiprotons can be efficiently transported across those zeros. This understanding was made possible by our use of the sophisticated code EGUN, acquired from the Stanford Linear Accelerator Center.

Cryogenic fluids, i.e. liquid nitrogen and helium, are used to maintain high vacuum, i.e. approaching  $10^{-15}$  torr. Because the magnet requires no fluids, the volume is considerably reduced over a conventional Penning trap. The system is designed to require no fluids for at least four days, sufficient for transport over large distances using a small truck or commercial aircraft.

Renderings of the trap are shown in Figures 1 and 2. It is cylindrical in shape, 100 cm tall and 30 cm in diameter. Its weight is 70 kg, so it is readily transported by conventional methods. The cost of the cryosystem and permanent magnets were \$20,000 and \$10,000 respectively. We estimate the final cost of the trap at less than \$60,000. The trap, fully outfitted with all required systems, will be ready for antiproton injection in the Fall.

We are pleased to note that our work has captured national and international attention. An article in the July 15, 1994 issue of Technology Review (Appendix V) briefly mentions our work. The Mutual Broadcasting System radio program "America in the Morning" featured Prof. Smith in a spot in August, 1994. The spot was taped and prepared by the American Association for the Advancement of Science. A feature article appeared in the September 17, 1994 issue of the New Scientist (Appendix VI). We were featured in an article in October, 1995 issue of Discover Magazine. The American Institute of Physics taped an interview for radio airing on Feb. 6 of this year. Finally, we have recently been taped for airing on the BBC TV programs "Future Fantastic" and "Horizons".

#### **(b) RECORD NUMBERS OF ANTIPROTONS TRAPPED AT CERN**

In 1993, in collaboration with Los Alamos National Laboratory, we trapped 720,000 antiprotons from one CERN beam spill. This was a world-record, eclipsing the previous record set by the Harvard group by roughly a factor of seven. For this work, we developed a systematic method of detecting particles in the trap (Appendix VII).

In 1994 we routinely trapped, electron cooled and stored for up to one half-hour 1,000,000 antiprotons. We observed an anomalously low annihilation rate of low energy antiprotons in the trap. With reference to theoretical atomic physics predictions, the data suggest a lower than expected (by at least one order of magnitude) annihilation cross section with residual helium gas in the trap. Also, the annihilation rate does not exhibit the expected dependence with antiproton energy. Thus, the experiment has demonstrated that it is capable of windowing previously unseen atomic physics.

In January, 1995 the CERN management gave PS200 the green light for more than enough beam shots through 1996. They were impressed with the progress we have made, along with the expansion of the collaboration through the addition of groups from Denmark (University of Aarhus), England (University College, London), and

Japan (University of Tokyo).

### **(c) IMPLOSION TESTS AT SHIVA STAR**

The High Energy Plasma Division (J.Degnan et al) started serious solid liner implosion tests in 1994. The first results, without a target at the center of the electrodes, were very successful and published in Physical Review Letters (Appendix VIII). Penn State physicists R.A. Lewis and G.A. Smith are co-authors on this paper.

In 1995 tests were done with copper and aluminum cylindrical targets, prototypes for antiproton microfission injection experiments to be carried out next year. Again, radiographs of the implosion (see Figure 3) were in excellent agreement with predictions from the 2D MHD codes MACH2 (PL) and CALE (Penn State). Penn State graduate student Suman Chakrabarti is responsible for the CALE simulations, and has played a major role in this activity.

### **(d) PREPARATIONS AT PENN STATE FOR PARTICLE INJECTION TESTS AT SHIVA STAR**

Figure 4 shows the antiproton injection test facility at Penn State. It consists of the portable trap, vacuum system, beam transport and proton diagnostic (only protons will be loaded into the trap at Penn State). This apparatus will be moved exactly as it appears to SHIVA Star next year.

Tests with protons will recreate most of the conditions expected with antiprotons at SHIVA Star. A major exception is stray electromagnetic fields from the transmission lines of SHIVA Star. This has been anticipated, by making the beam system from 6 penetration layers (2.3 mm) of copper for high frequency radiation.

After initial cool-down tests, we will inject and store electrons in the trap. This is required for cooling, and will characterize trapping dynamics and induction circuitry used as a diagnostic. We will then turn to proton injection, done by dissociating molecular hydrogen with the electron gun. Electron cooling of protons will then follow. Finally, utilizing three einzel lenses we will test proton extraction to the proton diagnostic. The optics are illustrated in Figure 5. These tests are planned for this Summer.

## **V. PROFESSIONAL PERSONNEL**

Professor Gerald A. Smith (Principal Investigator)

Senior Scientist Raymond L. Lewis

Visiting Professor Michael H. Holzscheiter (on leave from Los Alamos National Laboratory, June 18-Dec.18, 1995 and March 15-May 31, 1996)

Suman Chakrabarti, Ph.D. Graduate Student

## VI. PUBLICATIONS

1. Target Compression by Working Fluids Driven with Solid Liner Implosions, P-R. Chiang et al, J. Appl. Phys. 76 (1994).
2. Neutron Yields for Antiproton Microfission Experiments, C. Gazze et al, Nuclear Science and Engineering, 118, 217 (1994).
3. Containment and Neutron Production by Charged Pions in Antiproton Microfission Experiments, K. Higman et al, Nuclear Science and Engineering 118, 227 (1994).
4. Are Antiprotons Forever?, M. Holzschneider et al, Phys. Lett. A214, 279 (1996).
5. Tank Circuit Model Applied to Particles in a Penning Trap, X. Feng et al, J. Appl. Phys. 79, 8 (1996).

## VII. INTERACTIONS/TRANSITIONS

### (a) Participation/presentations at meetings, conferences, seminars, etc.

1. Colloquium, "Experiments with Trapped Antiprotons", Department of Physics, Brookhaven National Laboratory, February 21, 1995.
2. Seminar, "Experiments with Trapped Antiprotons", Dept. of Physics, Purdue University, April 26, 1995.
3. Seminar, "Experiments with Trapped Antiprotons", Dept. of Physics, University of Arizona, January 30, 1996.

### (b) Consultative and advisory function to other laboratories and agencies, especially Air Force and other DoD laboratories.

1. IPA appointment (paid), Phillips Laboratory, Kirtland AFB, March 1- Aug. 31, 1995 @ 20% of time; 24 days spent at KAFB working on antiproton microfission experiment.
2. Scientific Affiliate, Los Alamos National Laboratory, April 10, 1995-March 31, 1996; consultant on antiproton science.

### (c) Transitions

Potential applications of the portable Penning trap include (1) in situ production of rare radioisotopes for PET scanning at remote hospital sites (2) stimulation of lasing in portable weapons systems (3) portable ion source to medical accelerators for providing simultaneous, high resolution, low radiation scanning of treated areas.



#### **VIII. NEW DISCOVERIES, INVENTIONS OR PATENT DISCLOSURES**

See Appendix IX.

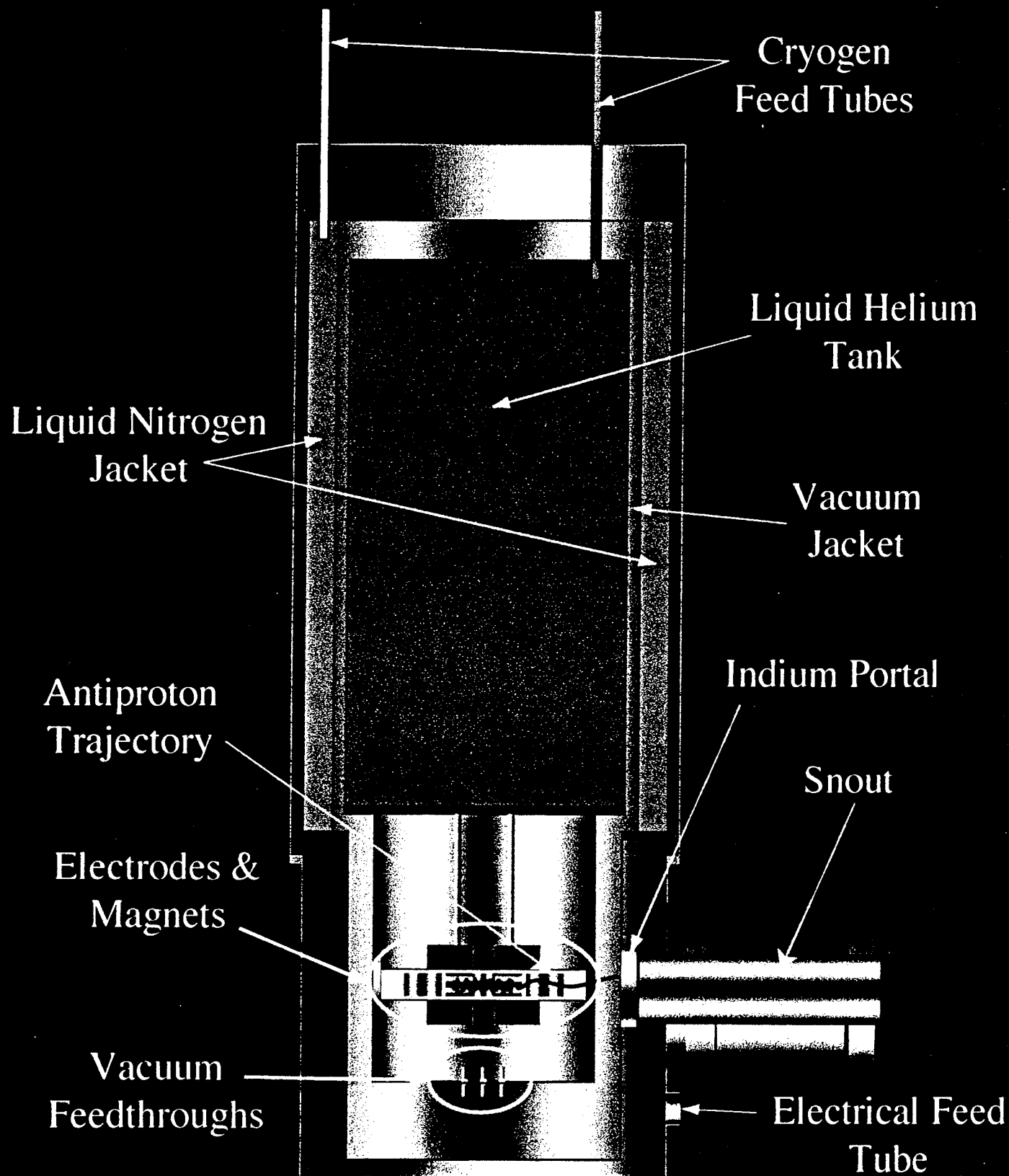
#### **IX. HONORS/AWARDS**

Fellow, American Physical Society

#### **X. ADDITIONAL INFORMATION**

The activities described above also benefit from support from the Jet Propulsion Laboratory (NASA). Additional graduate student support comes from the Penn State Propulsion Research Engineering Center (NASA), the National Science Foundation and the Rocketdyne Division, Rockwell International Corporation. AFOSR funding has been used to leverage significant funding from other sources.

# Portable Penning Trap



Scale 1:5

Laboratory for Elementary Particle Science  
The Pennsylvania State University

Figure 1

# Bottom View of Portable Penning Trap

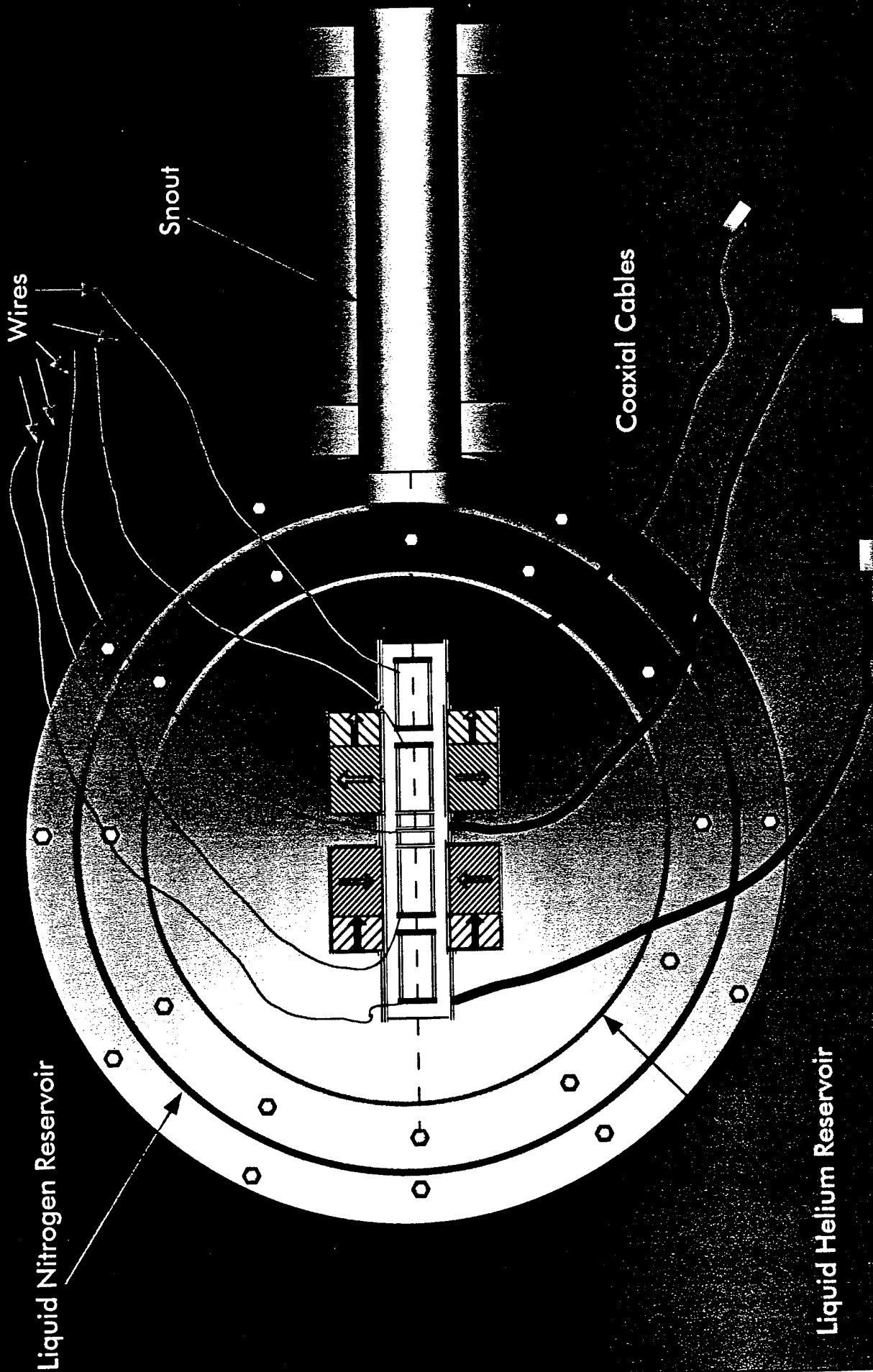


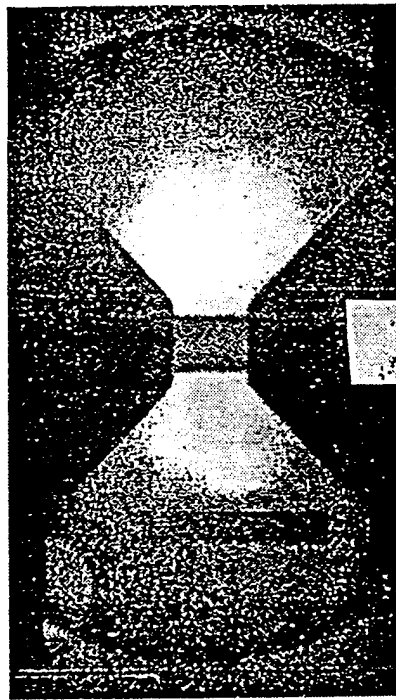
Figure 2

# Radiographs

Experimental

Simulated

Surface  
Contours



0  $\mu$ s



14.0  $\mu$ s



14.3  $\mu$ s

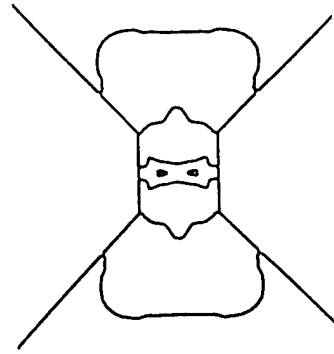
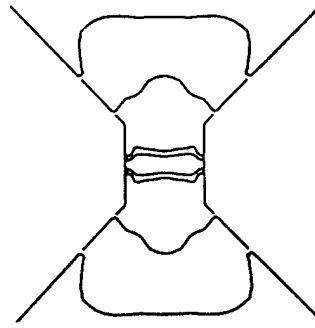


Figure 3

# ANTIPROTON INJECTION SYSTEM TEST FACILITY

JEP  
8/8/95

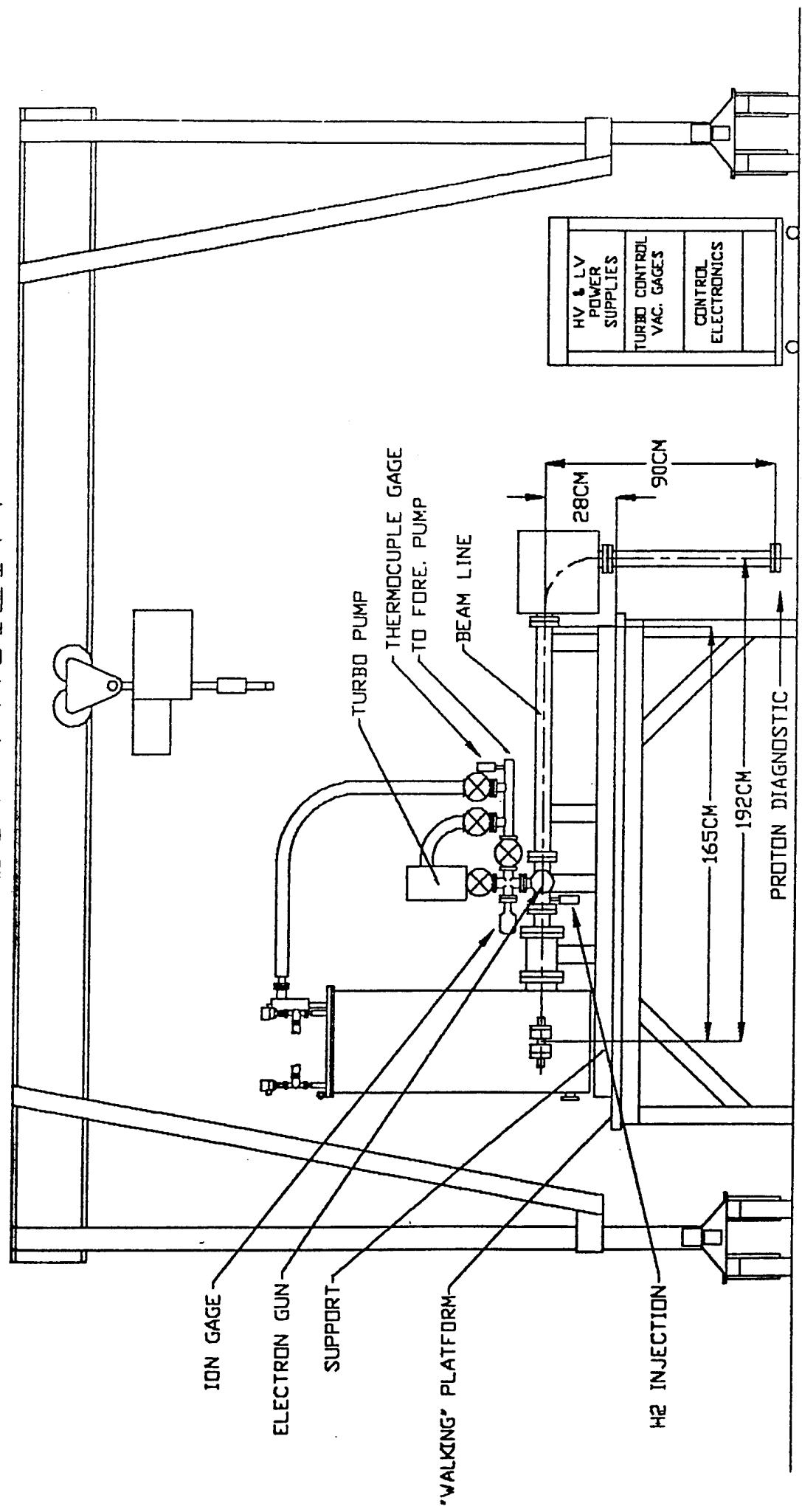
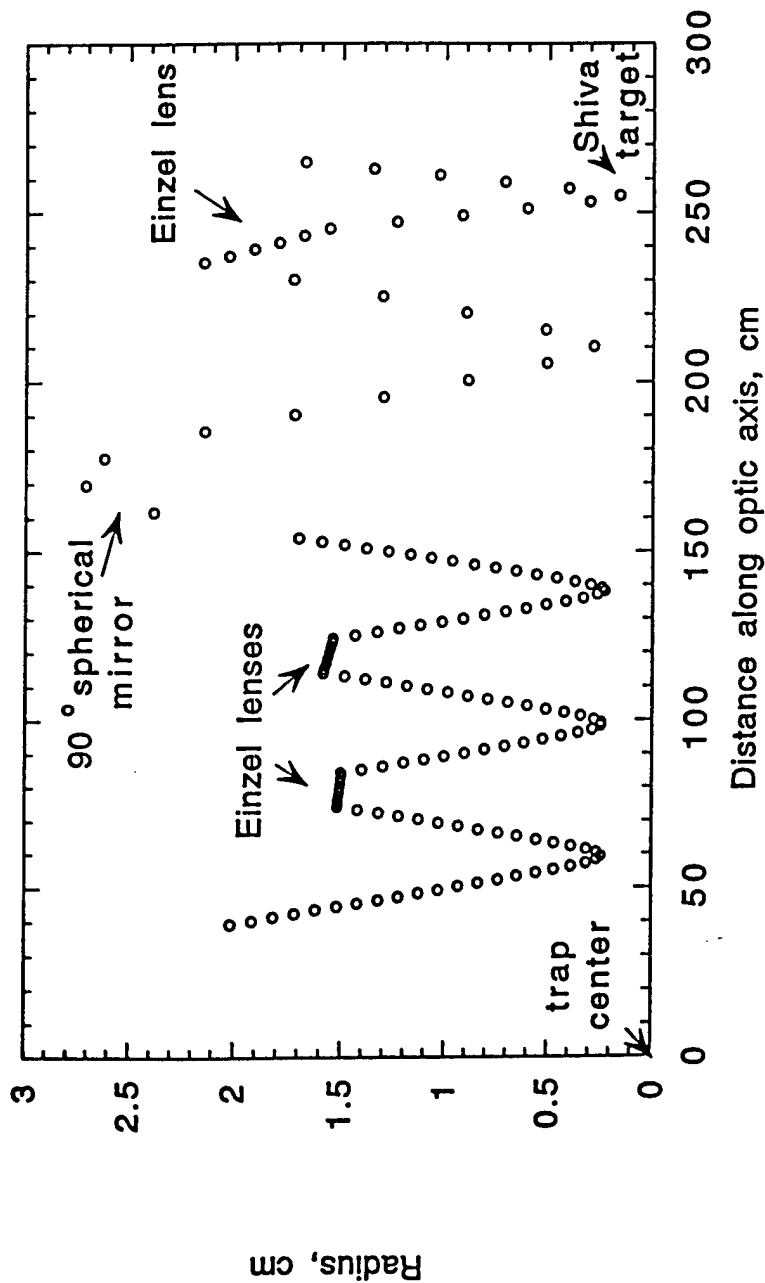


Figure 4

# Portable trap to Shiva target beam optics



Lenses (triplets)				Mirror
	L1	L2	L3	
Length (cm)	20	20	20	31
Radius (cm)	2	2	2	20
Voltages (V)	750	750	750	+1700

Figure 5

# Target compression by working fluids driven with solid liner implosions

P.-R. Chiang, R. A. Lewis, and G. A. Smith

*Laboratory for Elementary Particle Science, Department of Physics, The Pennsylvania State University, University Park, Pennsylvania 16802*

J. M. Dailey

*Department of Aerospace Engineering, The Pennsylvania State University, University Park, Pennsylvania 16802*

S. Chakrabarti

*Department of Mechanical Engineering, The Pennsylvania State University, University Park, Pennsylvania 16802*

K. I. Higman

*Department of Nuclear Engineering, The Pennsylvania State University, University Park, Pennsylvania 16802*

D. Bell, J. H. Degnan, T. W. Hussey, and B. W. Mullins

*High Energy Plasma Division, Phillips Laboratory, Kirtland AFB, New Mexico 87117*

(Received 4 October 1993; accepted for publication 25 March 1994)

Compression by a spherical solid liner of a gold target surrounded by a hydrogen plasma is simulated. Two-dimensional simulations that treat only a subset of the physics included in the one-dimensional code were performed in an attempt to assess multidimensional effects. A one-dimensional numerical code has been developed to study the effects of thermal radiation and conduction. Results of pressure, density, and energy deposited for different initial plasma conditions are presented and discussed. Results from both one- and two-dimensional codes show that the average target density at peak compression is  $39\text{--}43\text{ g/cm}^3$ , using the SHIVA Star facility at 90 kV discharge.

## I. INTRODUCTION

Electromagnetically imploded solid liners have been employed at some laboratories as a means of achieving high-energy densities and pressures.<sup>1-7</sup> Solid liner implosions are essentially hollow shell  $z$  pinches<sup>8</sup> or  $\theta$  pinches in which the mass of the liner is sufficient to prevent vaporization of the liner during the run-in phase of the implosion. At the Phillips Laboratory we are planning to use solid liner implosions to compress a hot hydrogen working fluid which will in turn compress an inner target. The advantages of a working fluid include decoupling of outer implosion nonuniformities from the central implosion and the possibility of transferring non-spherical liner energy onto a spherical target.

One application of this technology is antiproton-catalyzed microfission. Antiproton annihilations have been shown to be a strong source of neutrons<sup>9</sup> and pions<sup>10</sup> which, under conditions of high density, enable a significant reduction in burn time and, hence, size of fissile targets. The concept of antiproton-catalyzed microfission<sup>11,12</sup> will be tested by compressing a small fissile target with an electromagnetically imploded solid liner. A subcritical test is possible at this time, with presently limited numbers of antiprotons available. To simulate the compression of a solid target, a one-dimensional (1D) Lagrangian hydrodynamics with radiation code, HYDRAD,<sup>13</sup> has been developed. A two-dimensional (2D) magnetohydrodynamics (MHD) code, C-language arbitrary Lagrangian Eulerian (CALE),<sup>14</sup> is used in order to assess multidimensional effects. Since thermal radiation and conduction are not available in this version of CALE, 1D calcu-

lations with radiation and thermal conduction are performed to study their effects.

The solid liner implosion system is shown schematically in Fig. 1. The quasispherical liner is imploded by a 16 MA peak discharge from the Phillips Laboratory SHIVA Star capacitor bank, which stores 5.3 MJ of energy with 1300  $\mu\text{F}$  of capacitance at 90 KV. The current which flows through the liner forces it to collapse inward. A tapered spherical aluminum liner (1–2 mm thick) encloses 45° angle conical electrodes and a sealed chamber with a 4 cm radius; a gold target (gold is used instead of uranium due to availability of parametric information, e.g., equation of state, opacity, etc.) and a hydrogen plasma used as a working fluid are placed in the chamber. The implosion is designed to result in an isotropic, adiabatic compression intended to avoid generating shock waves in the target, which lead to undesirable high-temperature, low-density conditions; however, there is a trade-off between the requirement that the working fluid temperature, and hence its sound speed, be high enough so that the plasma will be compressed adiabatically, and the requirement that thermal losses to the walls be minimized. A hydrogen plasma with a temperature between 1 and 5 eV and density between  $10^{19}$  and  $10^{20}\text{ cm}^{-3}$  best satisfies these requirements.<sup>15,16</sup>

In Sec. II, HYDRAD is described. In Sec. III, results with different initial plasma parameters, specifically  $T_0=2\text{ eV}$ , 5 eV and  $n_0=1\times 10^{19}\text{ cm}^{-3}$ ,  $6\times 10^{19}\text{ cm}^{-3}$ , are presented. In Sec. IV, 1D results including radiation effects are presented and discussed.

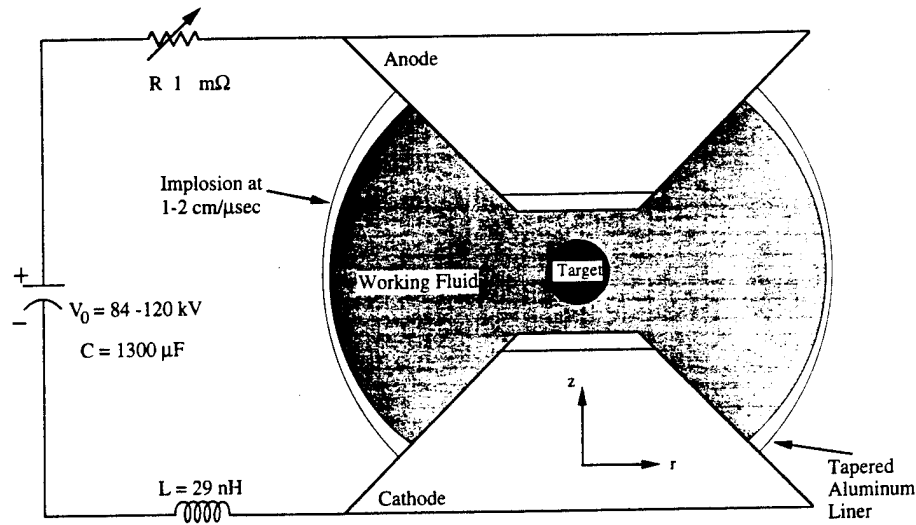


FIG. 1. Schematic of spherical solid liner at Shiva Star.

## II. DESCRIPTION OF HYDRAD AND CALE

### A. HYDRAD

#### 1. One-dimensional hydrodynamics

The model of HYDRAD assumes spherical symmetry and fluidlike solids. The one-dimensional Euler equations in spherical geometry are

$$\frac{\partial v}{\partial t} - \frac{\partial r^2 u}{\partial m} = 0 \quad (\text{continuity}), \quad (1)$$

$$\frac{\partial u}{\partial t} + r^2 \frac{\partial p}{\partial m} = g \quad (\text{momentum}), \quad (2)$$

and

$$\frac{\partial E}{\partial t} + \frac{\partial r^2 u p}{\partial m} = u g - K_{\text{th}} + q_{\text{ext}} \quad (\text{energy}). \quad (3)$$

Here,  $v = 1/\rho$  is the specific volume,  $u$  is the fluid velocity in the radial  $r$  direction,  $g$  is the external force,  $p$  is the pressure,  $E$  is the internal energy,  $m$  is the mass coordinate,  $K_{\text{th}}$  accounts for the rate of energy loss due to thermal radiation conduction, and  $q_{\text{ext}}$  is the rate of change of external energy sources.

We use a radiation thermal-conduction model<sup>17</sup> to calculate thermal radiation and conduction loss. Thermal conduction due to electrons and ions is included in the calculation by using the following equations, for both plasma and metallic solids:

$$K_{\text{th}} = -\frac{1}{\rho} \nabla \cdot (\kappa \nabla T), \quad (4)$$

$$\kappa = \kappa_i + \kappa_e + \kappa_r, \quad (5)$$

and

$$\kappa_r = \frac{16\sigma L_R T^3}{3}, \quad (6)$$

where  $T$  is the temperature,  $\sigma$  is the Stefan-Boltzmann constant,  $L_R$  is the Rosseland mean free length, and  $\kappa_i$  and  $\kappa_e$  are, respectively, the ion and electron thermal conductivities.

Since a strong shock wave may be created in the solid target due to its initial low temperature, it is necessary to use a sophisticated numerical scheme to account for large pressure and temperature gradients. Therefore, we adopt the piecewise parabolic method (PPM).<sup>18</sup> The PPM scheme is an extension of Godunov's approach,<sup>19</sup> which has: (1) a Riemann solver to handle wave interactions; (2) higher-order interpolation techniques; and (3) special monotonicity constraints and discontinuity detectors. The scheme is one of the most accurate numerical methods for hydrodynamics simulations.<sup>19</sup> The accuracy of the method is second order in time and third order in space. Instead of mixing a Lagrangian step and an Eulerian remap step, a pure Lagrangian scheme is used.

The Crank-Nicholson scheme<sup>20</sup> is used for solving the thermal conduction equation and the free-stream flux limiter<sup>20-22</sup> is imposed on thermal conduction coefficients,  $\kappa_r$  and  $\kappa_e$ , to compensate for the diffusion approximation. The numerical model for radiation calculations in HYDRAD is similar to the model of MEDUSA,<sup>22</sup> except that HYDRAD uses one temperature only.

#### 2. Equation of state and Rosseland mean free path

To simulate solids, including the target and liner, under compression a three-term model<sup>17</sup> is used to calculate the equation of state (EOS), namely,

$$E = E_c(v) + E_i^T(v, T) + E_e^T(v, T), \quad (7)$$

and

$$P = P_c(v) + P_i^T(v, T) + P_e^T(v, T), \quad (8)$$

where  $E_c(v)$  and  $P_c(v)$  are, respectively, the energy and pressure of the cold isotherms, and subscripts  $i$  and  $e$ , respectively, indicate the thermal contributions from ions and



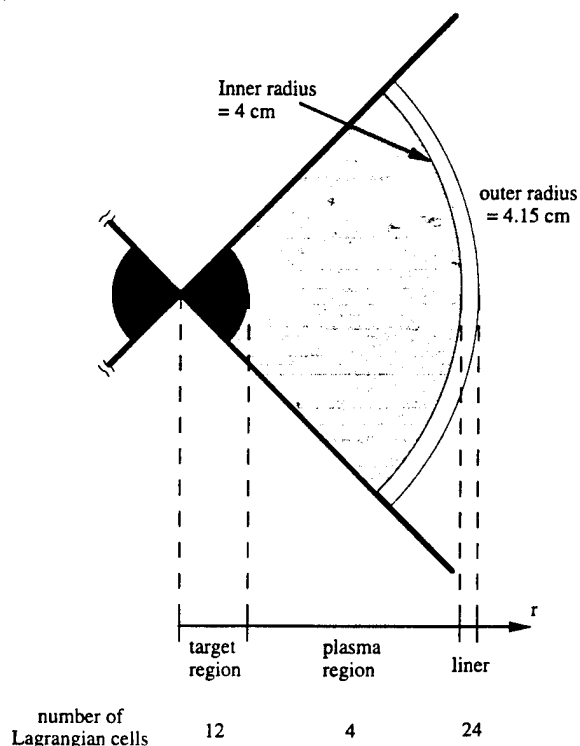


FIG. 2. Schematic of system geometry in one-dimensional simulation of compression.

electrons. Thermal contributions from ions and electrons are expressed in analytical forms.<sup>17</sup> The cold isotherms are generated from the SESAME EOS library,<sup>23</sup> and have been fit by a polynomial function to improve computation speed. The advantage of using this three-term model is that the temperature can be analytically computed without interpolation. The EOS model is reasonably accurate up to  $T=20$  eV.

With relatively low initial temperature compared to the temperature required for full ionization, the hydrogen gas is not fully ionized throughout the compression cycle. We therefore use the Saha equation<sup>24</sup> to calculate the EOS for the hydrogen plasma. Although the Saha equation may not be appropriate for hydrogen beyond solid density, the model is well justified since the Fermi energy is much smaller than the thermal energy.

We use power-law approximations based on the SESAME opacity library for calculating the Rosseland mean free path in the solids, i.e.,

$$L_R = A \rho^\alpha T^\beta, \quad (9)$$

TABLE I. Initial plasma conditions for simulations. All cases have a 27 g gold target at the center, and the liner and target are initially at room temperature.

Case	Density	Temperature (eV)	Pressure (bar)
A	$10^{19} \text{ cm}^{-3}$ ( $1.67 \times 10^{-5} \text{ g/cm}^3$ )	2	71
B	$10^{19} \text{ cm}^{-3}$ ( $1.67 \times 10^{-5} \text{ g/cm}^3$ )	5	161
C	$6 \times 10^{19} \text{ cm}^{-3}$ ( $1 \times 10^{-4} \text{ g/cm}^3$ )	2	256
D	$6 \times 10^{19} \text{ cm}^{-3}$ ( $1 \times 10^{-4} \text{ g/cm}^3$ )	5	952

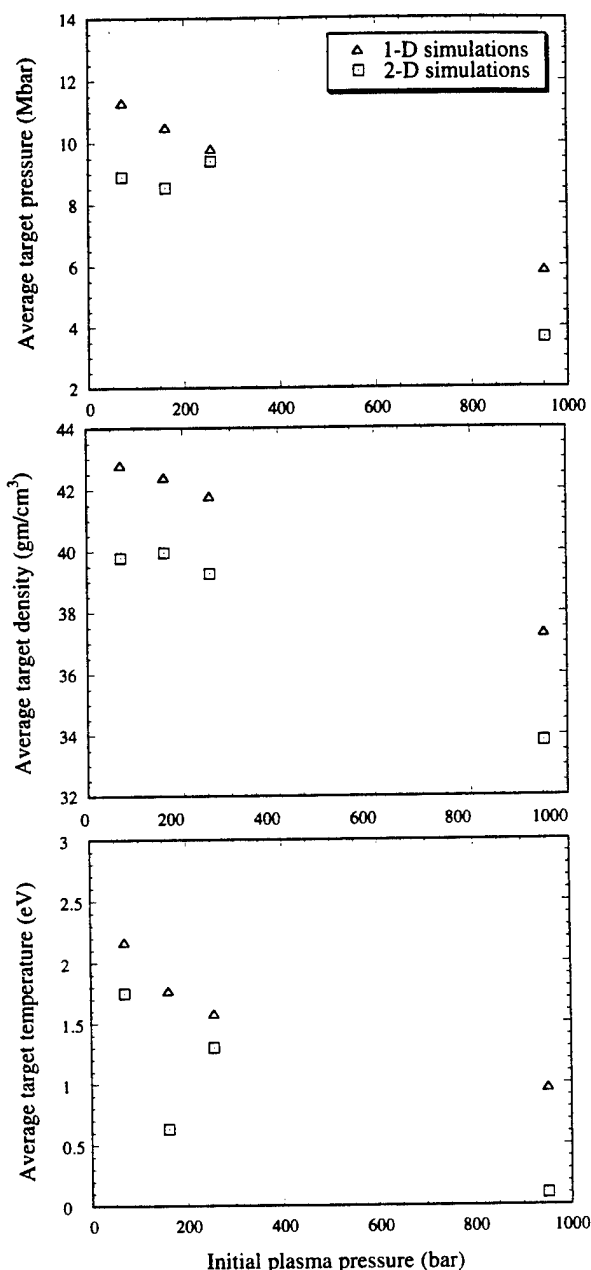


FIG. 3. Average target pressure, density, and temperature at peak compression vs initial plasma pressure from HYDRAD.

where  $A$ ,  $\alpha$ , and  $\beta$  are chosen to fit the SESAME opacity curves in the region of  $T \leq 10$  eV. Thermal conduction in the solid in this temperature regime is still dominated by electron thermal conduction, because the photon mean free path is much shorter than the electron mean free path. Since most temperatures in solids are below 10 eV, simulation results are not sensitive to this parameterization.

Photon absorption in hydrogen is dominated by shell absorption at temperatures below 10 eV. Since there is no analytical expression for opacity in this temperature regime, we use a Maxwellian distribution function to fit the Rosseland opacity curves for hydrogen in the SESAME opacity library

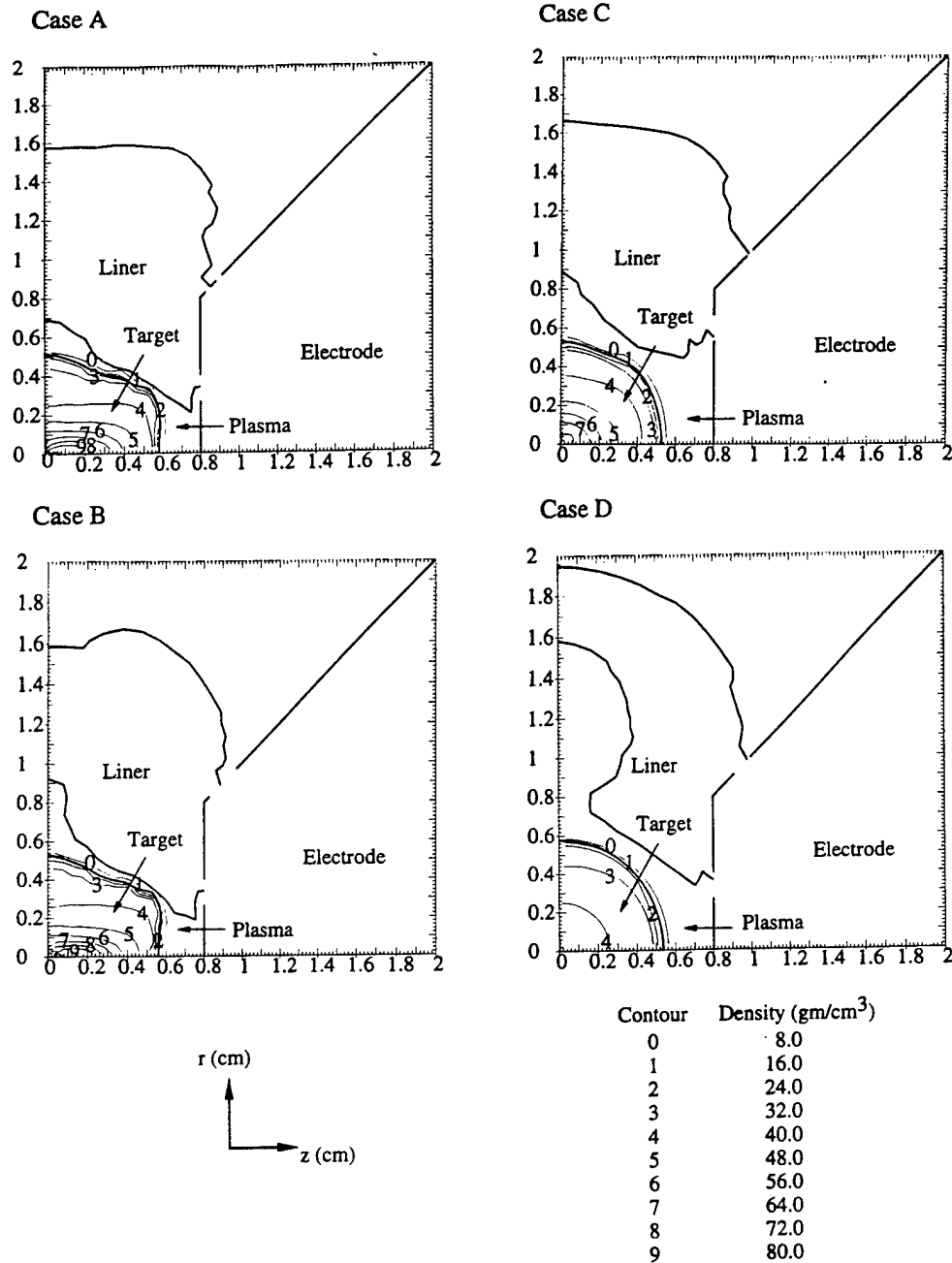


FIG. 4. System geometries and density contours in the target at peak compression for cases A–D (see Table I) from CALE.

for temperatures under 20 eV. Above 20 eV we use bremsstrahlung<sup>17</sup> absorption cross sections to calculate the opacity.

### 3. Pressure due to magnetic field

The system circuit for a solid liner compression can be schematically expressed as a simple  $RLC$  circuit shown in Fig. 1. The resistance  $R$  is considered to be constant throughout the compression cycle. If the liner inductance is constant in time, the current can be analytically expressed as

$$I(t) = CV_0 \frac{A^2 + B^2}{B} e^{-At} \sin Bt, \quad (10)$$

where  $V_0$  is the initial voltage of the capacitor bank,

$$A = \frac{R}{2L} \quad \text{and} \quad B = \left( \frac{1}{LC} - \frac{R^2}{4L^2} \right)^{1/2}. \quad (11)$$

However, since  $L$  is a function of the liner position, the circuit equation is coupled with the equation of motion. We have adjusted  $R, L, C$  from their initial values to compensate for the time-varying inductance in the system. The following parameters for a cylindrical implosion experiment<sup>6</sup> have been used in this calculation:  $R \approx 1 \text{ m}\Omega$ ,  $C = 1300 \text{ }\mu\text{F}$ ,  $L \approx 30 \text{ nH}$  (combined inductance of circuit and liner).

The diffusion time scale for the magnetic field in the liner is

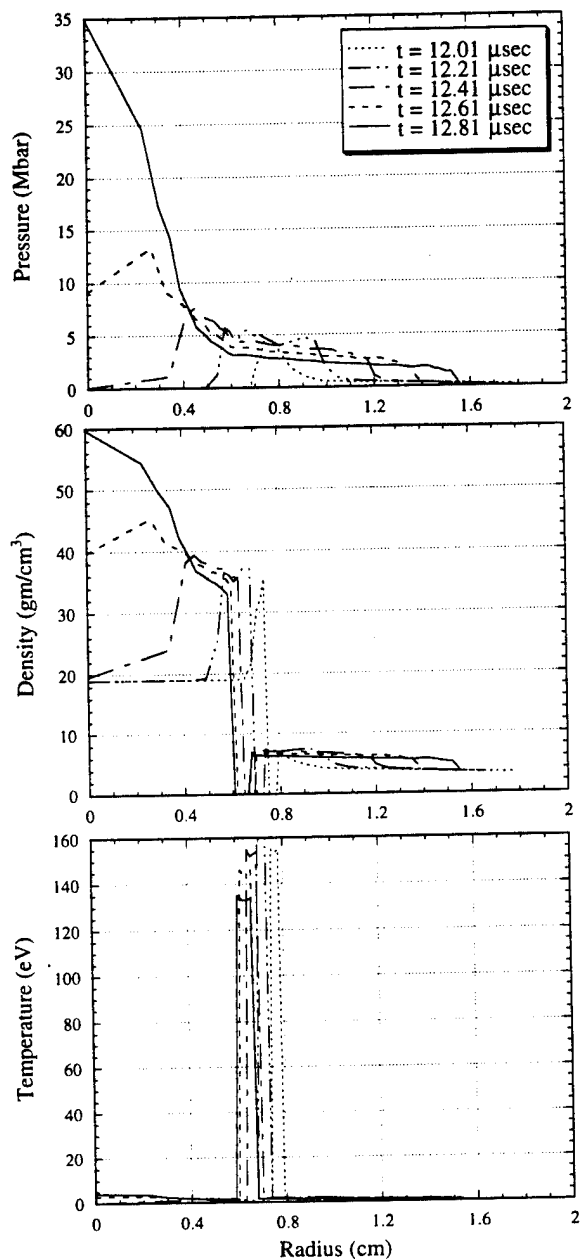


FIG. 5. Radial profiles of pressure, density, and temperature at different times close to the peak compression from HYDRAD for case A.

$$\tau_B = \sigma_L \mu_L \Delta r^2. \quad (12)$$

From CALE, the average liner temperature at peak compression is less than 1 eV. Using  $\sigma_L = 10^7 \Omega^{-1} \text{ m}^{-1}$  for the conductivity at  $T = 0.6 \text{ eV}$ ,  $\mu_L = 4\pi \times 10^{-7} \text{ H m}^{-1}$  for the magnetic permeability of the liner, and  $\Delta r = 1 \text{ mm}$  for the liner thickness, from Eq. (12) the diffusion time scale is  $50 \mu\text{s}$ , which is relatively long compared to the compression time ( $13 \mu\text{s}$ ). This estimate agrees with the CALE result which shows that  $10 \mu\text{s}$  is required for the current to diffuse across 1/4 of the liner thickness. Therefore, it is reasonable to approximate the spatial current distribution in the liner with a surface current.

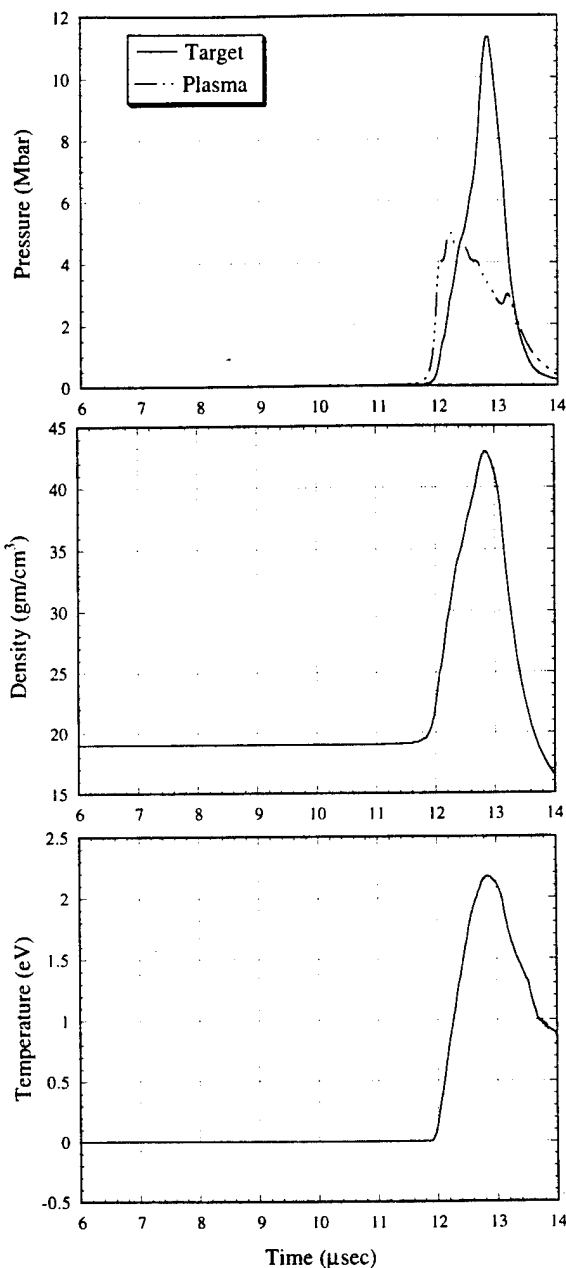


FIG. 6. Time history of average pressure, density, and temperature in the target from HYDRAD without radiation for case A.

The magnetic pressure due to a surface current through the liner is nonuniform along the polar angle direction for the spherical compression, and can be expressed as

$$P_B = \frac{B_\phi^2}{2\mu_0}, \quad (13)$$

where

$$B_\phi = \frac{\mu_0 I}{2\pi r_l \sin \theta} \quad (14)$$

is the azimuthal component of the magnetic field,  $I$  is the time-varying current running through the liner,  $r_l$  is the radial position of the liner outer surface,  $\theta$  is the polar angle

TABLE II. Plasma conditions at peak compression from HYDRAD without radiation.

Case	Plasma pressure (Mbar)	Plasma temperature (eV)	Plasma density (gm/cm <sup>3</sup> )
A	3.32	138	0.0125
B	3.11	263	0.006 13
C	2.91	57	0.0266
D	2.17	110	0.0102

measured around the electrode symmetry axis  $z$ , and  $\mu_0$  is the magnetic permeability in vacuum. Since HYDRAD is a one-dimensional code, it can only compute a single value for the magnetic pressure. To account for the tapered liner thickness, HYDRAD uses an average thickness for the liner. The average magnetic pressure is

$$P_B = 1.247 \frac{B_{\phi 0}^2}{2\mu_0}, \quad (15)$$

where

$$B_{\phi} = \frac{\mu_0 I}{2\pi r_l}. \quad (16)$$

### B. CALE

The version of CALE used for the simulation has the following features: 2D MHD calculation in Eulerian coordinates or Lagrangian coordinates; elastic properties of materials; Saha equation for the equation of state and conductivity of hydrogen; polynomial function input for the EOS of solids; frictionless contact between liner and electrode; and no thermal radiation or conduction in the system.

A fully Eulerian calculation is chosen for the simulations in order to correctly treat details at complicated boundaries.

The conductivities of the aluminum and gold are parametrized by a four-phase model. The solid, liquid, and vapor conductivities are parametrized as a power-law dependence on temperature and density. The plasma conductivity is calculated using the Thomas–Fermi ionization state, rather than the Saha ionization, since the plasma states of interest are nearly degenerate.

Parameters for the EOS for the solids were taken from Ref. 14, while the EOS from the SESAME library was used to obtain parameters appropriate for the higher pressures encountered in the gold target. The strength properties of the metals is based on the Steinberg–Guinan model.

### C. Limit of energy deposition

The fraction of the 5.3 MJ of stored energy which is available for compression is of crucial importance for the microfission experiment. An upper limit to the amount of energy which can be converted to compression is obtained from the work-energy relation,

$$\Delta U = \int_{r_0}^{r_p} F_B dr = \int_{r_0}^{r_p} \left( -2 \ln \tan \frac{\theta_m}{2} \right) \frac{\mu_0 I^2(t)}{4\pi} dr, \quad (17)$$

TABLE III. Plasma conditions at peak compression from CALE.

Case	Plasma pressure (Mbar)	Plasma temperature (eV)	Plasma density (gm/cm <sup>3</sup> )
A	3.7	220	0.009
B	2.7	350	0.0040
C	2.4	76	0.0332
D	1.4	128	0.0057

where  $r_0$  is the initial position of the outer liner surface,  $r_p$  is the radius of the liner outer surface at peak compression, and  $\theta_m = \pi/4$  is the electrode angle. Since most of the displacement  $\Delta r$  occurs at the time when  $I(t)$  is close to the maximum, Eq. (17) can be written as

$$\Delta U_{\max}(\text{MJ}) \approx 1.8 \times 10^{-3} (r_0 - r_p) I_{\max}^2(\text{MA}), \quad (18)$$

where  $I_{\max}$  is the maximum value of  $I(t)$ . Equation (18) shows the fundamental limitation on the efficiency for energy conversion. For example, using  $r_0 = 4.15$  cm,  $r_p \approx 1.5$  cm, and  $I_{\max} = 16$  MA (90 kV discharge), the maximum energy available for compression is 1.2 MJ. From Eq. (18), the efficiency for energy conversion is 22% (1.2/5.3), which agrees with the prediction from CALE (19%).

## III. RESULTS OF SIMULATIONS

The geometry used in HYDRAD simulations is schematically shown in Fig. 2. The total number of Lagrangian cells is 40. The region containing the liner, working fluid, and target is divided into a continuous 15 (in  $z$ )  $\times$  100 (in  $r$ ) Eulerian grid in CALE. A fine grid (15 polar sectors, 13 radii) is used to describe the target to facilitate the subsequent simulation of nuclear reactions. Except for the center of the target, all cells are quadrilaterals. A typical run requires  $\approx 0.5$  h for HYDRAD without radiation, and  $\approx 15$  h for CALE in central processor unit (CPU) time on a DECstation 3100.

Initial conditions for four cases simulated are listed in Table I. In this section, we show results of both 1D (HYDRAD) and 2D (CALE) simulations.

### A. Without radiation

Since the liner is tapered (see Fig. 1), we take the average thickness of 1.5 mm as the initial thickness of the liner. This leads to a 1D liner mass of 59 g, as compared to the actual mass of 51 g used by CALE. Figure 1 shows that the liner and the plasma occupy an angle of  $\pi/2$  rad in the  $\theta$

TABLE IV. Energy distribution in the system at peak compression from HYDRAD without radiation.

	Case A	Case B	Case C	Case D
Internal energy in target	290 kJ	248 kJ	222 kJ	121 kJ
Internal energy in plasma	124 kJ	238 kJ	306 kJ	597 kJ
Internal energy in liner	780 kJ	709 kJ	657 kJ	399 kJ
Kinetic energy in target	3 kJ	3 kJ	2 kJ	1 kJ
Kinetic energy in plasma	$\approx 0.04$ J	0.2 J	24 J	9 J
Kinetic energy in liner	51 kJ	56 kJ	66 kJ	100 kJ
Total energy	1.25 MJ	1.25 MJ	1.25 MJ	1.22 MJ

TABLE V. Energy distribution in the system at peak compression from CALE.

	Case A	Case B	Case C	Case D
Internal energy in target <sup>a</sup>	221 kJ	192 kJ	206 kJ	89 kJ
Internal energy in plasma	114 kJ	243 kJ	149 kJ	368 kJ
Internal energy in liner <sup>a</sup>	616 kJ	486 kJ	591 kJ	358 kJ
Kinetic energy in target	13 kJ	2 kJ	11 kJ	1 kJ
Kinetic energy in plasma	2 J	3 J	11 J	300 J
Kinetic energy in liner	38 kJ	35 kJ	50 kJ	79 kJ
Total energy	1002 kJ	958 kJ	1017 kJ	895 kJ

<sup>a</sup>The energy of degenerate electrons has been estimated by using the cold-temperature EOS from the TFC model and included in the internal energy.

direction, whereas the target subtends an angle of  $\pi$  rad. The target, which subtends an angle from  $\pi/4$  to  $3\pi/4$  in Fig. 2, contains 71% of the full target volume. Therefore, the target radius is increased by a factor of 1.12 to simulate a target of the same mass. The target in all HYDRAD simulations has a mass of 27 g and a radius of 0.783 cm.

Figure 3 shows target pressure, density, and temperature, spatially averaged at peak compression, as a function of the initial plasma pressure from HYDRAD and CALE simulations. The average target densities from HYDRAD simulations range from 38 to 43 g/cm<sup>3</sup>, while from CALE simulations the densities range from 34 to 40 g/cm<sup>3</sup>, as the initial pressure ranges from 71 bar (case A) to 952 bar (case D). At initial plasma pressures below 256 bar (case C), the average target density at peak compression is almost constant ( $\approx 42$  g/cm<sup>3</sup>) from 1D, and  $\approx 39$  g/cm<sup>3</sup> from 2D. With the initial pressure at 952 bar (case D), the target density is 8% less than in cases A–C. These results clearly show an inverse correlation between density and initial plasma pressure; however, there is a trade-off for increasing the liner momentum, i.e., a greater liner momentum may create a stronger shock wave in the target, which may increase thermal energy at the expense of compression energy, leading to lower target density.

Average target densities from CALE at peak compression are consistently lower than from HYDRAD by 3–4 g/cm<sup>3</sup>.

TABLE VI. Comparison between HYDRAD and CALE for case A.

Parameters	HYDRAD	CALE
Initial plasma conditions	2 eV, $1 \times 10^{19}$ cm <sup>-3</sup>	2 eV, $1 \times 10^{19}$ cm <sup>-3</sup>
Target	27 g Au	27 g Au
Initial target radius	0.783 cm	0.682 cm
Maximum current	$\approx 16$ MA	$\approx 16$ MA
Peak compression time	12.81 $\mu$ s	12.99 $\mu$ s
Plasma $P$ at peak	$\approx 3.3$ Mbar	$\approx 3.6$ Mbar
Plasma $T$ at peak	$\approx 135$ eV	$\approx 221$ eV
Maximum target $P$ at peak	$\approx 34$ Mbar	$\approx 147$ Mbar
Maximum target $\rho$ at peak	$\approx 60$ g/cm <sup>3</sup>	$\approx 94$ g/cm <sup>3</sup>
Maximum target $T$ at peak	$\approx 4.8$ eV	$\approx 11.8$ eV
Average target $P$ at peak	$\approx 11.3$ Mbar	$\approx 10$ Mbar
Average target $\rho$ at peak	$\approx 43$ g/cm <sup>3</sup>	$\approx 40$ g/cm <sup>3</sup>
Average target $T$ at peak	$\approx 2.2$ eV	$\approx 1.7$ eV
Average liner $\rho$ at peak	$\approx 6.0$ g/cm <sup>3</sup>	$\approx 4.2$ g/cm <sup>3</sup>
Average liner $T$ at peak	$\approx 0.3$ eV	$< 1$ eV

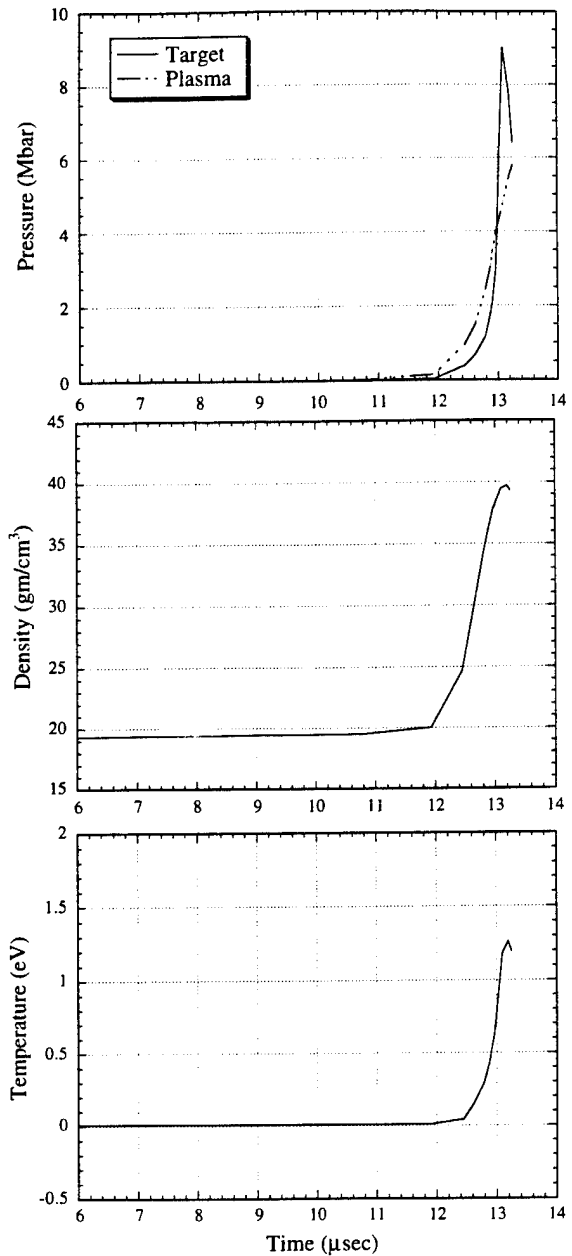


FIG. 7. Time history of average pressure, density, and temperature in the target from CALE without radiation for case A.

This density difference may be attributed to nonuniform compression in the 2D simulation. Because of the cylindrical symmetry of the liner, the radial compression wave converges earlier at the equator ( $z=0$ ) than the axial compression wave at the axis ( $r=0$ ). The compression of the target in CALE is more nearly cylindrical than spherical. This also explains why the target at peak compression appears prolate (as will be seen in Fig. 4). Therefore, the compression wave in CALE is less focused than in HYDRAD, giving rise to smaller average target densities.

Two-dimensional density profiles at peak compression from CALE are shown in Fig. 4. As seen, the lower the initial plasma pressure, the closer the liner gets to the target. This is especially true in cases B, C, and D. The bubbles seen in B,

C, and D in the plasma near the equator are most likely caused by the local imbalance of plasma and magnetic pressure, less likely by an instability. The magnetic pressure is not uniform along the  $\theta$  direction and is lowest at the equator ( $z=0$ ), as Eq. (14) shows. The plasma pressure, which is nearly uniform, exceeds the magnetic pressure earlier in time at the equator than for regions closer to the pole. A bubble is developed as the net force near the equator pushes outward. In case D, a large bubble has been formed in the liner due to early development of high pressure in the plasma. As seen by the contour lines, higher initial plasma pressure results in more nearly adiabatic and uniform target compression. The density gradients for case D are much smaller than those for cases A, B, and C and the contours are more spherical than cylindrical. Referring back to Fig. 3, the target temperature for case D is low, indicating that target compression is more nearly adiabatic.

The CALE simulation indicates that some interesting physics is occurring as the liner flows past the  $45^\circ$  electrode corner. The following information is provided by CALE: time,  $9.5 \mu\text{s}$ ; speed of liner near electrode,  $0.8 \text{ cm}/\mu\text{s}$ , speed of sound in liner,  $0.7 \text{ cm}/\mu\text{s}$ , temperature of liner,  $1.1 \text{ eV}$  for  $r < 0.8 \text{ cm}$ ,  $0.17 \text{ eV}$  for  $r > 0.8 \text{ cm}$ ; and pressure in the liner,  $320 \text{ kbar}$  for  $r < 0.8 \text{ cm}$  and  $220 \text{ kbar}$  for  $r > 0.8 \text{ cm}$ .

The liner gets very hot as it moves past the electrode corner. The speed indicated above suggests that a separation between the liner and electrode might occur; however, no indication of this separation is observed in CALE, possibly because the region of possible separation is small compared to the grid size of  $0.6 \text{ cm}$  (radial) by  $0.3 \text{ cm}$  (axial) in this area. Radiographs from the recent experiment at SHIVA Star confirm that the liner is in contact with the electrode at this point.

One-dimensional shock wave motion in the target can be seen in Fig. 5, which shows radial profiles of pressure, density, and temperature at different times close to peak compression for case A. Initially, the magnitude of the shock pressure in the target is approximately  $5 \text{ Mbar}$ , about the same as the plasma pressure. The momentum of the target surface compresses the target interior, until the pressure gets up to  $35 \text{ Mbar}$  at the center and rebounds. Time histories of the average target pressure, density, and temperature from HYDRAD for case A are shown in Fig. 6. The compression process takes about  $1 \mu\text{s}$ , and the dwell time for which the average target density is above  $35 \text{ gm}/\text{cm}^3$  is about  $700 \text{ ns}$ .

The plasma pressure at peak compression from HYDRAD ranges from  $2.17$  to  $3.32 \text{ Mbar}$  as shown in Table II. The temperature reaches above  $100 \text{ eV}$  for cases A and B; bremsstrahlung radiation from these hot dense plasmas may have significant influence on compression. For instance, the preheating of the target surface may reduce shock wave compression in the target. On the other hand, loss of plasma pressure at early times may increase maximum liner momentum, thus causing a high plasma pressure at peak compression. These two competing mechanisms can affect compression in either way.

Table III shows plasma conditions at peak compression from CALE. Plasma pressures are  $2$ – $4 \text{ Mbar}$ , which are close to HYDRAD values; However, the CALE temperatures are

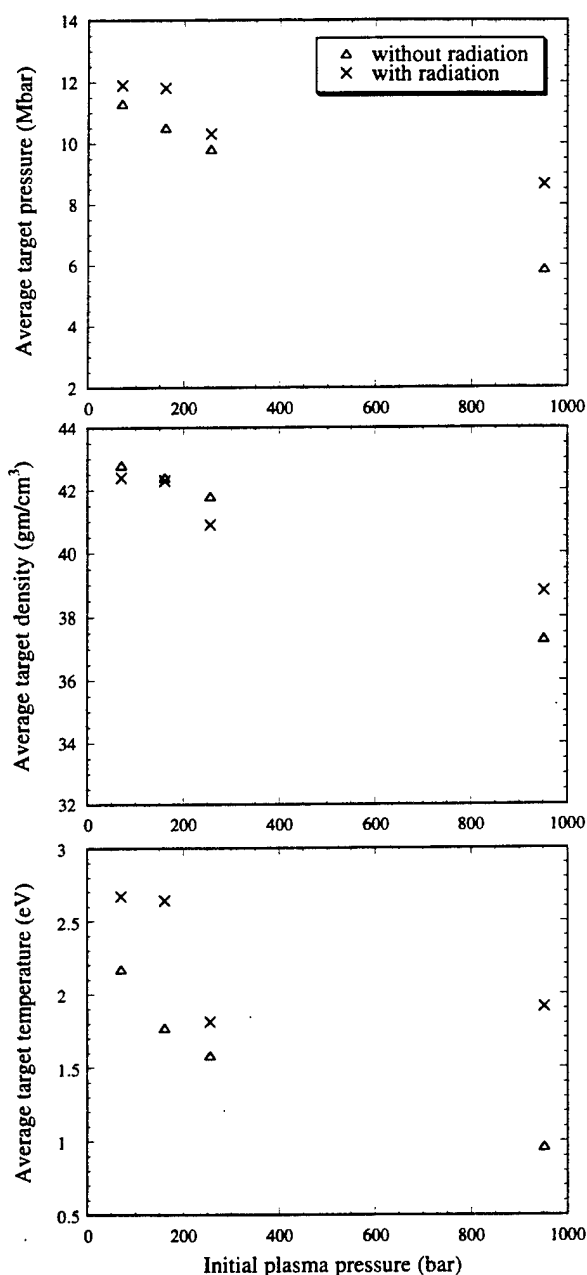


FIG. 8. Average target pressure, density, and temperature at peak compression vs initial plasma pressure from HYDRAD with and without radiation.

about  $1.2$ – $1.5$  times higher than those of HYDRAD. Since thermal conduction is not included in either calculation, this behavior suggests that viscous heating in the CALE plasma is quite significant.

The distribution of energy at peak compression from HYDRAD for all cases is shown in Table IV. The internal energy in solids is defined as the sum of (1) degenerate electron energy (compression energy), (2) ionization energy, and (3) ion thermal energy. The total energy deposited in the system is  $\approx 1.2 \text{ MJ}$  and is consistent with Eq. (18). The target energy is  $\approx 20\%$  of the total energy deposition. Most of the energy is deposited in the liner, and about  $30\%$ – $50\%$  of the total energy is in solids in the form of thermal energy. Energy of  $\approx 100$ – $200 \text{ kJ}$  is deposited in the target as degenerate

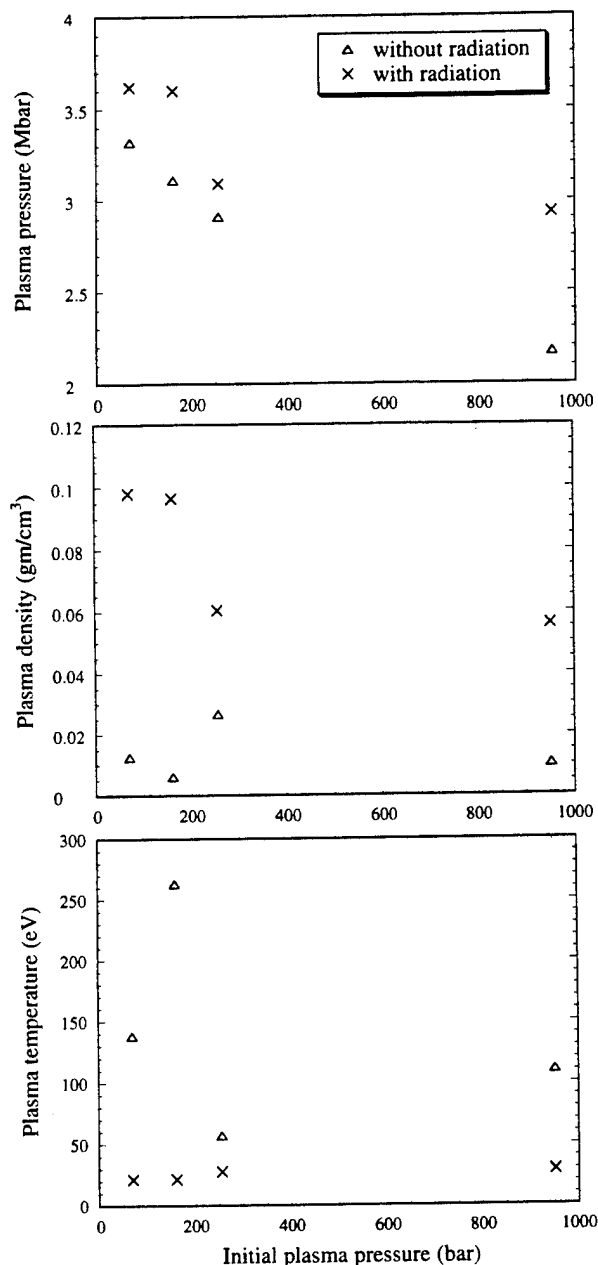


FIG. 9. Average plasma pressure, density, and temperature at peak compression vs initial plasma pressure from HYDRAD with and without radiation.

electron energy which is the energy accounted for by compression; therefore, about 4% of the capacitor energy is delivered into the target in the form of compression work.

For comparison, the energy distribution in each component from CALE for case A is shown in Table V. The total energy input is around 1 MJ, and  $\approx 20\%$  of the total energy input is deposited in the target. Again, this result agrees with HYDRAD.

Table VI lists HYDRAD and CALE results for case A (2 eV,  $1 \times 10^{19} \text{ cm}^{-3}$  initial plasma conditions.) The time at peak compression is about 13  $\mu\text{s}$  for both cases. CALE has a higher local pressure and density, although the average target pressure and density are higher in HYDRAD. The highest pressure in the CALE simulation usually occurs on the  $z$  axis, i.e., the

center of the compression. The CALE higher local quantities in Table VI may be due to the smaller radial grid size at the axis, which reveals more detailed structure of local quantities. Therefore, the CALE local pressure appears higher than that of HYDRAD. Time histories of average pressure, density, and temperature from CALE for case A are shown in Fig. 7. The dwell time for the average target density above 35  $\text{gm/cm}^3$  is about 500 nsec and comparable with HYDRAD.

## B. With radiation

Spatially averaged target quantities with radiation at peak compression from HYDRAD are shown in Fig. 8. For comparison, results without radiation from HYDRAD are also shown. The average target density increases as the initial plasma pressure decreases, which is similar to the trend seen without radiation. Therefore, a lower initial plasma pressure is more desirable.

The temperature in the target is generally higher with radiation than without radiation, as is the pressure. Target densities are lower in cases A–C and higher in D with radiation than without radiation. This shows that the role of radiation is complex. As discussed earlier, there are two competing mechanisms: (1) preheating of the target surface; and (2) loss of pressure in the hydrogen plasma, affecting target compression. These two mechanisms may lead to changes in target density, in either positive or negative directions. The effect of preheating depends more upon thermal conduction inside the target, while pressure loss depends more upon heat transfer at the boundary surface of the plasma. As the radiation loss in the plasma increases and thermal conduction inside the target remains unchanged, effects from pressure loss in the plasma will dominate over effects from preheating. Since the pressure loss leads to increased momentum in the liner, the target density is increased at peak compression. This explains why the average target density in case D increases, while the others decrease due to thermal radiation.

Plasma quantities at peak target compression are shown in Fig. 9. As seen, plasma temperatures in all cases are significantly lower with than without radiation. Correspondingly, plasma densities are higher with radiation than without radiation as a result of resisting the inward motion of the liner. Plasma densities in some cases are higher than solid density; however, since the Fermi energy at densities of  $\approx 0.1 \text{ g/cm}^3$  is around 5 eV, which is smaller than the plasma temperature ( $\approx 20 \text{ eV}$ ), use of the Saha equation is well justified.

Figure 10 shows the time history of average target pressure, density and temperature for case A. The histories are similar to results without radiation, despite significant differences in plasma properties when radiation is included. The dwell time for average target density above 35  $\text{g/cm}^3$  is around 700 ns. Because of radiation loss, the liner speed is faster with than without radiation. Peak compression times in all four cases are earlier by tens of nanoseconds due to radiation. Note that the target temperature is increased by about 0.5–1 eV due to the radiation.

The energy distribution with radiation from HYDRAD is shown in Table VII. Comparing Table VII with Table IV, all internal energies in the target are increased to  $\approx 320 \text{ kJ}$ . The increased energy raises the target temperature, instead of in-

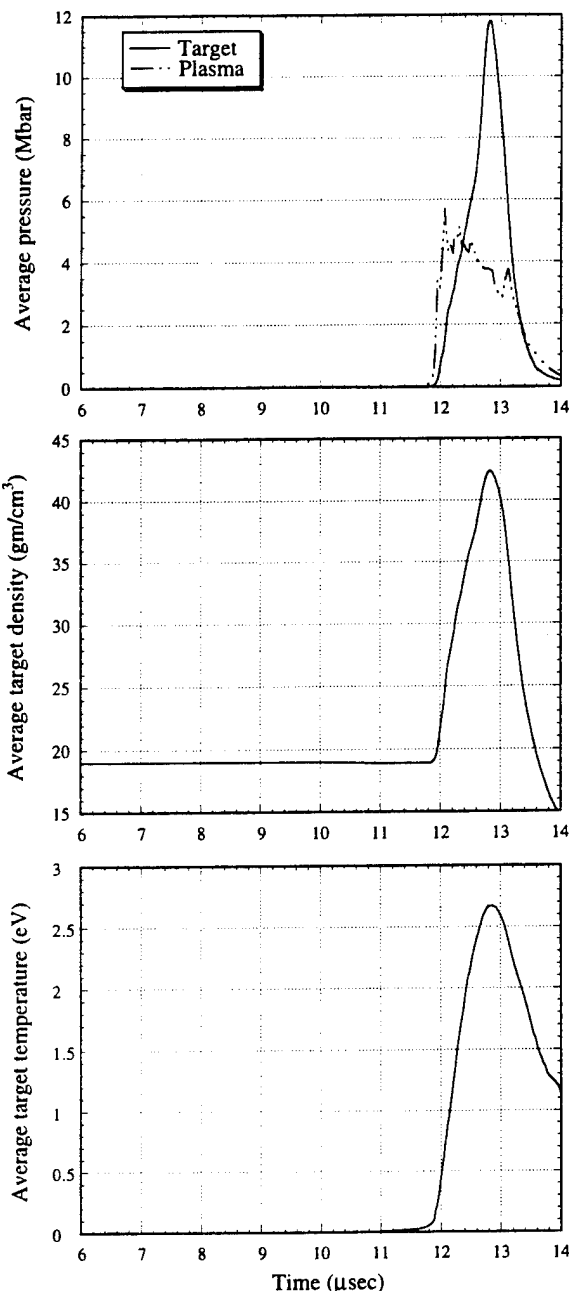


FIG. 10. Time history of average pressure, density, and temperature in the target from HYDRAD with radiation for case A.

creasing the target density, in cases A–C. The total energy deposited in the system is around 1.25 MJ, which is close to that without radiation.

#### IV. SUMMARY

In this study, the 1D hydrodynamics code HYDRAD and the 2D MHD code CALE are used to simulate compression of a hydrogen working fluid and target. It is found that the 1D and 2D results without radiation are comparable. The 1D calculation is much less time consuming than the 2D ( $\approx 1:30$  in CPU time), and includes important physics, i.e., thermal radiation, which is not available in our version of CALE. Although the 1D model simplifies several important physics

TABLE VII. Energy distribution in the system at peak compression from HYDRAD with radiation.

	Case A	Case B	Case C	Case D
Internal energy in target	344 kJ	342 kJ	322 kJ	320 kJ
Internal energy in plasma	18 kJ	18 kJ	144 kJ	147 kJ
Internal energy in liner	834 kJ	841 kJ	730 kJ	726 kJ
Kinetic energy in target	4 kJ	4 kJ	3 kJ	2 kJ
Kinetic energy in plasma	$\approx 0.005$ J	0.02 J	0.32 J	42 J
Kinetic energy in liner	49 kJ	46 kJ	54 kJ	63 kJ
Total energy	1.25 MJ	1.25 MJ	1.25 MJ	1.26 MJ

topics, for instance, circuit coupling and current diffusion, efforts have been made to minimize differences between the 1D and 2D results caused by these approximations. In the absence of a complete 2D code, HYDRAD is a very efficient and useful tool for simulating liner and target compressions.

The results are as follows: (a) The time for peak compression of a 27 g gold target is 12.5–13.5  $\mu$ s; (b) the dwell time for an average target density above 35 g/cm<sup>3</sup> ranges from 500 ns (2D) to 700 ns (1D); (c) an average target density (pressure) of about 40 g/cm<sup>3</sup> (12 Mbar) and a maximum local density (pressure) of 60–100 g/cm<sup>3</sup> (30–140 Mbar) can be achieved in the target using 5.3 MJ of energy from SHIVA star; (d) an energy of 1.2 MJ is deposited in the liner, plasma and target, including 200–350 kJ in the target; (e) radiation brings down the plasma temperature consistently to around 20 eV and increases the target temperature by about 0.5–1 eV; however, it has little influence on the average target density and pressure at peak compression; and (f) to obtain a higher target density, a lower initial plasma pressure is more desirable.

#### ACKNOWLEDGMENTS

This work was supported in part by the Air Force Office of Scientific Research, Jet Propulsion Laboratory (NASA), National Science Foundation, Penn State Propulsion Engineering Research Center Grant no. NAGW-1356, no. 8, and the Rocketdyne Corporation.

<sup>1</sup> A. E. Sherwood, E. L. Cantvel, C. A. Ekdhal, I. Henins, H. W. Hoiday, T. R. Jarboe, P. L. Klinger, R. C. Malone, J. Marshall, and G. A. Sawyer, in *Megagauss Physics and Technology*, edited by P. J. Turchi (Plenum, New York, 1980), p. 375.

<sup>2</sup> P. J. Turchi, A. L. Cooper, R. D. Ford, D. J. Jenkins, and R. L. Burton, in *Megagauss Physics and Technology*, edited by P. J. Turchi (Plenum, New York, 1985), p. 375.

<sup>3</sup> S. G. Alikhanov, V. P. Bakhtin, and D. A. Toporkov, in *Ultrahigh Magnetic Fields—Physics, Techniques, Applications*, edited by V. M. Totov and G. A. Shvetsov (Nauka, Moscow, 1984), p. 213.

<sup>4</sup> A. G. Eskov, M. I. Kitayev, and R. Kh. Kurtmullayev, in *Ultrahigh Magnetic Fields—Physics, Techniques, Applications*, edited by V. M. Totov and G. A. Shvetsov (Nauka, Moscow, 1984), p. 204.

<sup>5</sup> A. A. Petrukhnin, N. P. Bidlyo, S. F. Garanin, V. M. Danov, V. V. Zmushko, A. I. Kuzyaev, V. N. Mokhov, E. S. Pavlovskii, V. A. Prokopov, V. K. Chernyshev, V. A. Shvetsov, and V. B. Yakubov, in *Ultrahigh Magnetic Fields—Physics, Techniques, Applications*, edited by V. M. Totov and G. A. Shvetsov (Nauka, Moscow, 1984), p. 406.

<sup>6</sup> J. H. Degnan, M. L. Alme, W. L. Baker, J. S. Buff, C. B. Boyer, C. J. Clouse, S. K. Coffey, D. W. Conley, D. Dietz, J. D. Graham, S. L. Gonzalez, K. E. Hackett, D. J. Hall, J. L. Holmes, E. A. Lopez, W. F. McCullough, D. W. Price, R. E. Reinovsky, N. F. Roderick, P. J. Turchi, and J. M. Welby, in *Megagauss Technology and Pulsed Power Applications*,



- edited by C. M. Fowler, R. S. Caird, and E. J. Erickson (Plenum, New York, 1987), pp. 699–706.
- <sup>7</sup>J. H. Degnan, W. L. Baker, J. D. Beason, C. J. Clouse, D. Dietz, D. J. Hall, J. L. Holmes, D. W. Price, and C. R. Sovinec, in *Megagauss Technology and Pulsed Power Applications*, edited by V. M. Titov and C. A. Shvetsov (Plenum, New York, 1990), pp. 623–630.
- <sup>8</sup>N. A. Krall and A. W. Trivelpiece, *Principles of Plasma Physics* (McGraw-Hill, New York, 1973).
- <sup>9</sup>B. Chen, T. A. Armstrong, R. A. Lewis, R. Newton, G. A. Smith, J. P. Bocquet, F. Malek, H. Nifenecker, M. Maurel, E. Monnard, P. Perrin, C. Ristori, G. Ericsson, T. Johansson, G. Tibell, M. Rey-Campagnolle, S. Polikanov, T. Krogulski, and J. Mougey, *Phys. Rev. C* **45**, 2332 (1992).
- <sup>10</sup>E. D. Minor, T. A. Armstrong, R. Bishop, V. Harris, R. A. Lewis, and G. A. Smith, *Z. Phys. A* **336**, 461 (1990).
- <sup>11</sup>R. A. Lewis, G. A. Smith, R. J. Kanzleiter, K. I. Higman, and R. Newton, *Fusion Tech.* **20**, 1046 (1991).
- <sup>12</sup>R. A. Lewis, R. Newton, G. A. Smith, and R. J. Kanzleiter, *Nucl. Sci. Eng.* **109**, 411 (1991).
- <sup>13</sup>P.-R. Chiang, HYDRAD—One-Dimensional Radiative Hydrodynamics Code, Laboratory for Elementary Particle Science, The Pennsylvania State University, 1993 (unpublished).
- <sup>14</sup>CALE users manual, July 1, 1991, R. Tipton, LLNL, Mail Stop L-35, P.O. Box 808, Livermore, Los Angeles, CA 94550; *Megagauss Technology and Pulsed Power Applications*, edited by C. M. Fowler, R. S. Cavid, and D. J. Erickson (Plenum, New York, 1987), p. 299.
- <sup>15</sup>F. M. Lehr, A. Alaniz, J. D. Beason, L. C. Carswell, J. H. Degnan, J. F. Crawford, S. E. Englert, T. J. Englert, J. M. Gahl, J. H. Holmes, T. W. Hussey, G. F. Kiuttu, B. W. Mullins, R. E. Peterkin, Jr., N. F. Roderick, P. J. Turchi, and J. D. Graham (unpublished).
- <sup>16</sup>F. M. Lehr, J. H. Degnan, D. Dietz, S. E. Englert, T. J. Englert, T. W. Hussey, G. F. Kiuttu, J. M. Messerschmitt, B. W. Mullins, C. A. Outten, R. E. Peterkin, Jr., N. F. Roderick, P. J. Turchi, and J. D. Graham, in 9th IEEE Pulsed Power Conference, June 6–10, 1993.
- <sup>17</sup>Ya. B. Zel'dovich and Yu. P. Raizer, *Physics of Shock Waves and Temperature Hydrodynamic Phenomenon* (Academic, New York, 1966).
- <sup>18</sup>P. Collela and P. R. Woodard, *J. Comp. Phys.* **54**, 174 (1984).
- <sup>19</sup>P. R. Woodard and P. Collela, *J. Comp. Phys.* **54**, 115 (1984).
- <sup>20</sup>T. Tajima, *Computational Plasma Physics: With Applications to Fusion and Astrophysics* (Addison-Wesley, New York, 1989).
- <sup>21</sup>N. A. Tahir and K. A. Long, *Laser Part. Beams* **4**, 287 (1986).
- <sup>22</sup>J. P. Christiansen, D. E. T. F. Ashby, and K. V. Roberts, *Comp. Phys. Commun.* **7**, 271 (1974).
- <sup>23</sup>S. P. Lyon and J. D. Johnson, LA-UR-92-3407, 1992.
- <sup>24</sup>J. A. Bittencourt, *Fundamentals of Plasma Physics* (Pergamon, New York, 1988).



# Neutron Yields for Antiproton Microfission Experiments

Christopher E. Gazze and Richard J. Newton

*The Pennsylvania State University, Department of Nuclear Engineering  
University Park, Pennsylvania 16802*

and

Raymond A. Lewis, Pi-Ren Chiang, and Gerald A. Smith

*The Pennsylvania State University, Department of Physics  
Laboratory for Elementary Particle Science, University Park, Pennsylvania 16802*

*Received November 8, 1993*

*Accepted July 19, 1994*

**Abstract**—Neutrons that are produced following antiproton annihilation on uranium nuclei are transported through compressed targets by the SCATTER Monte Carlo code in support of antiproton microfission experiments. The SCATTER code and necessary input data are described. Results show that the high-energy ( $>20$  MeV) component of the source is responsible for the majority of the neutron yield. Results for a wide range of uniformly compressed targets are presented for moderation levels of hydrogen-to-uranium ratios of 0:1, 3:1, and 9:1 in  $^{235}\text{U}$  targets and  $^{238}\text{U}$ . Moderation is found to increase neutron yields at a given pr. Uniformly compressed unmoderated  $^{238}\text{U}$  targets demonstrate 9 to 16% lower yields than  $^{235}\text{U}$ . Four targets under different, nonuniform compression conditions are considered. The average yield in these cases is  $\sim 21.8 \pm 0.2$  neutrons per source antiproton, an increase of 34% over the 16.3 primary neutrons per antiproton. The average yield of the nonuniform compression cases agrees within error with uniformly compressed targets.

## I. INTRODUCTION

Practical, nondestructive uses of nuclear systems are limited by the inability to safely harness the resulting large energy yields. In microfission, these energy yields are reduced by burning as little fissile material as possible while still maintaining a net energy gain. The concept, first introduced by Askar'Yan et al.<sup>1</sup> and Winterberg,<sup>2</sup> involves starting a chain reaction in a small, compressed fissile target.

The use of antiprotons annihilating on the surface of fissionable nuclei has been proposed<sup>3</sup> as the initiator for the chain reaction. Recent experiments<sup>4</sup> at the Low-Energy Antiproton Ring at CERN, in Geneva, Switzerland, have demonstrated that large numbers of highly energetic neutrons are released following such annihilations. These neutrons could be used to bypass the slow, early stages of the chain reaction, increasing

the number of fissions that can occur during the confinement time.

A Monte Carlo study was performed to examine moderated and unmoderated neutron reactions induced by the annihilation of antiprotons in fissionable nuclei. This study was done in support of a larger effort to demonstrate the feasibility and potential applications of antiproton catalyzed microfission at the SHIVA Star facility.<sup>5</sup> Other studies address reactions induced by pions released during the annihilation of antiprotons<sup>6</sup> and the trapping and delivery of the antiproton beam.<sup>7</sup>

The goal of the SHIVA Star experiment is to demonstrate that significant subcritical neutron yields can be observed under moderate levels of compression following antiproton annihilation on fissionable targets. The SHIVA Star is a solid liner imploder capable of providing 10 to 40 Mbars of pressure to compress a small (tens of grams) uranium target. The apparatus is

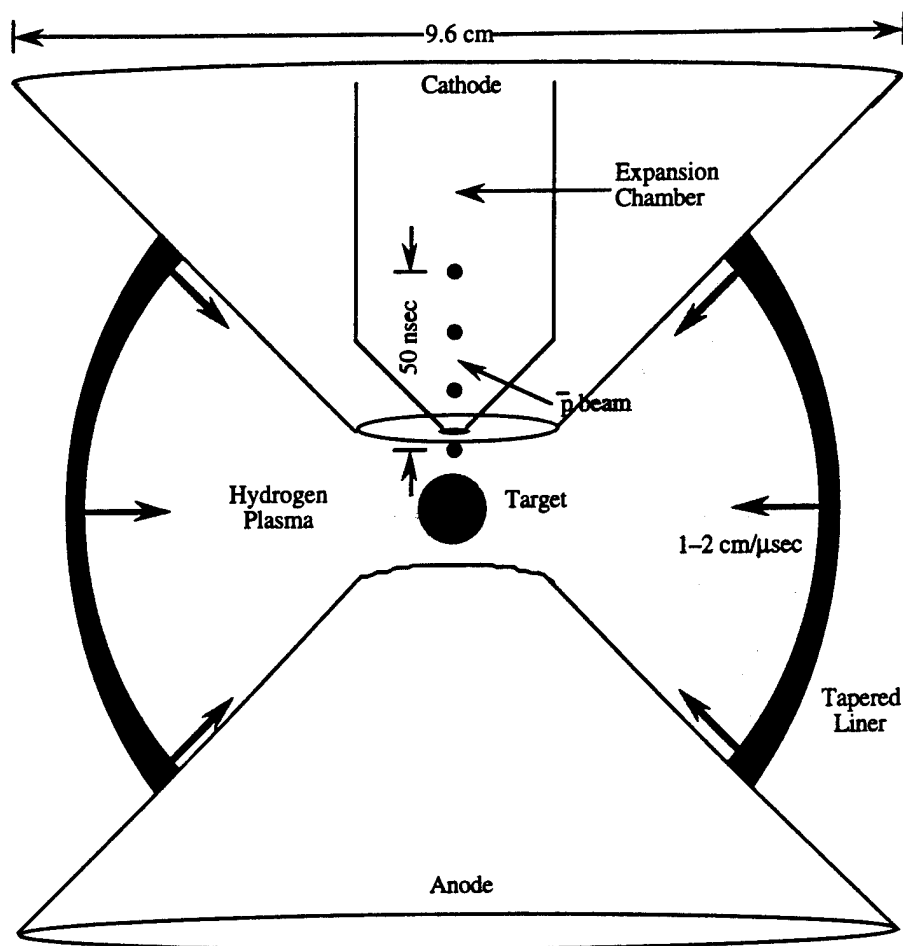


Fig. 1. Schematic diagram of the SHIVA Star apparatus.

shown schematically in Fig. 1. The system operates by discharging a 5.3-MJ capacitor bank through a thin liner connecting the anode and cathode. The resulting 10-MA average current induces large inwardly directed magnetic pressures. The liner then collapses, applying pressure on the working fluid inside, which is a hydrogen plasma. This produces a uniform pressure field in the plasma that can uniformly and adiabatically compress the spherical target that is located in the center of the system.

The HYDRAD one-dimensional radiative Lagrangian hydrodynamics code<sup>5</sup> and the CALE two-dimensional magnetohydrodynamics code<sup>8</sup> have been used to model the compression process in the SHIVA apparatus. The CALE finite difference code provides the time-dependent density profile during the compression. The information provided by the computer codes is then used directly in the neutronics calculation. The amount of energy released from nuclear interactions is  $\sim 1$  erg. This has a negligible effect on the hydrodynamics, which is driven by 5.6 MJ of stored energy in SHIVA Star. Therefore, the use of sequential and de-

coupled hydrodynamics-neutronics calculations for this application is fully justified.

## II. DESCRIPTION OF NEUTRONICS

To accurately model neutron reactions initiated by antiproton annihilation, one must characterize neutron cross sections within an energy regime that extends up to 750 MeV. Although existing data libraries focus on the energy regime below 20 MeV, our work has shown that neutrons in the higher energy regime are important.

The kinetic energy spectrum of neutrons from the antiproton annihilation is shown in Fig. 2 (Ref. 4). The spectrum extends to 747 MeV, which is the highest kinetic energy cited in the literature for fission-related reactions in uranium. The released neutrons are distributed isotropically in the laboratory frame and total 16.3 (Ref. 4).

The SCATTER Monte Carlo code was written to study the neutronics of the SHIVA Star experiment.<sup>9</sup>

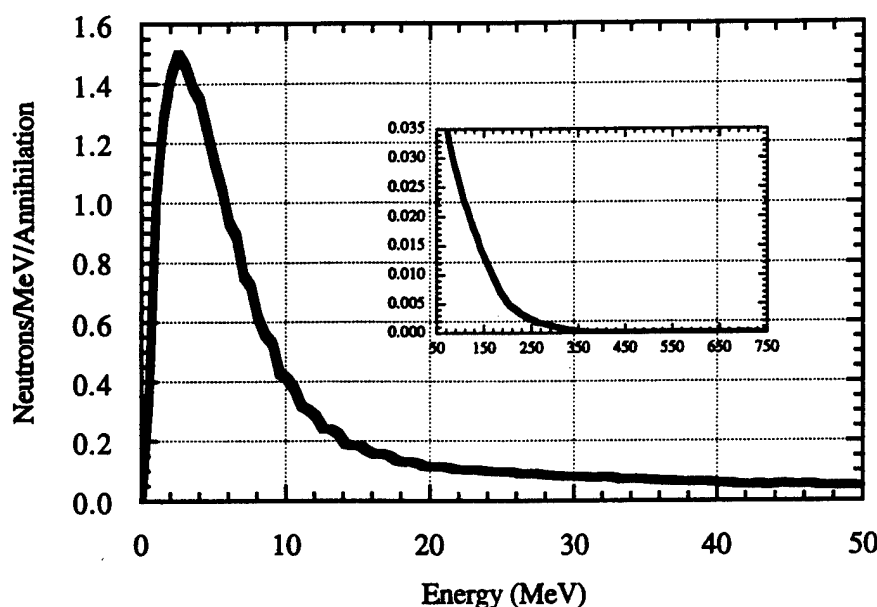


Fig. 2. Neutron energy spectrum resulting from antiproton annihilation in uranium.

The code requires a variety of input data. The energy spectrum of annihilation neutrons has been used to model the source. Total and partial neutron cross sections have been taken from the literature (from 0 to 1000 MeV). A time-dependent density profile has been taken from CALE and applied to the model. Anisotropic elastic-scattering probability distributions have been used to propagate neutrons through the target. Finally, energy-dependent multiplicity data and fission and other inelastic energy spectra have been applied to create secondary neutrons with the appropriate energies.<sup>4,10,11</sup>

Cross sections and nuclear reaction data in the lower energy regions (below 100 MeV for hydrogen and below 20 MeV for uranium) have been taken from the ENDF/B-VI database, compiled by Brookhaven National Laboratory.<sup>12</sup> Data for the higher energy regions were gathered from a variety of sources in the literature.<sup>9,13,14</sup> High-energy cross-section data that are used by the SCATTER program are shown in Fig. 3 for hydrogen and in Figs. 4 and 5 for <sup>235</sup>U and <sup>238</sup>U, respectively. The neutron production cross section ( $n \rightarrow xn$ ) is defined as the total cross section minus the elastic and inelastic ( $n \rightarrow n'$ ) cross sections. Multiplicity data are presented in Fig. 6 for uranium. The difference between <sup>235</sup>U and <sup>238</sup>U below 125 MeV results from the larger fission cross section in <sup>235</sup>U.

Spectra for neutrons released from high-energy reactions at 20 MeV (neutrons<sup>12</sup>), 155 MeV (protons<sup>11</sup>), 300 MeV (protons<sup>10</sup>), and 455 MeV (antiprotons<sup>15</sup>) are shown in Fig. 7. The 455-MeV curve is based on an energy transfer measurement for antiprotons at rest. In terms of equivalent laboratory bombarding energy, the curve would likely be represented at a higher energy.

The SCATTER code has been extensively tested. Predictions for more conventional neutron experiments (i.e., those occurring below 20 MeV) have been compared with the results of the Monte Carlo Neutron Photon (MCNP) code.<sup>16</sup> The results produced by the two codes agree very well. To assess statistical accuracy, we calculated and studied figures of merit (FOMs) as a function of the number of case histories run. We found that the FOMs became stable after ~15 000 case histories. Typically, 40 000 case histories were compiled for each of the data points presented in this paper, giving a statistical confidence per data point in excess of 99.5%.

### III. RESULTS FOR UNIFORMLY COMPRESSED TARGETS

While the most probable energy for primary neutrons is 2 MeV (Ref. 4), the average energy of neutrons selected from the energy spectrum is just over 50 MeV. Neutron-multiplying interactions involving very high energy neutrons are important because of their high multiplicities and the high-energy secondary neutrons they can produce. The SCATTER code was run with the primary neutron spectrum (Fig. 2) terminated at 20 MeV. Results from these tests have shown that the primary neutron population above 20 MeV is responsible for more than half of the yield in a typical SHIVA Star target.

#### III.A. Uranium-235

Before analyzing targets specific to the SHIVA Star experiment, the SCATTER code was used to examine

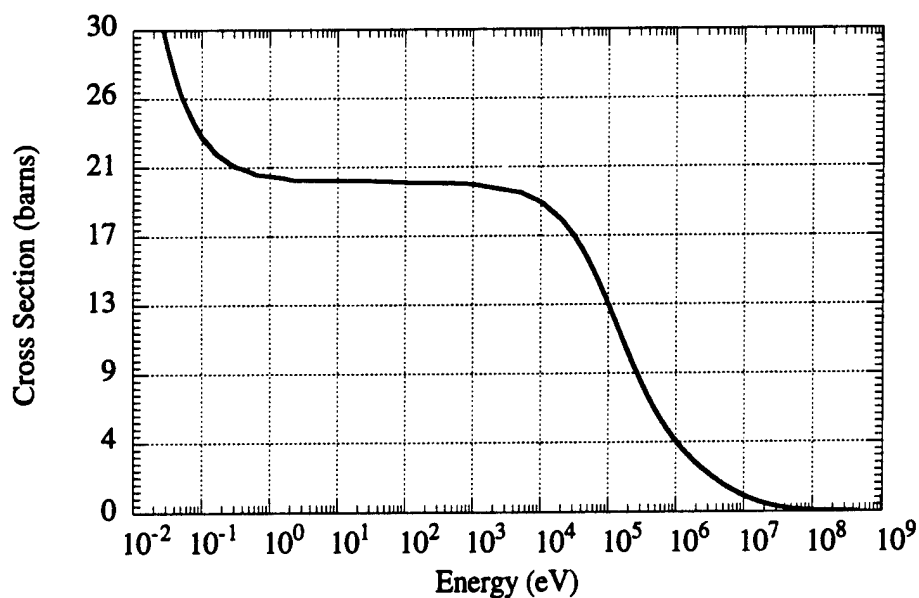


Fig. 3. Neutron elastic cross section in hydrogen.

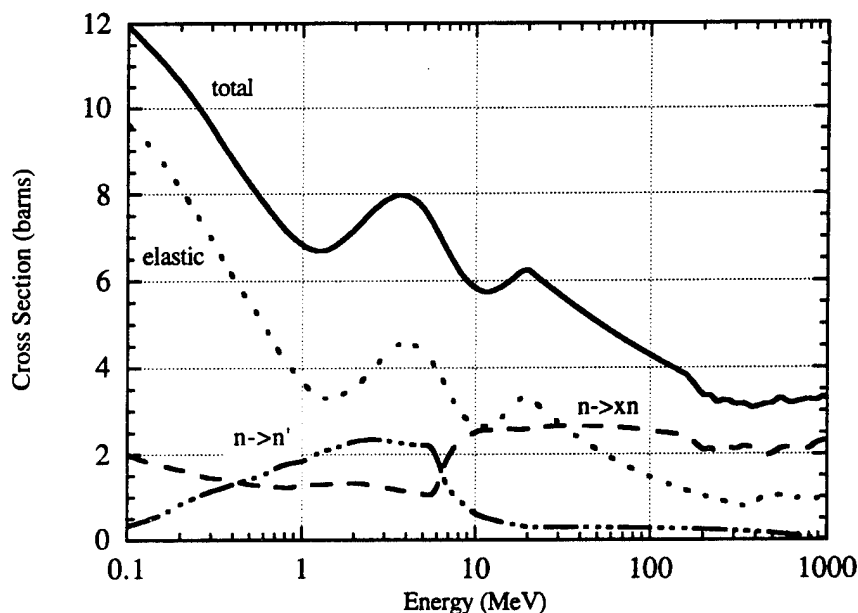


Fig. 4. Neutron cross sections for  $^{235}\text{U}$ : total cross section (solid line), neutron-producing cross section ( $n \rightarrow xn$ ) (dashed line), elastic cross section (dotted line), and inelastic cross section ( $n \rightarrow n'$ ) (dot-dashed line).

simple, one-region, spherical targets of uniform density. Such targets have been described by the product of their density and radius,  $\rho r$ . The purpose of this study is to examine the behavior of the neutron population over a wide range of compression conditions and levels of moderation. Cases have been run for  $\rho r$  from 10 to 40 g/cm<sup>2</sup> and at moderation levels (molar ratio)

of hydrogen-to-uranium ratios of 0:1 (unmoderated), 3:1, and 9:1. Each case has used a 27-g target, typical of SHIVA Star targets.

Neutron yields for uniformly compressed cases using  $^{235}\text{U}$  are presented in Fig. 8. The neutron yield is defined as the number of neutrons escaping the target per source antiproton. The neutron yield increases

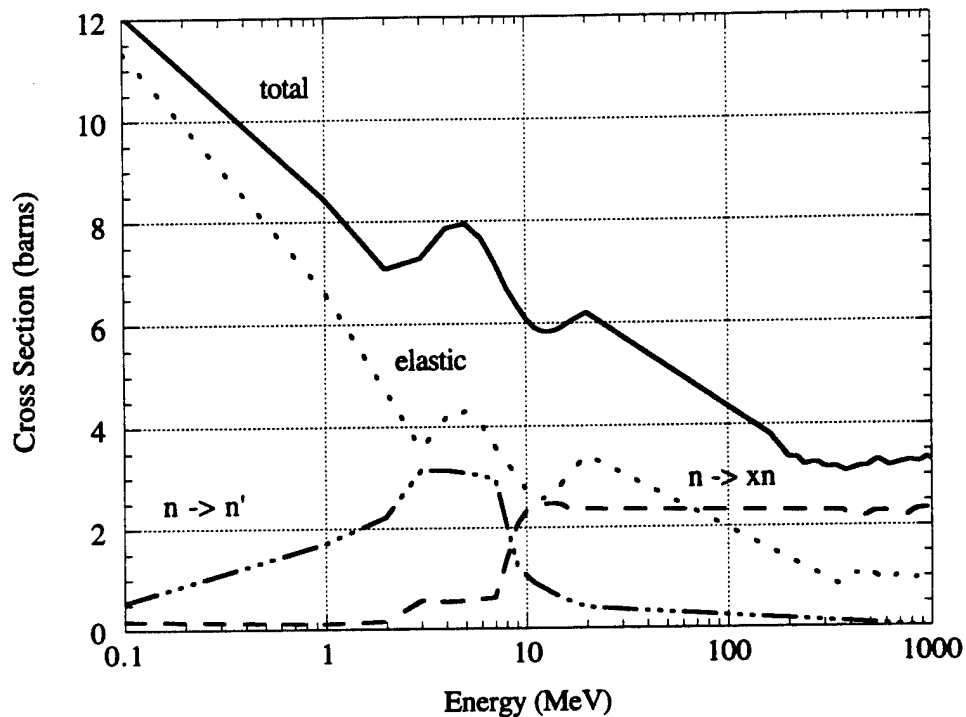


Fig. 5. Neutron cross sections for  $^{238}\text{U}$ : total cross section (solid line), neutron-producing cross section ( $n \rightarrow xn$ ) (dashed line), elastic cross section (dotted line), and inelastic cross section ( $n \rightarrow n'$ ) (dot-dashed line).

monotonically with  $\rho r$  at all levels of moderation. This dependence can be expressed by a power series in  $\rho r$  of the form

$$Y = c_0 + c_1(\rho r) + c_2(\rho r)^2 + c_3(\rho r)^3 + \dots, \quad (1)$$

where  $Y$  is the yield of escaping neutrons in neutrons per antiproton and  $c_i$ , shown in Table I for these fits, are the coefficients of the expansion. It is evident that the effect of adding moderation is to increase yield.

Figure 9 shows how average energies of the primary neutron population depend on  $\rho r$  and the moderation ratio in  $^{235}\text{U}$  targets. The statistical accuracy of these measurements is typically 10%. For all levels of moderation, the average energy at which primary neutrons

escape is approximately equal to the average energy at which they are created for all values of  $\rho r$ . For the 0:1 and 3:1 moderated cases, the average energy of absorbed neutrons is significantly higher than that of the rest of the population because of the larger neutron-production cross section ( $n \rightarrow xn$ ) above 8 MeV (see Fig. 4).

In the 3:1 moderated case, the behavior of the average absorption energy at low  $\rho r$  is the same as that observed for the unmoderated case. The effect of the hydrogen is not yet felt on the absorption average because the average path length of a neutron is relatively large at small values of  $\rho r$ . As  $\rho r$  increases, however, it becomes more likely that a neutron will be absorbed

TABLE I  
Coefficients for the Fitted Curves in Fig. 8

	Hydrogen-to-Uranium Ratio of 0:1	Hydrogen-to-Uranium Ratio of 3:1	Hydrogen-to-Uranium Ratio of 9:1
$c_0$ neutrons per antiproton	1.6300E+1 <sup>a</sup>	1.6300E+1	1.6300E+1
$c_1$ neutrons per antiproton (g/cm <sup>2</sup> )	2.1120E-1	1.7110E-1	2.1040E-1
$c_2$ neutrons per antiproton (g <sup>2</sup> /cm <sup>4</sup> )	6.0850E-4	3.0000E-3	2.0000E-3
$c_3$ neutrons per antiproton (g <sup>3</sup> /cm <sup>6</sup> )	0.0000E+0	0.0000E+0	0.0000E+0
$c_4$ neutrons per antiproton (g <sup>4</sup> /cm <sup>8</sup> )	0.0000E+0	0.0000E+0	4.6660E-6

<sup>a</sup>Read as  $1.6300 \times 10^{-1}$ .

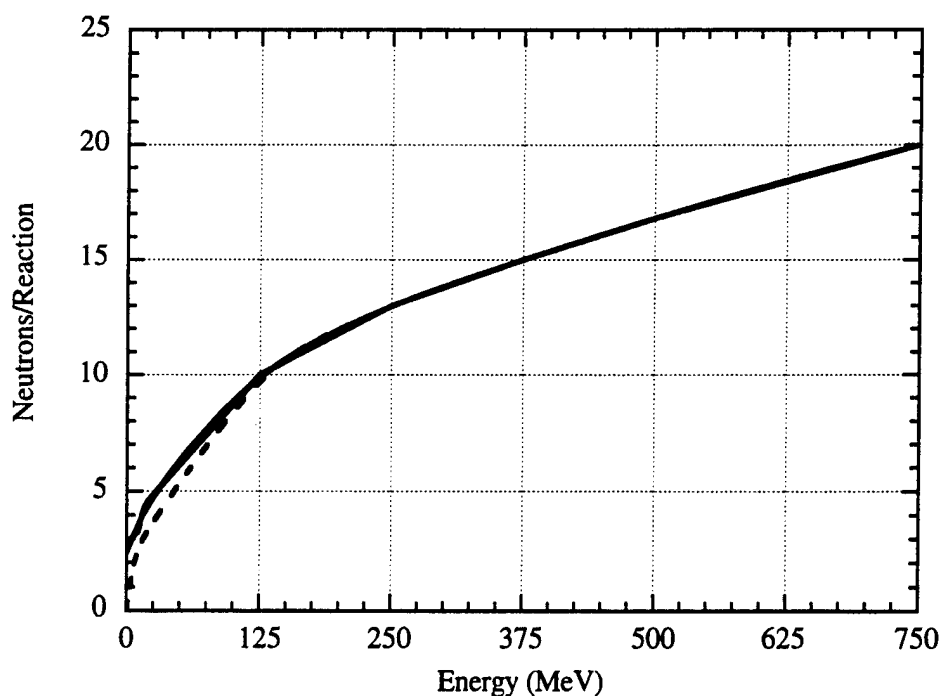


Fig. 6. Neutron multiplicity from neutron induced reactions in uranium:  $^{235}\text{U}$  (solid line) and  $^{238}\text{U}$  (dashed line).

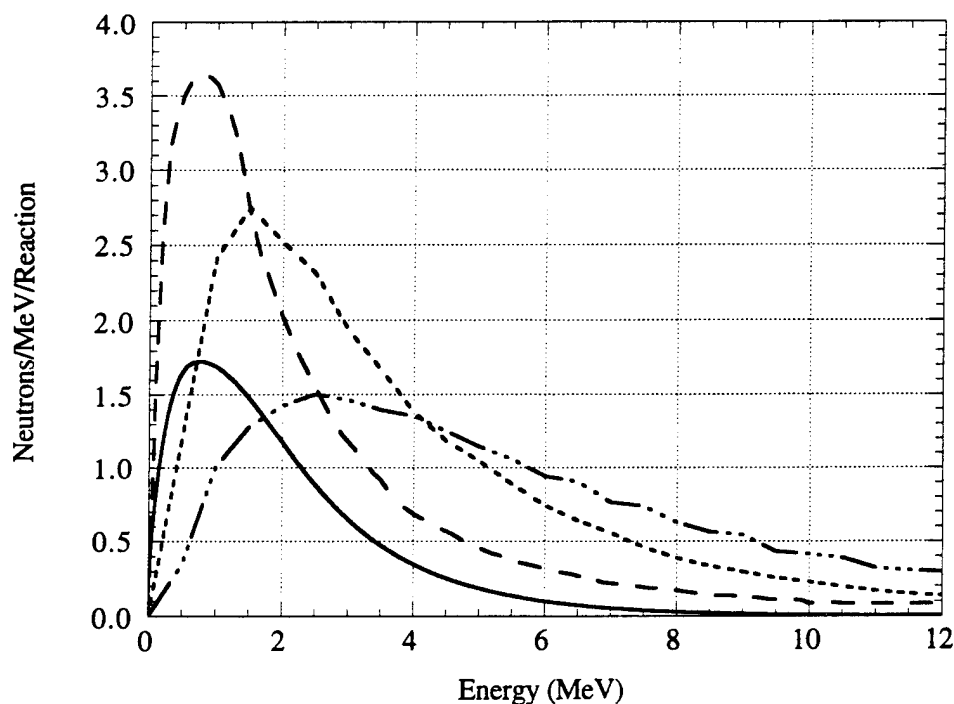


Fig. 7. Secondary neutron energy distributions normalized to absolute yields: 20 MeV (solid line), 155 MeV (dashed line), 300 MeV (dotted line), and 455 MeV (dot-dashed line).

after a scattering collision. Such events lower the average energy of absorption. The 9:1 moderated case is different; at low  $\rho r$  values, there is significant moderation that results in a lower average absorption energy.

As in the 3:1 case, the average energy of absorption falls off rapidly with  $\rho r$ .

Our study has shown that in the presence of a moderator, the average absorption energy of primary and



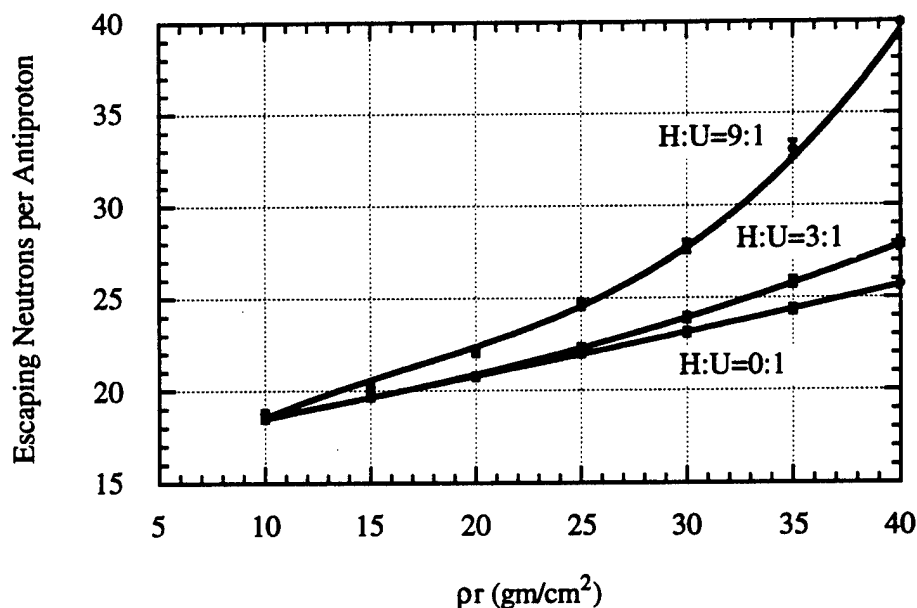


Fig. 8. Yields of neutrons escaping uniformly compressed  $^{235}\text{U}$  targets for three levels of moderation.

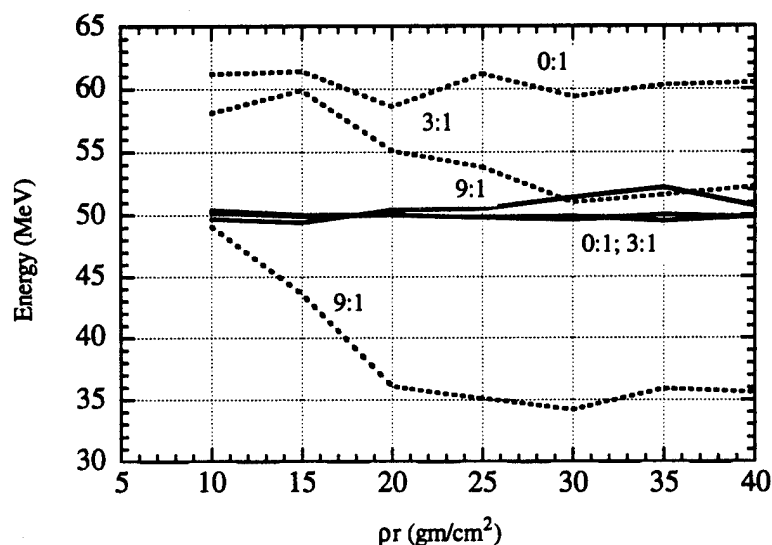


Fig. 9. Average energy of primary neutrons in  $^{235}\text{U}$ : escaping neutrons (solid line) and absorbed neutrons (dotted line).

secondary (not shown) neutrons remains well above 100 keV, thus not accessing regions of substantially higher cross section. However, the addition of a moderator aids in confining neutrons within the target. The probability of the occurrence of a neutron-producing event increases the longer neutrons are confined, which results in larger yields.

### III.B. Uranium-238

Uniformly compressed unmoderated  $^{238}\text{U}$  targets were also studied. The yield of escaping neutrons is

smaller than the yield from  $^{235}\text{U}$  for all values of  $\rho r$  because of the lower neutron-producing  $^{238}\text{U}$  cross section ( $n \rightarrow xn$ ) and multiplicity below 10 MeV (see Figs. 4, 5, and 6). Unmoderated  $^{238}\text{U}$  coefficients for Eq. (1) are listed in Table II. At 20 g/cm<sup>2</sup>, the number of escaping neutrons from a  $^{238}\text{U}$  target is 18.9 neutrons per antiproton (compared with 20.8 neutrons for  $^{235}\text{U}$ ). At 40 g/cm<sup>2</sup>, the numbers of escaping neutrons per antiproton are 21.5 and 25.7 for  $^{238}\text{U}$  and  $^{235}\text{U}$ , respectively. We see that the neutron yield of a  $^{238}\text{U}$  target is lower by 9 to 16% than the yield of the corresponding  $^{235}\text{U}$  target, depending on  $\rho r$ .

TABLE II  
Coefficients for the  $^{238}\text{U}$  Escaped-Neutron Yield

	Hydrogen-to-Uranium Ratio of 0:1
$c_0$ neutron per antiproton	$1.6300\text{E}+1^a$
$c_1$ neutron per antiproton ( $\text{g}/\text{cm}^2$ )	$1.3030\text{E}-1$
$c_2$ neutrons per antiproton ( $\text{g}^2/\text{cm}^4$ )	$0.0000\text{E}+0$
$c_3$ neutrons per antiproton ( $\text{g}^3/\text{cm}^6$ )	$0.0000\text{E}+0$

<sup>a</sup>Read as  $1.6300 \times 10^1$ .

As in the case of  $^{235}\text{U}$ , the addition of a moderator to the  $^{238}\text{U}$  targets could improve the yield of escaping neutrons. The effect of moderation has been shown to improve confinement and not to significantly degrade the neutron energy distribution. Using the yields from the  $^{235}\text{U}$  targets as a representative case, at  $40 \text{ g}/\text{cm}^2$ , one can expect an increase in the yields from  $^{238}\text{U}$  targets between 8% (hydrogen-to-uranium ratio of 3:1) and 50% (hydrogen-to-uranium ratio of 9:1).

#### IV. EXPECTED YIELDS FROM THE SHIVA STAR EXPERIMENT

The CALE code is used to model the compression of a 27-g  $^{235}\text{U}$  target. Four cases are considered with varying initial plasma conditions resulting in different density profiles at peak compression.<sup>5</sup> The code calculates density conditions throughout the target and reports the density profile every 10 ns. Antiprotons are injected at peak compression. Moderated cases were evaluated by using the same density profiles, although it is recognized that SHIVA Star will not be able to compress a moderated target as well as a pure uranium target.

The CALE and HYDRAD codes have demonstrated that there is little evaporation of the target around the point of peak compression. For example, CALE finds that the electric current (i.e., electrical conductivity) in the target is nearly constant over the compression cycle.

At peak compression, the target's density profile changes slowly with respect to the speed at which the neutron reaction rate proceeds. The changes in the density profile over 10 ns are small and only slightly effect the evolution of neutron production within the target.

Results for the unmoderated and moderated (hydrogen-to-uranium ratio of 3:1) CALE cases are shown in Tables III and IV, respectively. Initial conditions of the working fluid listed in Tables III and IV are discussed in Ref. 5. The comparison of CALE results with results for uniformly compressed targets (Fig. 8) shows good agreement. Yields from uniformly compressed targets are similar to the yields of the CALE cases at similar  $\rho r$ .

Currently, the SCATTER code is modeling neutrons that arise directly from the intranuclear cascade (INC). However, at SHIVA Star, neutrons will also be produced when high-energy pions from INC interact in the target and the aluminum linear. Calculation of neutron yields produced by these pions is found in another paper.<sup>6</sup> These mechanisms represent a significant additional source of neutrons.

Wienke, Seamon, and Madland<sup>17</sup> have described how a multigroup microfission calculation using the antiproton source might be done with transport theory. Specifically, they set up 30 energy groups, dedicating 8 to the region below 1 keV and 1 to the region above 15 MeV. In the most moderated case considered in this study, only 0.02% of the total neutron population dropped below 1 keV. Therefore, without modification, this method seems inappropriate for this application.

#### V. CONCLUSIONS

This study has explored the behavior of neutron reactions that are initiated by antiproton annihilations on microfission targets. In particular, special effort has been directed toward predicting neutron yields for the SHIVA Star antiproton experiment.

Results for uniformly compressed  $^{235}\text{U}$  targets show that neutron yields are described by a power series in  $\rho r$ . Furthermore, adding a hydrogen moderator increased yields at all compression levels because of enhanced confinement of neutrons. This increase is small

TABLE III  
Neutron Yields for Unmoderated  $^{235}\text{U}$  CALE Cases

	Case 1 <sup>a</sup>	Case 2 <sup>b</sup>	Case 3 <sup>c</sup>	Case 4 <sup>d</sup>
Average $\rho r$ ( $\text{g}/\text{cm}^2$ )	21.4	21.6	21.0	19.3
Neutron yield per antiproton	$21.56 \pm 0.16$	$21.69 \pm 0.16$	$21.50 \pm 0.21$	$21.50 \pm 0.21$

<sup>a</sup>Initial plasma temperature 2.0 eV and initial density  $1 \times 10^{19} \text{ ion}/\text{cm}^3$ .

<sup>b</sup>Initial plasma temperature 2.0 eV and initial density  $6 \times 10^{19} \text{ ion}/\text{cm}^3$ .

<sup>c</sup>Initial plasma temperature 5.0 eV and initial density  $1 \times 10^{19} \text{ ion}/\text{cm}^3$ .

<sup>d</sup>Initial plasma temperature 5.0 eV and initial density  $6 \times 10^{19} \text{ ion}/\text{cm}^3$ .

TABLE IV  
Neutron Yields for Moderated (Hydrogen-to-Uranium Ratio of 3:1)  $^{235}\text{U}$  CALE Cases

	Case 1 <sup>a</sup>	Case 2 <sup>b</sup>	Case 3 <sup>c</sup>	Case 4 <sup>d</sup>
Average $\rho r$ (g/cm <sup>2</sup> )	21.4	21.6	21.0	19.3
Neutron yield per antiproton	$21.71 \pm 0.21$	$21.87 \pm 0.16$	$21.72 \pm 0.21$	$21.92 \pm 0.21$

<sup>a</sup>Initial plasma temperature 2.0 eV and initial density  $1 \times 10^{19}$  ion/cm<sup>3</sup>.

<sup>b</sup>Initial plasma temperature 2.0 eV and initial density  $6 \times 10^{19}$  ion/cm<sup>3</sup>.

<sup>c</sup>Initial plasma temperature 5.0 eV and initial density  $1 \times 10^{19}$  ion/cm<sup>3</sup>.

<sup>d</sup>Initial plasma temperature 5.0 eV and initial density  $6 \times 10^{19}$  ion/cm<sup>3</sup>.

at low  $\rho r$  but increases with higher  $\rho r$ . Studies of average energy and interaction profiles for primary and secondary neutron populations indicate that the effect of moderation is to confine the neutrons in the target, rather than degrading them into regions of higher cross section.

Modeling of unmoderated  $^{238}\text{U}$  targets has demonstrated 9 to 16% lower yields of escaping neutrons than yields from  $^{235}\text{U}$  targets. The yield of escaping neutrons from moderated  $^{238}\text{U}$  targets are expected to increase analogously with the yields from the moderated  $^{235}\text{U}$  targets.

Four SHIVA Star moderated (hydrogen-to-uranium ratios of 3:1) and unmoderated  $^{235}\text{U}$  targets with differing initial plasma density and temperature conditions were evaluated. Results for the cases, which had average  $\rho r$  values of  $\sim 21$  g/cm<sup>2</sup>, differ only slightly. The SCATTER code predicts an average yield per antiproton for these targets of  $21.8 \pm 0.2$ , which is in good agreement with uniformly compressed cases of similar  $\rho r$ .

#### ACKNOWLEDGMENT

This work was supported in part by the U.S. Air Force Office of Scientific Research and Jet Propulsion Laboratory (National Aeronautics and Space Administration).

#### REFERENCES

1. G. A. ASKAR'YAN et al., "Supercompression of Matter by Reaction Pressure to Obtain Microcritical Masses of Fissioning Matter, to Obtain Ultrastrong Magnetic Fields, and to Accelerate Particles," *JETP Lett.*, **17**, 424 (1973).
2. F. WINTERBERG, "The Possibility of Micro-Fission Chain-Reactions and Their Application to the Controlled Release of Thermonuclear Energy," *Z. NATURFORSCH*, **28a**, 900 (1973); see also "The Possibility of Microfission Explosions by Laser or Relativistic Electron-Beam High Density Compression," *Lett. Nuovo Cimento*, **6**, 407 (1973); see also "Micro-Fission Explosions and Controlled Release of Thermonuclear Energy," *Nature*, **241**, 449 (1973).
3. R. A. LEWIS, R. NEWTON, G. A. SMITH, and R. J. KANZLEITER, "Antiproton-Boosted Microfission," *Nucl. Sci. Eng.*, **109**, 411 (1991); see also R. A. LEWIS, G. A. SMITH, R. J. KANZLEITER, K. HIGMAN, and R. NEWTON, "Antiproton Boosted Microfission," *Fusion Technol.*, **20**, 1046 (1991).
4. B. CHEN et al., "Neutron Yields and Angular Distributions Produced in Antiproton Annihilation at Rest in Uranium," *Phys. Rev.*, **C45**, 2332 (1992).
5. P.-R. CHIANG et al., "Target Compression by Working Fluids Driven with Solid Liner Implosions," *J. Appl. Phys.*, **76**, 2, 15 (July 1994).
6. K. I. HIGMAN, R. J. NEWTON, R. A. LEWIS, P.-R. CHIANG, and G. A. SMITH, "Containment and Neutron Production by Charged Pions in Antiproton Microfission Experiments," *Nucl. Sci. Eng.*, **118**, 227 (1994).
7. G. A. SMITH, "Applications of Trapped Antiprotons," *Hyperfine Interact.*, **81**, 189 (1993).
8. R. TIPTON, *CALE Users' Manual*, Lawrence Livermore National Laboratory (July 1991); see also *Megagauss Technology and Pulsed Power Applications*, p. 299, C. M. FOWLER, R. S. CAVID, and D. J. ERICKSON, Eds., Plenum Press, New York (1987).
9. C. E. GAZZE, "Neutron Yields for the SHIVA Star Antiproton Microfission Experiment," MS Thesis, The Pennsylvania State University (1993).
10. F. S. ALSMILLER, R. G. ALSMILLER, Jr., T. A. GABRIEL, R. A. LILLIE, and J. BARISH, "A Phenomenological Model for Particle Production from the Collisions of Nucleons and Pions with Fissile Elements at Medium Energies," *Nucl. Sci. Eng.*, **79**, 147 (1981).
11. E. CHEIFITZ et al., "Measurement of the Prompt Neutrons Emitted in the Fission of  $\text{Bi}^{209}$  and  $\text{U}^{238}$  Induced by 155-MeV Protons," *Phys. Rev. C*, **2**, 256 (1970).

12. "ENDF-102 Data Formats and Procedures for the Evaluated Nuclear Data File ENDF-6," BNL-NCS-44945, Brookhaven National Laboratory (1990).
13. J. FRANZ et al., "Total Neutron-Nucleus Cross Sections at Intermediate Energies," *Nucl. Phys.*, **A490**, 667 (1988).
14. W. SCHIMMERLING et al., "Neutron-Nucleus Total and Inelastic Cross Sections: 900 to 2600 MeV/c," *Phys. Rev. C*, **7**, 248 (1973).
15. E. D. MINOR et al., "Charged Pion Spectra and Energy Transfer Following Antiproton Annihilation at Rest in Carbon and Uranium," *Z. Phys. A*, **336**, 461 (1990).
16. "CCC-200/MCNP, Version 3A Code," Oak Ridge National Laboratory (1986).
17. B. R. WIENKE, R. E. SEAMON, and D. G. MADLAND, "Multigroup Antiproton Transport and Fission," *Nucl. Sci. Eng.*, **113**, 86 (1993).

## Containment and Neutron Production by Charged Pions in Antiproton Microfission Experiments

Kumiko I. Higman and Richard J. Newton

*The Pennsylvania State University, Department of Nuclear Engineering  
University Park, Pennsylvania 16802*

and

Raymond A. Lewis, Pi-Ren Chiang, and Gerald A. Smith

*The Pennsylvania State University, Department of Physics  
Laboratory for Elementary Particle Science, University Park, Pennsylvania 16802*

*Received November 8, 1993*

*Accepted August 5, 1994*

**Abstract**—*Containment and interaction of charged pions in a solid linear implosion system are simulated. Pions are generated from annihilation of antiprotons at the surface of a compressed target. A three-dimensional Monte Carlo code has been developed to simulate the interaction of charged pions with the system. Neutron yields are presented for several 27-g uranium targets compressed under different initial plasma conditions. Effects on neutron yields from the diffused magnetic field and density profiles at peak compression are discussed. Results show that the magnetic field at peak compression significantly increases overall neutron yields.*

### I. INTRODUCTION

Antiproton annihilation has been shown to be a strong source of neutrons<sup>1</sup> and charged pions.<sup>2</sup> Under conditions of high density, the neutrons, and neutrons produced by charged pions, enable a significant reduction in the burn time and, hence, size of fissile targets. The concept of antiproton microfission will be tested by compressing a small fissile target with an electromagnetically imploded solid liner.<sup>3</sup> A subcritical test is possible at this time by using the currently limited numbers of antiprotons available. The experiment employs hydrogen plasma as a working fluid to compress the target and will be conducted at the SHIVA Star facility, located at the Phillips Laboratory, Kirtland Air Force Base, New Mexico. The solid liner implosion system is suitable because of its relatively high efficiency of energy conversion and capability of compressing high-Z materials.

Pions from antiproton annihilation have a mass of about one-seventh of a nucleon mass and are produced in three charge states. On the average,  $1.48 \pi^-$ ,  $1.36 \pi^0$ , and  $0.99 \pi^+$  are produced per annihilation in ura-

anium, with an average kinetic energy of 232 MeV/pion. The  $\pi^0$ 's decay into two gamma rays with a lifetime of  $8.4 \times 10^{-17}$  s and contribute little to secondary interactions. The 26-ns lifetime of charged pions is long compared with the 1 to 2 ns required for a pion to escape or stop in the target. The  $\pi^-$  can stop in nuclear targets and produce secondary interactions at rest, whereas  $\pi^+$  can interact only in flight because of their repulsion from positively charged nuclei.

In the absence of pion interactions, the experiment will yield an  $\approx 20\%$  increase in neutrons relative to the primary source<sup>1</sup> of neutrons 16.3. The actual neutron yield will consist of primary neutrons and secondary neutrons induced by antiprotons, plus neutrons created by charged pions. Since path lengths for charged pions are increased because of the magnetic field diffused around the target, neutron multiplicities from charged pions are expected to be enhanced.

The PICALE three-dimensional Monte Carlo code has been developed to simulate containment and interactions of charged pions in the apparatus at peak compression.<sup>4</sup> The PICALE code is described in Sec. II. Results obtained from PICALE for different initial

plasma conditions in SHIVA Star are presented, and effects on neutron yields from magnetic field and density profiles at peak compression are discussed in Sec. III. Results are summarized in Sec. IV.

## II. PION-CONTAINMENT MODEL

### II.A. Simulation of Pion Motion and Interactions

The PICALE code tracks the motion of charged pions in a magnetic field and simulates interactions of pions with the target (uranium) and aluminum liner (see Fig. 1) using the Monte Carlo method. Given the initial position and momentum of a pion born on the upper surface of the target, the code updates the pion's position at every time step by integrating the equations of motion. Magnetic field and density profiles in the simulations are calculated by the CALE two-dimensional magnetohydrodynamics code.<sup>5</sup> Because the time scale ( $\approx 1$  to  $2$  ns) for pion interactions is much shorter than the dwell time<sup>3</sup> ( $\approx 400$  ns) of peak compression, the magnetic field and density are assumed to be constant throughout the simulations. The Lorentz force due to the magnetic field is  $240$  MeV/cm, three orders of magnitude larger than the force due to the electric field ( $\approx 90$  keV/cm). Therefore, effects on pion

motion from both the static electric field and that induced by the time-dependent magnetic field are neglected.

Because most of a pion's path length occurs at momenta above  $100$  MeV/c (Ref. 2), charged pions are assumed to lose energy at a constant rate of  $1.09$  MeV/g $\cdot$ cm<sup>2</sup> because of collisions with atomic electrons.<sup>6</sup> Interactions of pions with a nucleus include elastic scattering, inelastic scattering, and absorption. Elastic scattering at high energies shows strong forward diffraction scattering, and energy loss is assumed negligible in collisions with nuclei.

In an inelastic scattering, a pion may undergo charge-exchange. However, experiments<sup>7,8</sup> show that the fraction of charge-exchange in the total reaction cross section is small ( $< 1\%$ ). The inelastic scattering angle and energy distributions of charged pions on nuclei are assumed to be uniform in the center-of-mass and laboratory frames, respectively.<sup>7,8</sup>

The energy range of measured neutron yields and cross sections from pions is limited to low momenta.<sup>7-9</sup> Since the momentum cutoff of pion spectra from antiproton annihilation is  $1000$  MeV/c (Ref. 2), it is necessary to further model neutron yields and cross sections due to pions up to this energy.

### II.B. Energy-Dependent Neutron Yields

Figure 2 shows neutron yields versus energy deposited in uranium and aluminum nuclei for different projectiles. The solid curve is a characterization of the yield in uranium, drawn through points at  $455$  MeV (antiprotons at rest<sup>2</sup>),  $140$  MeV ( $\pi^-$  at rest<sup>10</sup>), and  $20$  to  $50$  MeV (protons in flight<sup>11</sup>). Based on the smooth energy dependence, we conclude that neutron yields do not depend on the incident particle but rather on the amount of energy deposited into a nucleus. Production of neutrons in uranium can be induced by absorption and inelastic scattering of charged pions, and two mechanisms are treated separately in the simulation.

Because of lack of data, neutron yields for aluminum are scaled from uranium. A correlation between the average number of ejectiles from annihilation of an antiproton and the atomic mass number of the target is<sup>12</sup>

$$N_{eject} \propto A^{0.43} \quad (1)$$

We assume that the number of emitted neutrons is proportional to  $N_{eject}$ , and energy-dependent neutron yields for aluminum are scaled from those for uranium. As seen in Fig. 2, data from Madey et al.<sup>13</sup> are consistent with the scaled curve for aluminum (dotted curve).

### II.C. Energy-Dependent Cross Sections

Cross sections from Ashery et al.<sup>8</sup> for absorption and inelastic scattering of  $\pi^+$  and  $\pi^-$  in aluminum are used. Although data for uranium are not available, those for bismuth can be used to infer cross sections for

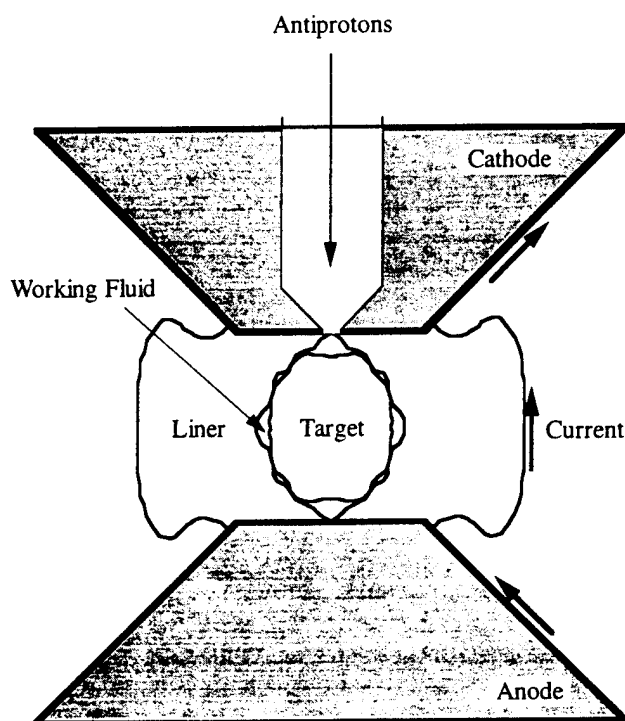


Fig. 1. Schematic of spherical solid liner implosion system with working fluid shown at peak compression.

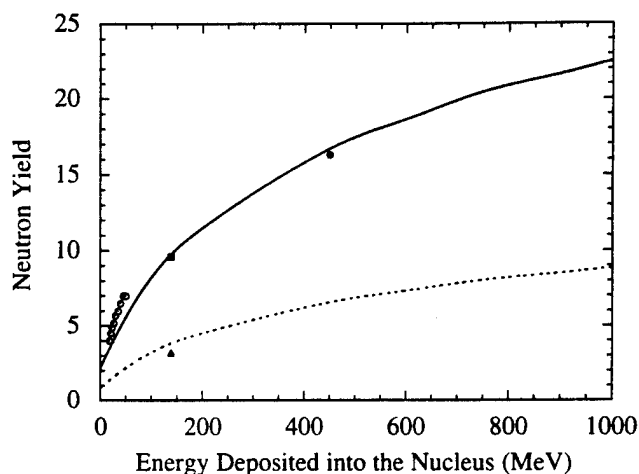


Fig. 2. Neutron yields versus energy deposited into the nucleus for uranium (solid curve) and aluminum (dashed curve). Data are taken from Refs. 2 (solid circle), 10 (solid square), 12 (open circles), and 13 (solid triangle).

uranium. Absorption and inelastic scattering cross sections for uranium can be scaled by using<sup>8</sup>

$$\sigma_m \propto A^{q_m(E)}, \quad (2)$$

where  $q_m(E)$  is an energy-dependent exponent,  $A$  is the target atomic mass, and the subscript  $m$  indicates the reaction, i.e., absorption, inelastic scattering, etc.

The exponents  $q_m(E)$  of  $\pi^+$  for various types of interactions and the effective number  $N_{eff}$  of nucleons participating in the process are obtained from Ashery et al.<sup>8</sup> For  $\pi^-$ , data for  $q_m(E)$  are available<sup>14</sup> only at 125 and 165 MeV and are not sufficient to establish scaling. Therefore, the same  $q_m(E)$  for  $\pi^+$  is used for  $\pi^-$  as an approximation. Equation (2) is used, and cross sections for uranium are scaled as

$$\sigma_{m,U}(E) = \sigma_{m,Bi}(E) \left[ \frac{238}{209} \right]^{q_m(E)}. \quad (3)$$

Cross sections for interactions between charged pions and uranium at energies above 315 MeV are not available in the literature; however, they can be reasonably inferred from data from other projectiles. Reaction cross sections for uranium with proton incident energies<sup>15</sup> up to 3 GeV, total and reaction cross sections for uranium and aluminum with neutron incident energies<sup>16</sup> of 0.9 to 2.6 GeV, and total cross sections for uranium and aluminum at intermediate incident neutron energies<sup>17</sup> (160 to 575 MeV) are used to infer cross sections for charged pions.

For an opaque nucleus, the geometric limit,  $2\pi R^2$ , for the total cross section, is the sum of cross sections due to absorption and diffractive processes, and both cross sections approach the geometric limit asymptotically.<sup>17</sup> Therefore, it is reasonable to assume that both

absorption and inelastic scattering cross sections are approximately constant at high energies. Both the reaction and absorption cross sections of  $\pi^+$  and  $\pi^-$  for uranium and aluminum for energies above 400 MeV are interpolated between data at energies below 315 MeV and values at higher energies.

To model absorption cross sections at low energies, we used data obtained by Navon et al.<sup>18</sup> at 50 MeV. The data do not include uranium and aluminum. However, a correlation between absorption cross sections and atomic mass number at 50 MeV is given, and cross sections for uranium and aluminum are deduced by using this correlation.

For cross sections at energies below 50 MeV, the following features<sup>19</sup> are included:

1. The absorption cross section of  $\pi^-$  increases to infinity as the pion energy approaches zero.
2. The absorption cross section of  $\pi^+$  drops to zero at  $\sim 20$  MeV for uranium and 4 MeV for aluminum, energies required to penetrate the Coulomb barrier.
3. The inelastic scattering cross sections of  $\pi^+$  and  $\pi^-$  become very small at low energies and rapidly drop to zero at a threshold value.

Gathering together all of the measurements and features discussed earlier, energy-dependent cross sections for  $\pi^-$  and  $\pi^+$  interactions with uranium and aluminum nuclei are shown in Figs. 3 and 4 (for uranium) and Figs. 5 and 6 (for aluminum), respectively. Because these cross sections are model-dependent generalizations of several experiments over a wide range of energies, both statistical and systematic errors must be considered.

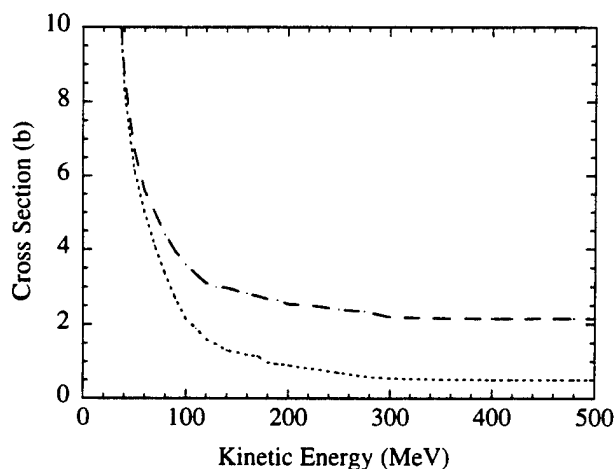


Fig. 3. Energy-dependent neutron producing cross sections for  $\pi^-$  interactions with uranium: inelastic (dashed curve) and absorption (dot-dashed curve).

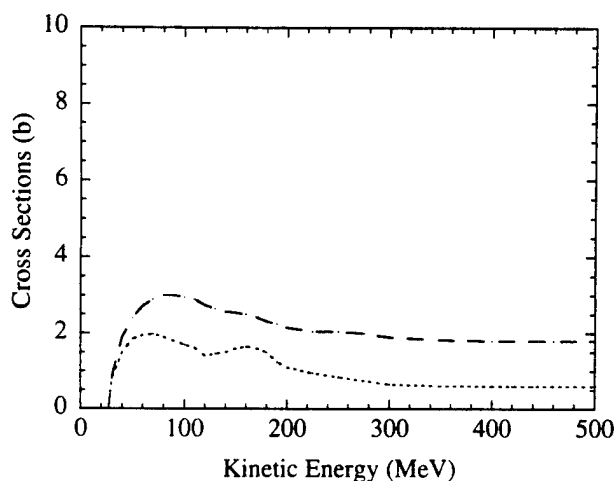


Fig. 4. Energy-dependent neutron producing cross sections for  $\pi^+$  interactions with uranium: inelastic (dashed curve) and absorption (dot-dashed curve).

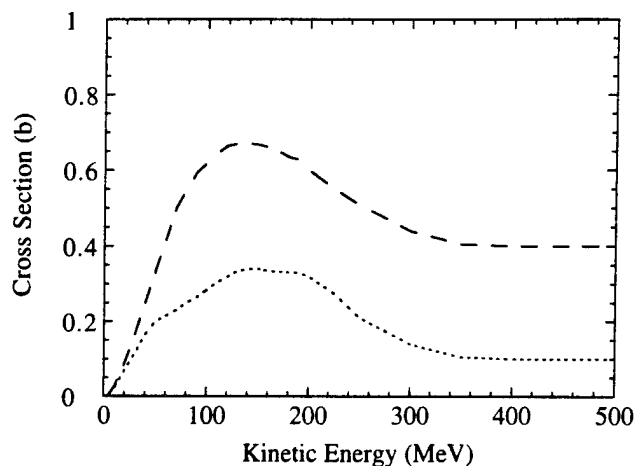


Fig. 6. Energy-dependent neutron producing cross sections for  $\pi^+$  interactions with aluminum: inelastic (dashed curve) and absorption (dot-dashed curve).

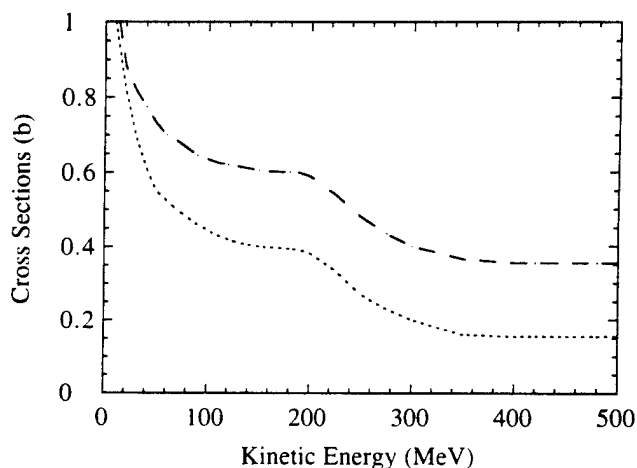


Fig. 5. Energy-dependent neutron producing cross sections for  $\pi^-$  interactions with aluminum: inelastic (dashed curve) and absorption (dot-dashed curve).

For the inelastic cross sections given, only one set of experimental data with small statistical errors (a few percent) was available. The errors are dominated by systematics related to the validity of the energy-scaling model employed, which we estimate to be  $\sim 10\%$  at any energy.

For the absorption cross sections given, up to four different sets of experimental data were used, which exhibited individual statistical and systematic errors among themselves of typically a few percent and 20%, respectively. When combined with estimated model-dependent errors (10%), we estimate overall errors at any energy to be  $\sim 25\%$ .

### III. RESULTS AND DISCUSSION

#### III.A. Effects of Magnetic Field and Density Profile

The preferred direction of antiproton injection is opposite to the direction of current (see Fig. 1). This preference results from the charge asymmetry and relative cross sections of pions. With such an arrangement, a  $\pi^-$  turns toward the target and a  $\pi^+$  turns away from the target. Since a  $\pi^-$  produces more neutrons than a  $\pi^+$ , neutron yields will be enhanced by choosing this direction for antiproton injection. In addition, as discussed later, the magnetic field direction also helps focus the antiproton beam.

The CALE code results for the compression of a 27-g target with initial plasma conditions of 2 eV and  $1 \times 10^{19} \text{ cm}^{-3}$  are used for the simulations.<sup>3</sup> At peak compression, the target has density fluctuations up to  $90 \text{ g/cm}^3$ , and magnetic fields of several hundred tesla. Results of simulations with/without target compression and/or magnetic field are summarized in Table I. Case A is the baseline simulation, wherein the antiprotons are injected before compression. At peak compression with the magnetic field (case B), the neutron yield increases by a factor of 3.6 because of the combination of compression and magnetic field. For case C, with the magnetic field ignored in the simulation, the neutron yield increases by only a factor of 2.0, which implies that the magnetic field accounts for a factor of 1.8 increase in yield. Simulations with the CALE code predict no significant target asymmetries or instabilities, e.g., formation of jets of liner or target material. This has been recently partially confirmed in SHIVA Star liner firings in vacuum.<sup>20</sup>



TABLE I

Average Pathlengths of Pions in Target and Liner, Fraction of Stopped  $\pi^-$  in Target, and Resultant Neutron Yields for 27-g Target, and 2-eV and  $1 \times 10^{19} \text{ cm}^{-3}$  Initial Working Fluid Conditions

Items	Case A <sup>a</sup>	Case B <sup>b</sup>	Case C <sup>c</sup>
Average $l_{\text{path}}$ of $\pi^-$ in target (mm)	$3.179 \pm 0.027$	$3.435 \pm 0.025$	$2.604 \pm 0.020$
Average $l_{\text{path}}$ of $\pi^+$ in target (mm)	$3.233 \pm 0.019$	$2.825 \pm 0.017$	$2.709 \pm 0.015$
Average $l_{\text{path}}$ of $\pi^-$ in liner (mm)	$0.439 \pm 0.003$	$15.181 \pm 0.123$	$7.828 \pm 0.048$
Average $l_{\text{path}}$ of $\pi^+$ in liner (mm)	$0.445 \pm 0.002$	$9.725 \pm 0.062$	$8.133 \pm 0.036$
Percent of stopped $\pi^-$ in target (%)	0.46	4.73	1.19
Neutron yield from target per $\bar{p}$	$1.335 \pm 0.022$	$3.810 \pm 0.038$	$2.151 \pm 0.028$
Neutron yield from liner per $\bar{p}$	$0.016 \pm 0.001$	$1.001 \pm 0.012$	$0.557 \pm 0.009$
Total neutron yield per $\bar{p}$	$1.351 \pm 0.022$	$4.811 \pm 0.040$	$2.708 \pm 0.029$

<sup>a</sup>Case A: uncompressed target.

<sup>b</sup>Case B: CALE density profiles and magnetic field.

<sup>c</sup>Case C: CALE density profiles without magnetic field.

Orbits of three typical charged pions in the magnetic field are shown in Fig. 7 (elevation view as shown in Fig. 1) and Fig. 8 (top view). Path lengths of charged pions, especially in the liner, increase because of the magnetic field as seen in Table I. Comparing cases B and C in Table I, we see that the magnetic field increases the path lengths of charged pions, especially  $\pi^-$ , by factors ranging from 1.04 to 1.94. The percentage of stopped  $\pi^-$  is also increased by nearly a factor of 4.

### III.B. Neutron Yields

In this section, neutron yields for four CALE cases are presented. These results, and their corresponding initial plasma conditions, are summarized in Table II. For comparison, case A discussed in Sec. III.A is also listed.

Case 2 gives the largest yield of  $4.574 \pm 0.042$  neutrons from the target. The average target density for case 2 is the largest among all cases, thus increasing the interactions between the pions and the target. The magnetic field also increases path lengths of  $\pi^-$  and  $\pi^+$ ; therefore, the neutron yield is further enhanced. Effects from the magnetic field can be seen in the difference in  $\pi^-$  and  $\pi^+$  path lengths. Since the magnetic field direction increases the path length of  $\pi^-$  more than that of  $\pi^+$ , a stronger magnetic field results in a greater difference in the path lengths. As seen in Table II, the differences in path lengths of  $\pi^-$  and  $\pi^+$  in case 2 are the largest among the four cases. Therefore, the magnetic field enhances the neutron yield the most in case 2.

Azimuthal magnetic field contours for case 2 are shown in Fig. 9. A large magnetic field of  $\approx 1$  MG is predicted within 0.1 cm of the beam axis ( $r = 0$ ). By Ampere's law, the magnetic field must decrease to zero on the axis. An antiproton moving off the beamline will be deflected radially inward by the Lorentz force. Tak-

ing into account energy loss per unit length,  $dE/ds$ , due to antiproton interactions with electrons, we numerically ray-trace antiproton trajectories in this field. Typical trajectories inside the compression chamber are shown in Fig. 10. As seen, a beam with a maximum spread of 0.9 mm from  $r = 0$  and initial energy of 4 MeV hits the target surface within a 0.2-mm radius from  $r = 0$ . In other words, the chosen magnetic field direction focuses the antiproton beam onto the target.

Neutron yields from the liner are greatly enhanced (factor of 40 to 60), compared with those for case A, for all four cases. As seen in Fig. 9, this is because the magnetic field is much stronger in the liner than in the

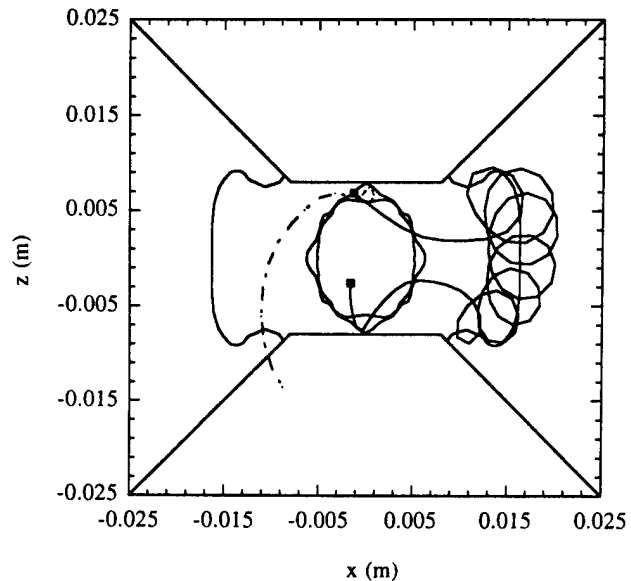


Fig. 7. Three typical pion orbits seen in the elevation view.

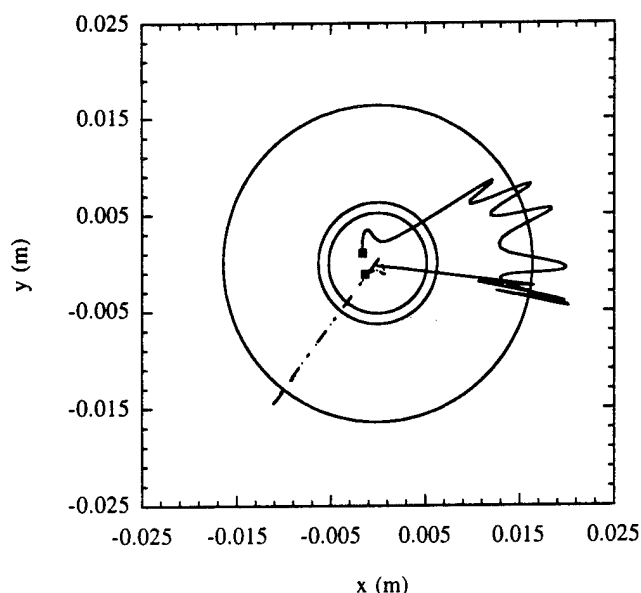


Fig. 8. Three typical pion orbits from Fig. 7 seen in the top view.

target, and the liner thickness is greatly increased under compression; hence, the average path length of pions is dramatically larger in the liner under compression.

The magnetic field profile at peak compression differs somewhat for different initial plasma conditions. As a consequence, neutron yields induced by charged pions are more sensitive to initial plasma conditions than those induced by primary neutrons generated by annihilation of antiprotons. We illustrate as follows: The gain in neutron yields<sup>1</sup> from the compressed target induced by parent neutrons is enhanced by a factor of  $\approx 1.8$  compared with the uncompressed target case A, whereas the factor varies between 1.95 and 3.43 for neutron yields induced by charged pions.

The version of CALE used in these simulations does not include radiation and thermal conduction. Including thermal radiation, we find that the target density at peak compression is relatively unchanged for cases 1, 2, and 3 and increases<sup>3</sup> by 10% for case 4. Therefore, neutron yields at peak compression including radiation and thermal conduction should be similar to the results in Table II.

#### IV. SUMMARY

Containment of charged pions generated at annihilation of an antiproton have been simulated. Neutron yields resulting from interactions between charged pions and the target and liner are obtained. The results are summarized as follows:

1. The magnetic field at peak compression increases neutron yields induced by charged pions by a factor

TABLE II

Average Pathlengths of Pions in Target and Liner, Fraction of Stopped  $\pi^-$  in Target, and Resultant Neutron Yields for 27-g Target and Four Cases (1 Through 4) of Initial Working Fluid Conditions

Items	Case A <sup>a</sup>	Case 1 (2 eV, $1 \times 10^{19} \text{ cm}^{-3}$ )	Case 2 (2 eV, $6 \times 10^{19} \text{ cm}^{-3}$ )	Case 3 (5 eV, $1 \times 10^{19} \text{ cm}^{-3}$ )	Case 4 (5 eV, $6 \times 10^{19} \text{ cm}^{-3}$ )
Average $l_{\text{path}}$ of $\pi^-$ in target (mm)	$3.179 \pm 0.027$	$3.435 \pm 0.025$	$4.041 \pm 0.029$	$3.334 \pm 0.024$	$3.111 \pm 0.024$
Average $l_{\text{path}}$ of $\pi^+$ in target (mm)	$3.233 \pm 0.019$	$2.825 \pm 0.017$	$2.834 \pm 0.018$	$2.960 \pm 0.018$	$3.180 \pm 0.019$
Average $l_{\text{path}}$ of $\pi^-$ in liner (mm)	$0.439 \pm 0.003$	$15.181 \pm 0.123$	$15.675 \pm 0.124$	$13.326 \pm 0.114$	$10.955 \pm 0.085$
Average $l_{\text{path}}$ of $\pi^+$ in liner (mm)	$0.445 \pm 0.002$	$9.725 \pm 0.062$	$9.102 \pm 0.056$	$9.829 \pm 0.067$	$10.273 \pm 0.066$
Percent of stopped $\pi^-$ in target (%)	0.46	4.73	5.18	3.60	3.13
Neutron yield from target per $\bar{p}$	$1.335 \pm 0.022$	$3.810 \pm 0.038$	$4.574 \pm 0.042$	$3.365 \pm 0.035$	$2.609 \pm 0.031$
Neutron yield from liner per $\bar{p}$	$0.016 \pm 0.001$	$1.001 \pm 0.012$	$0.987 \pm 0.012$	$0.824 \pm 0.011$	$0.666 \pm 0.010$
Neutron yield from target and liner per $\bar{p}$	$1.351 \pm 0.022$	$4.811 \pm 0.040$	$5.561 \pm 0.044$	$4.189 \pm 0.037$	$3.275 \pm 0.033$
Neutron yield from target induced by parent neutrons <sup>1</sup>	$1.63 \pm 0.03$	$2.94 \pm 0.04$	$3.02 \pm 0.04$	$2.91 \pm 0.05$	$2.91 \pm 0.05$
Total neutron yield per $\bar{p}$ <sup>b</sup>	19.28	24.05	24.88	23.40	22.49

<sup>a</sup>Case A from Table I is repeated for comparison.

<sup>b</sup>Includes primary neutron yield of  $16.3 \text{ n}/\bar{p}$ .

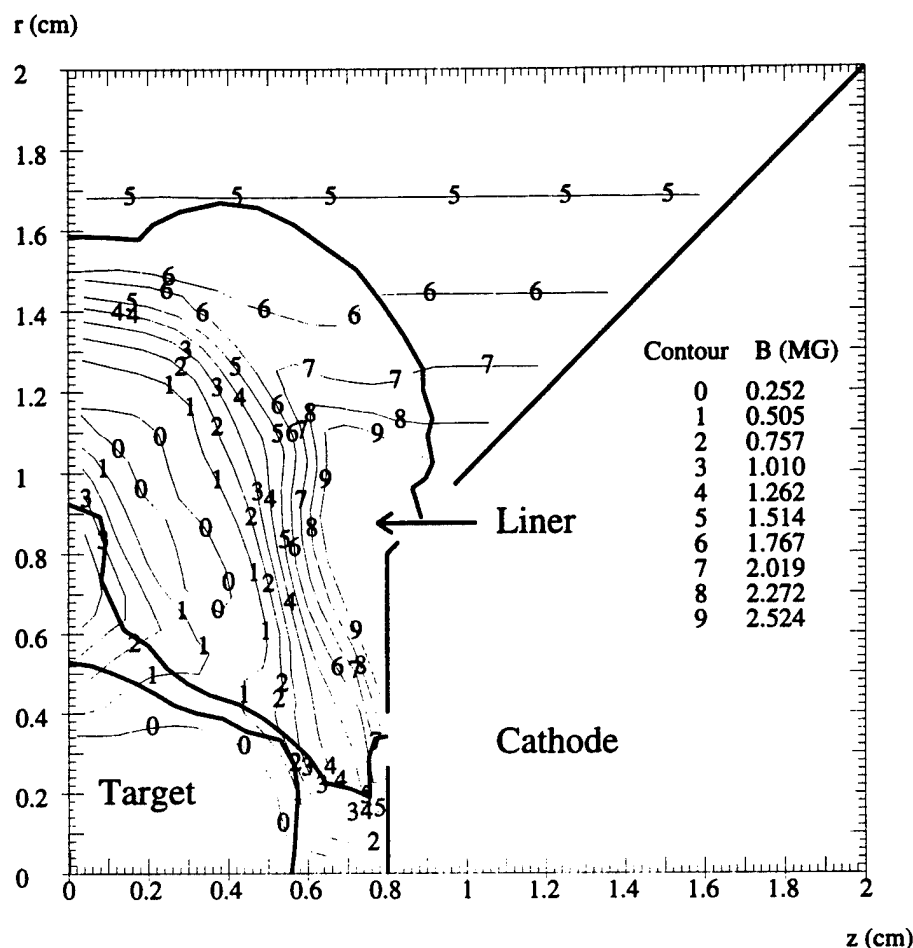


Fig. 9. Magnetic field profiles at peak compression for case 2 (Table II).

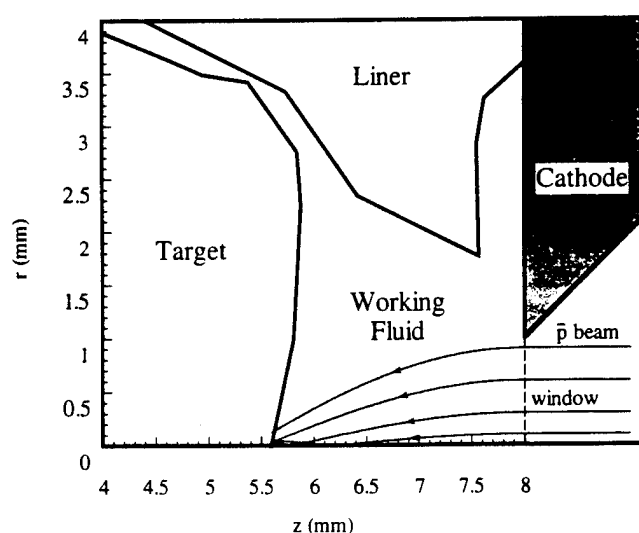


Fig. 10. Enlarged view of target, working fluid region showing focusing of antiproton beam rays (solid lines).

of  $\approx 2.4$  to 4.1 over yields with an uncompressed target without magnetic field.

2. Neutron yields induced by charged pions are sensitive to initial plasma conditions used for compression, since different initial plasma conditions significantly change the magnetic field profile at peak compression.

3. The highest neutron yields induced by charged pions per antiproton are 4.6 from the target and 1.0 from the liner. Including 16.3 primary neutrons, 3.0 neutrons induced by parent neutrons,<sup>1</sup> and 5.6 neutrons induced by pions, approximately 25 neutrons are produced from the target and liner at annihilation. This represents a gain of a factor of 1.3 over an uncompressed target.

#### ACKNOWLEDGMENT

This work was supported in part by the U.S. Air Force Office of Scientific Research and the Jet Propulsion Laboratory (National Aeronautics and Space Administration).

## REFERENCES

1. C. E. GAZZE, R. J. NEWTON, R. A. LEWIS, P. R. CHIANG, and G. A. SMITH, "Neutron Yields for Antiproton Microfission Experiments," *Nucl. Sci. Eng.*, **118**, 217 (1994).
2. E. D. MINOR et al., *Z. Phys. A*, **336**, 461 (1990).
3. P.-R. CHIANG et al., "Target Compression by Working Fluids Driven with Solid Liner Implosions," *J. Appl. Phys.*, **76**, 2, 15 (July 1994).
4. K. I. HIGMAN, "Compression and Pion Recirculation in Antiproton-Induced Microfission," PhD Thesis, The Pennsylvania State University (1993).
5. R. TIPTON, "CALE Users' Manual," Lawrence Livermore National Laboratory (July 1991); see also *Megagauss Technology and Pulsed Power Applications*, p. 299, C. M. FOWLER, R. S. CAVID, and D. J. ERICKSON, Eds., Plenum Press, New York (1987).
6. "Review of Particle Properties," *Phys. Rev. D*, **45**, 2 (June 1992).
7. J. P. SCHIFFER, "Pion Reaction Modes on Nuclei," *Nucl. Phys. A*, **335**, 339 (1980).
8. D. ASHERY et al., "True Absorption and Scattering of Pions on Nuclei," *Phys. Rev. C*, **23**, 2173 (1981).
9. K. NAKAI et al., "Measurements of Cross Sections for Pion Absorption by Nuclei," *Phys. Rev. Lett.*, **44**, 1446 (1980).
10. H. P. ISAAK et al., "Inclusive Neutron Spectra from the Absorption of Stopped Negative Pions in Heavy Nuclei," *Nucl. Phys. A*, **392**, 368 (1983).
11. H. BABA et al., "A Shell Model Nuclear Level Density," *Nucl. Phys. A*, **159**, 625 (1970).
12. J. CUGNON et al., "Nucleus Excitation and Deexcitation Following Antiproton Annihilation at Rest," *Nucl. Phys. A*, **470**, 558 (1987).
13. R. MADEY et al., "Neutrons from Nuclear Capture of Negative Pions," *Phys. Rev. C*, **25**, 3050 (1982).
14. D. ASHERY and J. P. SCHIFFER, "Pion Absorption in Nuclei," *Ann. Rev. Nucl. Part. Sci.*, **36**, 207 (1986).
15. F. S. ALSMILLER, R. G. ALSMILLER, Jr., T. A. GABRIEL, R. A. LILLIE, and J. BARISH, "A Phenomenological Model for Particle Production from the Collisions of Nucleons and Pions with Fissile Elements at Medium Energies," *Nucl. Sci. Eng.*, **79**, 147 (1981).
16. W. SCHIMMERLING et al., "Neutron-Nucleus Total and Inelastic Cross Sections: 900 to 2600 MeV/c," *Phys. Rev. C*, **7**, 248 (1973).
17. J. FRANZ et al., "Total Neutron-Nucleus Cross Sections at Intermediate Energies," *Nucl. Phys. A*, **490**, 667 (1988).
18. I. NAVON et al., "True Absorption and Scattering of 50 MeV Pions," *Phys. Rev. C*, **28**, 2548 (1983).
19. E. SEGRE, *Nuclei and Particles—An Introduction to Nuclear and Subnuclear Physics*, 2nd ed., Benjamin Publishing, Reading, Massachusetts (1977).
20. J. H. DEGNAN et al., "Electromagnetic Implosion of Spherical Liner," submitted to *Phys. Rev. Lett.* (1994).

## ARE ANTIPROTONS FOREVER?

M. H. Holzscheiter.<sup>a</sup> X. Feng.<sup>b</sup> T. Goldman.<sup>c</sup> N. S. P. King.<sup>a</sup>  
R. A. Lewis.<sup>d</sup> M. M. Nieto<sup>ce</sup> and G. A. Smith,<sup>d</sup>

<sup>a</sup>*Physics Division, Los Alamos National Laboratory, Los Alamos, NM 87545, U.S.A.*

<sup>b</sup>*University of Aarhus, Institute for Physics and Astronomy, 8000 Aarhus-C, DENMARK*

<sup>c</sup>*Theoretical Division, Los Alamos National Laboratory, Los Alamos, NM 87545, U.S.A.*

<sup>d</sup>*Pennsylvania State University, University Park, PA 16802, U.S.A.*

<sup>e</sup>*Abteilung für Quantenphysik, Universität Ulm, D-89069 Ulm, GERMANY*

### ABSTRACT

Up to more than one million antiprotons from a single LEAR spill have been captured in a large Penning trap. Surprisingly, when the antiprotons are cooled to energies significantly below 1 eV, the annihilation rate falls below background. Thus, very long storage times for antiprotons have been demonstrated in the trap, even at the compromised vacuum conditions imposed by the experimental set up. The significance for future ultra-low energy experiments is discussed.

PACS: 39.10.+j, 25.43.+t, 35.80.+s, 07.30.-t

An experiment to measure the gravitational acceleration of antiprotons is under preparation at the Low Energy Antiproton Ring (LEAR) at CERN [1]. The experiment proposes to use a time-of-flight technique [2], as pioneered in an experiment which measured the gravitational acceleration of electrons [3]. A critical requirement for such an experiment is a sufficiently large number of antiprotons at sub-eV energies in order to assemble a time-of-flight spectrum with sufficient statistics.

The lowest-energy antiprotons currently available are produced at LEAR. Here antiprotons are delivered at energies as low as 5.9 MeV. A gap of at least 10 orders of magnitude in energy has to be bridged before a meaningful measurement of the gravitational acceleration of antiprotons can be attempted.

To achieve this energy reduction we have developed a large Penning trap system which is matched to the output phase space of the LEAR facility. An antiproton bunch of 200 ns duration, containing up to  $10^9$  antiprotons, is transmitted through a thin foil in which the energy of the individual particles is reduced by multiple collisions. With a properly chosen foil thickness up to 0.6 % of the incident antiprotons emerge from the foil with less than 12.5 keV kinetic energy.

These particles are dynamically captured in the Penning trap by rapidly switching the entrance electrode potential while the bunch is inside the trap volume. Once captured, the antiprotons are cooled by an electron cloud which has been stored in the trap in preparation for the capture. During recent tests of this system we have succeeded in the capture of up to one million antiprotons from a single bunch from LEAR. Up to 65 % of the captured particles were cooled to sub-eV energies and collected in a  $1 \text{ cm}^3$  region at the center of the trap. Presumably, the remaining 35% could not be cooled due to a lack of overlap between antiproton and electron clouds in the radial direction. This can also be seen by the fact that the collection efficiency varies strongly with the beam tune from LEAR, which may change from run to run, causing strong variations in the number of collected antiprotons for otherwise

unchanged conditions (see data points in figure 2 around 130 seconds).

Using a set of scintillators mounted externally to the vacuum system we are able to monitor the annihilation of the antiprotons on the residual gas molecules during the cool-down period. When all particles have been collected in the central well and have been cooled below 1 eV, no annihilation can be observed above the ambient background of approximately 1-2 counts per second.

This result is, at first glance, in contradiction to what one would expect to happen since the annihilation cross section at low energy is generally assumed to have a  $1/v$  dependence. As a result of this effect, antiprotons were stored for significantly long periods of time, even though the residual gas pressure in the system was estimated to be equal to or greater than  $10^{-11}$  Torr. Note that our result is of different origin than the long storage times obtained by the PS196 collaboration [4]. In this experiment, which demonstrated the first capture and subsequent electron cooling of antiprotons from LEAR, a fully cryogenic vacuum system was used. Their long storage time was simply attributed to an extremely-low residual gas density. Effects discussed here were not considered.

We now describe our results in detail and comment on their significance. Charged particles may be confined in vacuum by a superposition of an electric quadrupole field and a strong, axial, magnetic field, a combination typically referred to as a Penning trap [5]. One needs to ensure that all the antiprotons emerging from the degrading foil during a single LEAR pulse and having a kinetic energy of less than 12.5 keV are still within the trap volume when the potential at the entrance electrode is ramped up. This requires an axial dimension of the trap of about 50 cm.

To meet this requirement we have constructed an 'open-end-cap' Penning trap [6]. It contains 5 cylindrical electrodes of inside diameters 2.8 cm and with other dimensions carefully chosen to allow generation of a harmonic potential at the center. Additionally there are two high-voltage electrodes, located at the entrance and the

exit of the trap. The entrance electrode consists of a 5 mil, gold-coated, aluminum foil of diameter 0.6 cm, which also serves as the degrading foil. The exit electrode was chosen to be an open cylinder (of inside diameter 2.8 cm) to allow ejection of the antiprotons from the trap subsequent to their capture and cooling. The electric potential to the innermost electrodes was  $-26$  Volts for the end-caps,  $+4$  Volts for the central ring, and ground potential for the compensation electrodes. This formed a harmonic well with a depth of 30 Volts. The entrance and exit electrodes defining the 50 cm long catching trap were initially set to  $-12.5$  kV, and lowered to 10 kV 8 seconds after capture.

This trap is located in the bore of a superconducting magnet capable of producing an axial magnetic field of up to 6 Tesla. Figure 1 displays a schematic lay-out of the entire set-up, including the location of the external scintillators used to monitor antiproton annihilations.

The following is a brief description of a normal measurement cycle. The central, harmonic well of the trap is preloaded with typically  $10^9$  electrons from an electron gun located in the fringe field of the magnet. These electrons quickly cool by synchrotron radiation to equilibrium with the ambient temperature of the system ( $\approx 10$  K). Initially the entrance foil potential is held at ground while the exit electrode is at full potential. Antiprotons from LEAR traverse the beam profile monitor, generating a trigger for the high-voltage switch to the entrance foil. The antiprotons are slowed down in the foil. Those emerging from it at kinetic energies below the exit electrode potential are reflected back towards the entrance. The potential at the entrance electrode is ramped up to the desired potential in less than 100 ns by a commercial switch [7]. This captures the antiprotons in the 50 cm long (non-harmonic) well of this "catching trap." Due to scattering on the cold electrons, the stored antiprotons lose energy and eventually collect in the inner, harmonic region of the trap.

Antiprotons stored in either the the long, non-harmonic well or the inner, har-



monic well of the trap can be detected by lowering the respective electrical potentials. Escaping antiprotons will follow the magnetic field lines, strike the surface of the down-stream radiation baffle, and annihilate. External scintillators S5-S8 (see figure 1) detect the annihilations and the information is stored in a multichannel analyzer. If the time constant for reducing the potential is chosen to be much longer than the oscillation period in the trap, particles will constantly probe the height of the barrier and escape when this barrier has become lower than their energy. The resulting 'time-of-arrival' spectrum directly reflects the energy distribution of the particles in the trap before the release.

During a typical cycle we collect three such spectra. At  $T_1 = 8$  seconds, the potential on the exit electrode is lowered to 10 kV. This ejects a fixed fraction of the captured antiprotons and provides a calibrated measure for the number of particles captured. At a variable time  $T_2$ , the potential on the high voltage electrodes is lowered to zero, allowing all antiprotons which have not been cooled to the inner, harmonic well to escape. This is typically between 35 and 50 % of the remaining population. Finally, at  $T_3$ , the harmonic well is lowered and the number and energy distribution of cold antiprotons in the central well is recorded.

In Figure 2 we show the total number of antiprotons detected in the inner, harmonic well (normalized to the number of antiprotons initially captured) vs. the cooling time. We find that after approximately 600 seconds as much as 65 % of the initially captured antiprotons were cooled into the inner well. The solid line shows the prediction for a cooling time constant of 175 sec. This time constant is in good agreement with calculations based on Spitzer's equation [8], allowing for the only partial overlap between electron and antiproton clouds.

Overall we have collected data for about 30 LEAR shots during the 2 hour beam time for which the parameters given here apply. All these runs show the same features. Subsequently we have increased the electron density, thereby lowered the cooling

time constant to about 50 seconds, and reproduced the overall results. Since both the parameters for the LEAR beam and the settings for the trap parameters have changed drastically these data can not be easily compared, but we now use the change of annihilation rate in time as an indication for successful electron cooling, which is then used as a start signal for the continuation of the measurement cycle.

The following describes the finding for one specific shot during this 2 hour LEAR run. Figure 3 shows the energy spectrum of those antiprotons released from the inner, harmonic trap after 1500 sec of storage time. We find the width of the peak to be less than 800 meV, with the centroid located around 1 eV. Due to unknown contact potentials on the trap structure it is impossible to determine the absolute value of the energy to better than 200 meV. The width of the distribution must be attributed mostly to the space charge effects from the charged particles in the trap. When the antiprotons are cooled to 10 K the Debye length is smaller than the cloud size and the cloud can be considered a uniformly charged ellipsoid. When the potential at the edge of the cloud balances the external potential the antiprotons will start escaping the trap. Since the shape of the potential and the cloud is changing when the external potential is reduced, this is a dynamic process. Using the parameters for our trap, and assuming the cloud to be an ellipsoid despite the unsymmetrical lowering of the potential, we find this balance to occur at  $V \approx 0.95$  Volts. This argument does not include the space charge potential from the electrons. We find little effect on the overall width of the spectrum when the electrons are removed prior to opening the trap and attribute this to the small overlap in radial direction between electrons (which are produced as a filament with a sub-millimeter diameter) and the antiprotons (which occupy a region of several mm diameter). Therefore we find our results to be fully compatible with 65 % of the antiprotons having been cooled to the ambient temperature of the trap ( $< 15$  K) after 600 seconds.

During the entire time between the initial capture of the antiproton pulse and the

final release from the inner trap, the counts in the external scintillators are recorded. Scintillators S1 - S3 are located closest to the center of the trap and are therefore mostly sensitive to annihilations occurring on the residual gas in the trap (see Figure 1). For background suppression these scintillators are connected in a two-fold coincidence set-up and the detection efficiency is determined to be 4 %. Since the number of stored antiprotons may vary in time, the observed annihilation rate needs to be normalized to the number of particles present in the trap at any given time  $t$ . To obtain this number, we use four data points between which we interpolate assuming an exponential decay of the antiproton population (which has been confirmed in independent measurements studying the development of the antiproton population both with and without electron cooling present). The number of antiprotons at  $t = 0$  is obtained from the signal at T1. The number of cold antiprotons remaining at the end of the cycle ( $t = 1500\text{sec}$ ) is obtained by integrating the spectrum at T3. The number of antiprotons in the trap just after the opening of the catching trap (T2) is obtained by adding the integrated count rate (after background subtraction) from S1 - S4 and S5 - S8 during the storage time in the inner well to the number at T3. Adding to this the count rate observed at T2 gives the number of particles prior to the release from the catching trap. These results can be cross checked using typical decay times of particles in the trap as well as the known ratio between cold and hot particles at the specific time T2. Such a normalized annihilation rate, for this specific run, is shown in Figure 4.

At the beginning of the cool-down we see an increase in the probability for annihilation on the residual gas. The annihilation rate reaches a maximum at approximately 150 seconds, but afterwards decreases strikingly. At  $t = 600$  seconds the long, non-harmonic section of the trap is opened and a small, but sharp, drop in the annihilation rate is seen. This indicates the ejection of the few higher-energy antiprotons remaining in this section of the trap. Subsequently, the observed rate is not distinguishable

above the cosmic-ray background. This is so even though, in this specific example, approximately 12 % of the initially captured antiprotons were determined to be still present in the inner trap at  $t = 1500$  sec.

This observation is in contradiction to the generally held belief that the annihilation cross section at low energy should exhibit a  $1/v$  dependence [9]. (This adiabatic calculation was done, it should be noted, for hydrogen targets.) Such a  $1/v$  behavior would result in a normalized annihilation rate which would be independent of the antiproton energy, which in turn implies that we should observe a constant rate vs. time. Thus, with a  $1/v$  behaviour, neither the initial rise of the observed rate nor the decay at times larger than 200 seconds could be explained. (The initial increase may be consistent with a  $1/v^n$ ,  $n > 1$ , dependence as given, for instance, by Morgan and Hughes [10], who had  $n = 2$ .) The upper bound of the observed annihilation rate is  $8 \times 10^{-3} \text{ sec}^{-1}$ . However, the final annihilation rate at  $t \geq 600$  sec is significantly lower than this. To our knowledge no theoretical model exists that predicts such a striking (or indeed, any) decrease of the rate with temperature. An approach [11] different than that of Ref. [9] uses a coupled-channel, non-adiabatic procedure. Although this produces a low rate at low energies, that model underpredicts our measured results at times less than 200 sec.

The chemical composition of the residual gas in the trap is of critical importance. Since the outer wall of the vacuum vessel is in direct contact with the liquid helium in the cryostat, all gases except hydrogen and helium should be frozen out. Furthermore, because of the liquid helium environment and the fact that helium is poorly pumped by the external ion-getter pumps, the remaining gas should be predominantly helium.

Now we can consider the actual gas pressure in the trap. In fact, the observed maximum annihilation rate,  $8 \times 10^{-3} \text{ sec}^{-1}$ , can be used to verify a rough estimate for the residual gas pressure. Assume that (1) the cross-section estimates given by Bracci et al. [9] (which has a  $1/v$  dependence) are valid as an upper bound for our

observed annihilation rate even through the calculation was for a hydrogen target. and (2) the measured temperature of the trap structure. 10 K. is the temperature of the residual gas. Using these parameters one obtains  $4 \times 10^{-12}$  Torr for the residual gas pressure. This is in good agreement with our expectation that the gas pressure in the trap is bounded from above by the lower limit of the residual gas pressure immediately outside the cryogenic section.  $10^{-11}$  Torr.

In those runs where no electrons were preloaded, so no cooling of the antiprotons was taking place, the observed normalized annihilation rate remained constant at about  $2 \times 10^{-3}$  over comparable time intervals. This shows the importance of the temperature of the antiprotons and proves the stability of the antiproton cloud against dynamical effects.

Experimental data for the annihilation of antiprotons on neutral particles at low energy does not exist. We are investigating the possibility that there exists a small repulsive potential at short range [12]. Strong binding/antibinding effects on antiprotons penetrating the electron cloud of helium atoms have been observed by the PS194 collaboration [13] in a study of the double-ionization cross section for antiprotons and protons impacting on a helium gas target at energies of 13 keV and above. Recently, the formation of metastable systems in antiproton-helium collisions have been observed [14] and theoretical predictions of repulsive potentials in excited-state systems have been discussed [15]. Possibly related effects have been seen in positronium formation from positron impact on large molecules [16]. (Elsewhere we will comment in more detail on these points [17].)

The observed reduction of the annihilation rate at ultra-low energies would have a significant impact on a number of experiments planned with cold antiprotons. For these experiments antiprotons, once captured and cooled in the PS200 catching trap, need to be extracted as a beam and transported to either a scattering chamber or a second trap system for recapture. Such a transport line would be made technically

much easier if a room temperature vacuum system can be used instead of enclosing the entire apparatus in a cryogenic environment.

Downstream traps will have to include a vacuum section which can be coupled to the PS 200 catching trap (or a similar system) for filling. Again, this is easier to do if ultra-low pressures are not needed, and, even though the actual traps need to be at cryogenic temperatures to achieve the ultra-low energy for the antiprotons, the transfer sections (which must include mechanical valves) could be operated under room temperature UHV conditions. To summarize, because of the reduced antiproton annihilation rate at low energies that we have observed, the long storage times needed for experimentation with antiprotons can realistically be achieved in small systems [18]. (Earlier it was assumed that antiprotons need to be stored at higher energies, requiring larger, possibly ring-like structures, to counteract the expected increase of the annihilation rate at low energies.)

Future work will include the controlled reheating of the cooled antiprotons. This will be done by using resonance excitation of the axial motion with radio-frequency fields. The energy dependence of the annihilation cross section will be studied. We also will use different target gases to investigate the possible effect of the polarization potential of the target atom.

The work described here has been performed within the framework of the PS200 experimental development and we wish to thank the entire PS200 collaboration for their support. We especially wish to thank P. L. Dyer for the development of the data acquisition system used for these measurements, J. Rochet for his assistance in constructing and operating the experimental apparatus, and M. Charlton and Y. Yamazaki for their support during data taking. We appreciate the helpful comments by S. Barlow on the positron annihilation data. None of the results presented here would have been obtainable without the support and help from the entire LEAR operating team. A very special 'thank you' goes to J.-Y. Hemery, M. Michel, and M.

Giovannozzi for delivering the very best beam spot possible to the entrance of our apparatus. This work was in part supported by the US Department of Energy under contract no. W7405 ENG-36 (Los Alamos), the U.S. Air Force Office of Scientific Research under grant no. F49620-94-1-0223 (Pennsylvania State University) and the Alexander von Humboldt Stiftung (M.M.N. at Ulm).

## References

- [1] M. H. Holzschneider. *Hyperfine Int.* 81 (1993) 71; M. M. Nieto and M. H. Holzschneider. *Appl. Phys. B* 60 (1995) 103; M. H. Holzschneider. et al.. *Phys. Atom. Nucl.* 57 (1994) 1799; M. H. Holzschneider. *Physica Scripta* (to be published).
- [2] T. Goldman and M. M. Nieto, *Phys. Lett. B* 112 (1982) 437.
- [3] F. S. Witteborn and W. M. Fairbank. *Phys. Rev. Lett.* 19 (1967) 1049.
- [4] G. Gabrielse, X. Fei, K. Helmerson, S. L. Rolston, R. Tjoelker, T. A. Trainor, H. Kalinowsky, J. Haas, W. Kells: *Phys. Rev. Lett.* 57 (1986) 2504, and G. Gabrielse, X. Fei, L. A. Orozco, R. L. Tjoelker, J. Haas, H. Kalinowsky, T. A. Trainor, and W. Kells, *Phys. Rev. Lett.* 65 (1990) 1317.
- [5] J. R. Pierce. *Theory and Design of Electron Beams* (D. van Nostrand, NY, 1949). chapter 3; H. G. Dehmelt, *Adv. At. Mol. Phys.* 3 (1967) 53; *ibid.* 5 (1969) 109.
- [6] G. Gabrielse, L. Haarsma, and S. L. Rolston, *Int. J. Mass Spec. Ion Processes* 88 (1989) 319.
- [7] Solid state switch Model HTS301 from Behlke Electronics GmbH, Frankfurt, Germany, with maximum operating voltage of 30 keV and a rated rise time of 20 ns under optimum load conditions.
- [8] L. Spitzer: *Physics of Fully Ionized Gases*. Interscience Publishers. New York (1962) chapter 5.
- [9] L. Bracci, G. Fiorentini, and O. Pitzurra, *Phys. Lett. B* 85 (1979) 280.
- [10] D. L. Morgan, Jr. and V. W. Hughes. *Phys. Rev. A* 7 (1973) 1811.



- [11] A. Yu. Voronin, Zh. Eksp. Teor. Fiz. 102 (1992) 760. [Sov. Phys. JETP 75 (1992) 416.]
- [12] We wish to especially thank T. Kinoshita and T. Ziegler, private communications, for insightful comments on this matter.
- [13] P. Hvelplund, H. Knudsen, U. Mikkelsen, E. Morenzoni, S. P. Møller, E. Uggerhøj, and T. Worm, J. Phys. B 27 (1994) 925.
- [14] T. Yamazaki, R. S. Hayano, T. Ishikawa, H. Onta, E. Takada, H. Tamura, and A. Sakaguchi, Phys. Rev. Lett. 63 (1989) 1590.
- [15] K. Richter, J.-M. Rost, R. Thurwächter, J. S. Briggs, D. Wintgen, and E. A. Solov'ev, Phys. Rev. Lett. 66 (1991) 149.
- [16] C. M. Surko, R. G. Greaves, and M. Leventhal, Hyperfine Int. 81 (1993) 239.
- [17] M. H. Holzschneider et al., (in preparation).
- [18] H. G. Dehmelt, R. Van Dyck, P. Schwinberg and G. Gabrielse, Bull. Am. Phys. Soc. 24 (1979) 757, abstract D 3; S. D. Howe, M. V. Hynes, and A. Picklesimer; in *Antiproton Science and Technology*, eds. B. W. Augenstein, B. E. Bonner, F. E. Mills, and M. N. Nieto (World Scientific Singapore, 1988), p. 481; G. A. Smith, Hyperfine Int. 81 (1993) 189.

Figure Captions:

**Fig.1** Schematic layout of the experimental set-up. Shown is the superconducting magnet system (length 2 meter), the PS200 catching trap, all beam monitors, and the scintillators used to trigger the voltage switch and to monitor the antiproton annihilations during storage and upon release.

**Fig.2** Accumulation of ultra-low energy antiprotons in the harmonic well in the center of the PS200 catching trap. The solid line is calculated for a cooling time constant of 175 seconds and a maximum transfer efficiency of 65 %.

**Fig.3** Energy spectrum of cold antiprotons released from the inner trap. The centroid of the distribution is at  $\leq 1$  eV, the FWHM is  $\leq 800$  meV.

**Fig.4** Rate of annihilation during storage and cooling of antiprotons in the PS200 catching trap. The observed rate has been normalized to the number of antiprotons in the trap at any given time  $t$ . The sharp drop between 600 and 700 seconds is due to the loss of antiprotons when the outer trap is opened completely (see text also).

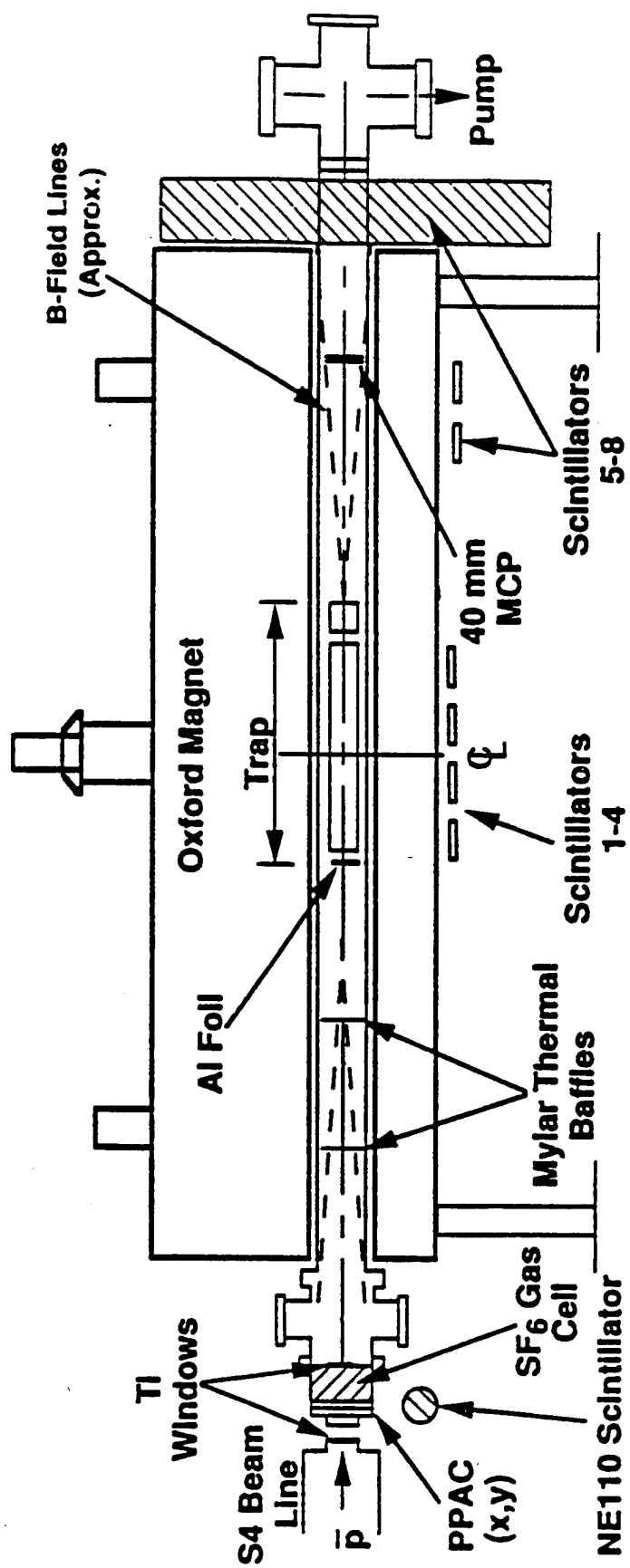


Figure 1

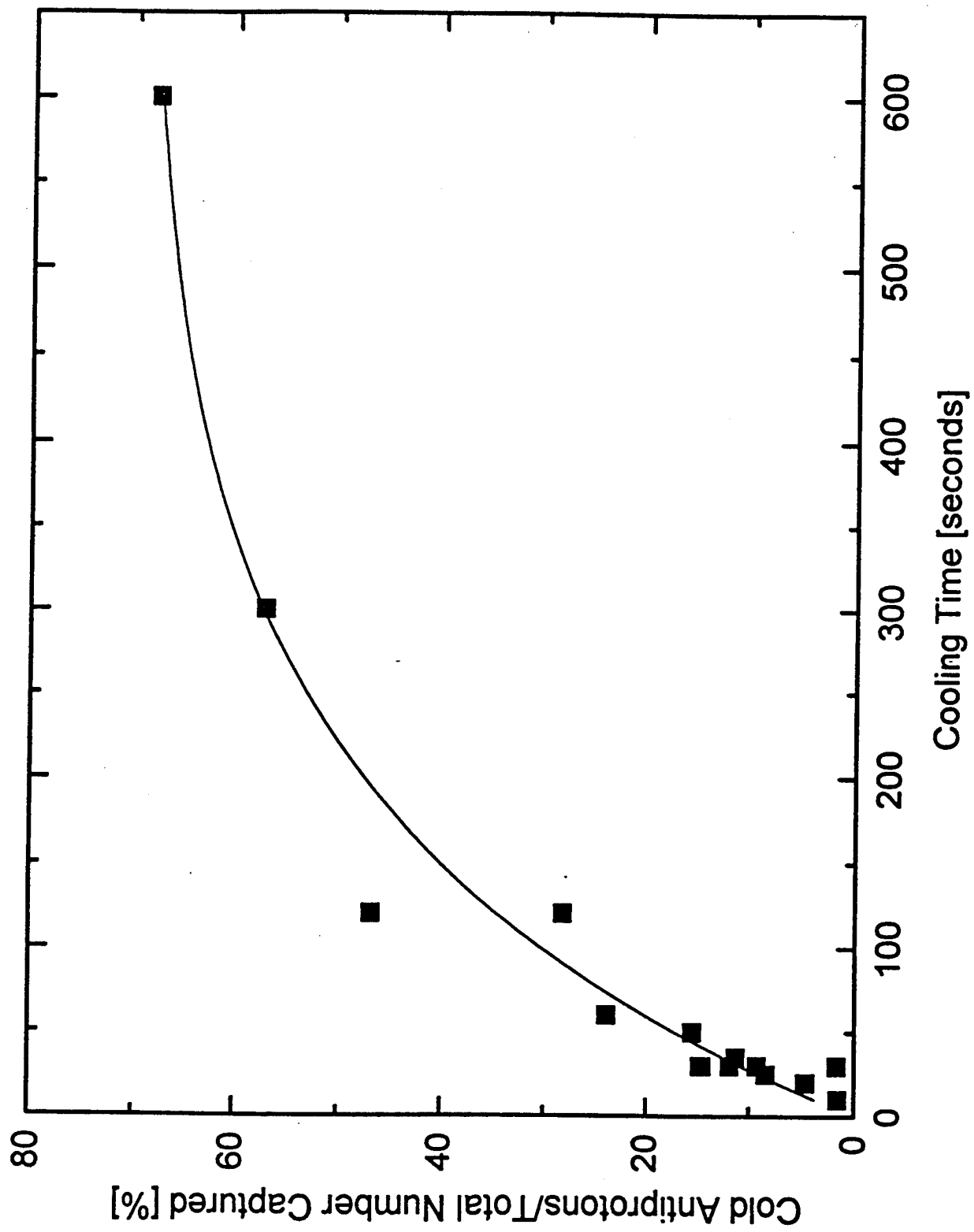
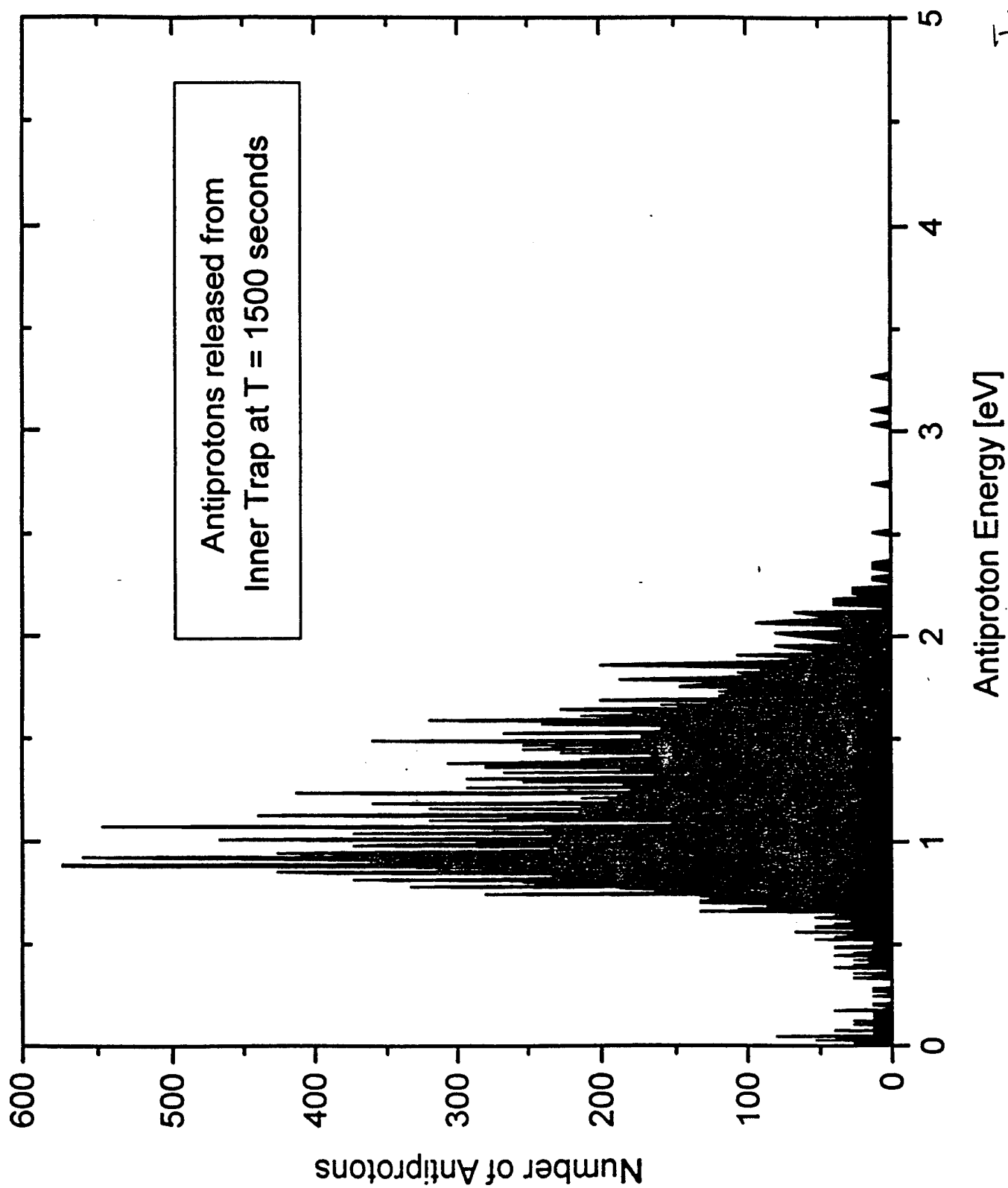


Figure 2

Figure 3



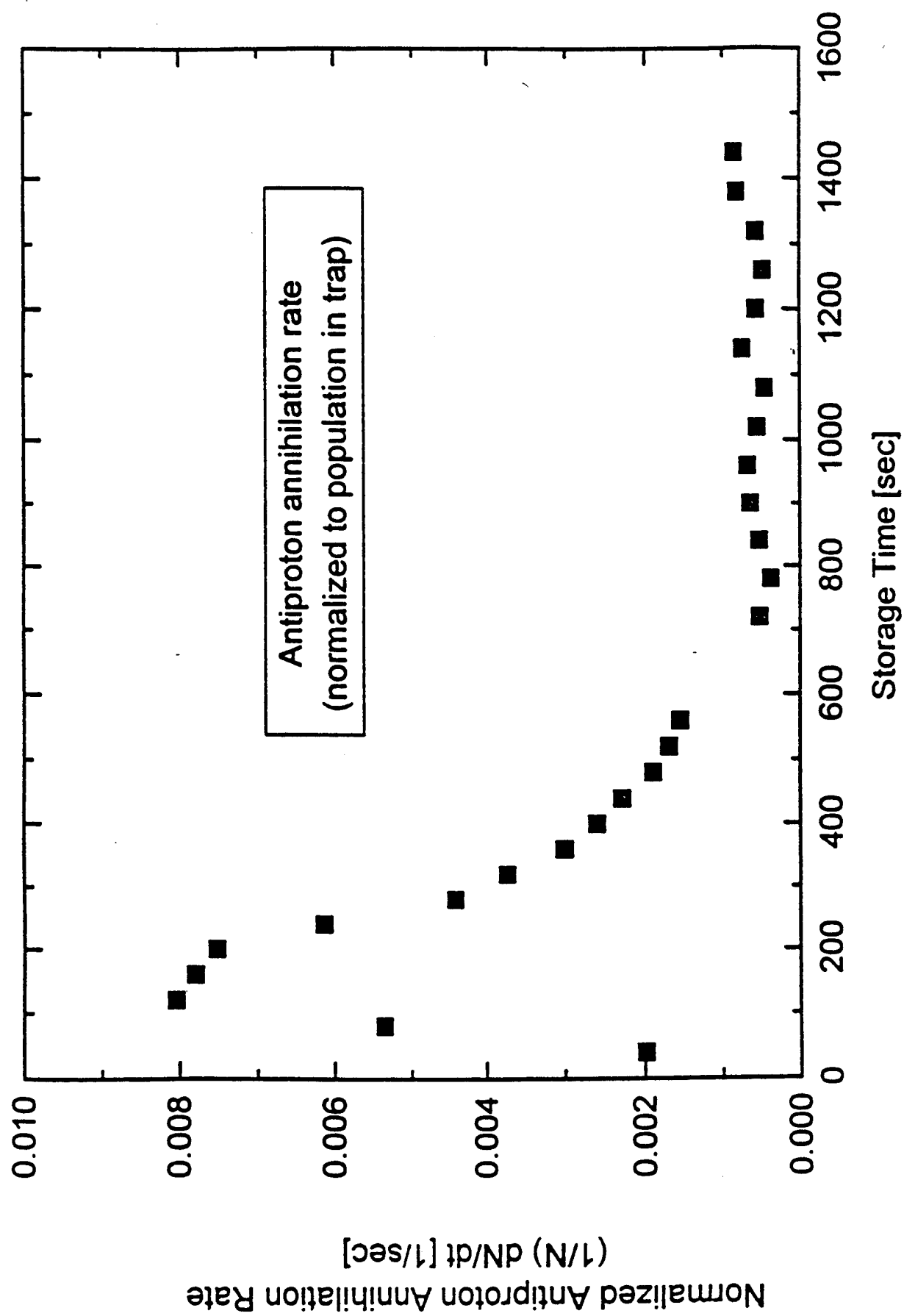
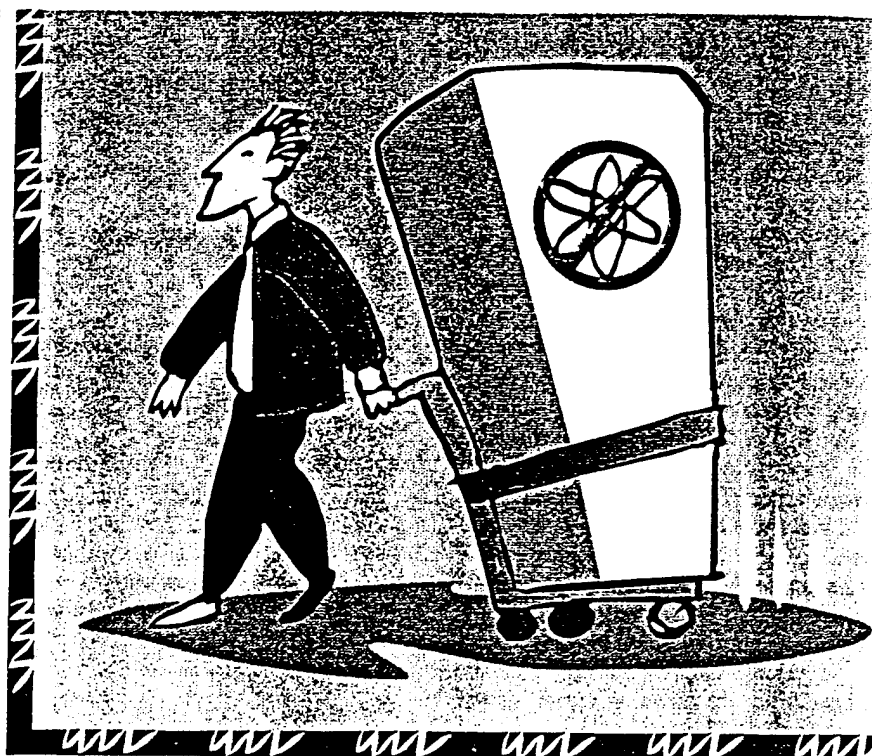


Figure 4

southern Arabian Peninsula, Elachi saw a series of lines leading to a single point. "Archeologists went to this area in Oman and found that these lines are really ancient roads, says El-Baz. "The point where they meet is the site of an ancient city," which may be the lost city of Ubar, famous in the Koran and other literature as a major stop on the frankincense trade route. Further investigations using SIR images and satellite photos led to the discovery of another, even larger ancient entrepôt, Saffara Metropolis, in Oman's Qara Mountains.

Elachi's latest brainchild, a technologically advanced SIR, flew in April on the shuttle *Endeavor* and is scheduled to fly again in August. Part of the \$366 million, 23,000-pound Space Radar Laboratory, the new SIR is regarded as the most sophisticated radar system ever used in space. Unlike its single-wavelength predecessors, which sent C-band (6-centimeter) signals, the new model also uses X-band (3-centimeter) and L-band (23-centimeter) wavelengths. Each wavelength penetrates surface materials differently. L-band radar penetrates solid ground better than shorter wavelength signals do, and X-band signals reflect better off of low-density materials. Combining data from the three frequencies produces sharper images than were previously possible.

The radar images from the April shuttle flight will be used to study the geology and hydrology of nearly 20 sites in South America, Australia, Egypt, the Sahara Desert, and Death Valley, Calif. El-Baz has requested radar strips of two areas—the Arabian Peninsula, where he has been working since 1991 to evaluate the Gulf War's environmental effects; and Egypt's Western Desert, where he hopes to further trace the rivers uncovered by the first SIR flight. He has also found evidence that other portions of the Sahara may conceal huge underground aquifers. He believes they may be on the scale of the one Libya is now tapping, which hydrologists claim will supply that riverless country with six million cubic meters of water daily for the next half-century.—PETER TYSON



## Have Antimatter, Will Travel

Antimatter may be most familiar as the strange fuel that powers *Star Trek's* starship Enterprise across the galaxy in the twenty-fourth century. But the material is quite real. In fact, twentieth-century physicists are heralding it as a potential tool for accomplishing feats ranging from understanding the fundamental nature of matter to creating a powerful new form of energy.

Unfortunately, antimatter is also quite rare and volatile, which has severely limited scientists' ability to use the exotic material. For the past 40 years, physicists have been able to study particles of it as it zips around the massive linear accelerators where it is created by high-energy particle collisions. And because antimatter possesses an electrical charge opposite that of normal matter, a proton with a positive charge and an antiproton with a negative charge will annihilate each other on contact, converting all of

their combined mass into a flash of energy.

In recent months, however, researchers have developed a technique that collects more than a million antimatter particles at a time—an order-of-magnitude increase over earlier efforts. Encouraged by the ability to amass such quantities, they are designing cases for transporting the particles from the giant accelerators to their own labs for experimentation.

The technique represents a major step beyond the original technique for collecting antimatter particles developed by Gerald Gabrielse, a physicist at Harvard University. While working at the European Organization for Nuclear Research (CERN) in France a few years ago, he devised a way to siphon off as many as 100,000 antiprotons into a foot-long cylindrical trap. The billions of antiprotons created in the particle accelerator were first slowed from near light-speed by radio waves, which absorbed some of the antimatter's kinetic energy. This material was then guided by a magnetic

field into a separate tunnel at CERN, called the Low-Energy Antiproton Ring. Gabrielse took the small fraction of whizzing antimatter particles that would escape through an opening in the ring and confined them with a strong magnetic field in a vacuum tube.

In recent months, a team from Los Alamos National Laboratory led by physicist Michael Holzsheiter improved Gabrielse's technique by building a magnetic trap large enough to hold a million antiprotons. The team also fired electrons into the trap to slow the still whizzing particles, making them easier to use in experiments. Because the electrons also have a negative electrical charge, they absorb and dissipate the antiprotons' high energy without colliding with and annihilating them.

Using this concept, scientists at Los Alamos and Pennsylvania State University are planning to build portable antimatter carrying cases. An entire apparatus—which would require powerful batteries to generate the required magnetic fields—might be the size of a 40-gallon trash can and weigh 400 pounds. Though cumbersome, the cases would allow researchers to transport antimatter from CERN anywhere in the world, says Gerald Smith, a physicist at Penn State.

In one of the first experiments with such relatively large quantities of antimatter, theorists want to probe the accuracy of Einstein's theory of gravity. Michael Nieto, a theoretical physicist at Los Alamos, plans to open the end of a capture tube and drop antiprotons into another vacuum tube to measure whether gravity affects their movement any differently than it does normal protons under identical conditions.

If antiprotons fall at a different rate than protons, it would mean gravity is more complicated than even Einstein thought, perhaps involving an unknown force. Such a result could explain why theorists have had great difficulty uniting the theories of gravity, electromagnetic forces, and strong and weak nuclear forces to form a grand theory describ-

ing all the interactions of matter and energy in the universe.

Some researchers also think portable antimatter has a future in cancer therapy. Antiprotons aimed at tumors could be more effective at killing cells than standard radiation, says Theodore Kaloogeropoulos, a physicist at Syracuse University. That's because antiproton beams, which completely annihilate the non-antimatter tissue on contact, are more destructive than the proton beams used in conventional therapy. He is planning an experiment at Brookhaven National Laboratory to shoot antiproton beams into a number of materials of varying density to test their precision and effectiveness.

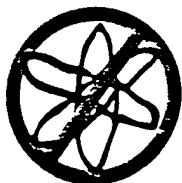
In industry, antimatter might supplement x-rays as a more sensitive test for detecting flaws or impurities in fabricated materials, such as panels for airplanes or a space station, says Terrence Goldman, a physicist at Los Alamos. Because the radiation emitted from antimatter annihilation

scatters much less as it leaves a material than x-rays do, antimatter scans may yield higher-resolution images revealing tinier flaws.

Stanley Bodsky, a physicist at Stanford University, and Penn State's Smith are part of a collaboration that has begun investigating the possibility of building entire antimatter atoms starting with the simplest, antihydrogen. Working at Fermi National Laboratory, they plan to mix individual antiprotons with anti-electrons, or positrons, to form antihydrogen atoms.

Creating such antiatoms would be a key step toward what ultimately may be antimatter's most dramatic application: energy production. Remarkably, only a few cubic centimeters of antimatter, perhaps as a block of antihydrogen ice, would be required to propel a space ship, theorists believe. The ice could be bled to annihilate normal hydrogen atoms, generating billions of times the energy produced by burning the most efficient hydrocarbon-based fuels.

—DAVID GRAHAM



## Whatever your problem, I'll solve it.

I'm Riva Poor and your success is my business.

I've helped thousands of successful people achieve the Results they want in life. And I can help you.



I'm a professional problem-solver who can help you solve your problems. I can help you identify THE REAL YOU, WHAT YOU REALLY WANT and HOW TO GET IT. I can provide you with *new ways* of looking at yourself, your business, your personal relationships or whatever is important to you. I can rid you of any negative attitudes keeping you from attaining your goals. I can *catalyze* your best thinking.

You will get clarity, reassurance, direction, self-confidence. Results! More money, power, achievement, productivity, leisure time, better family relations, whatever is important to you.

My clients are the proof. And they'll be pleased to talk with you.

Challenge me now. Call me to explore what I can do for you. *No charge to explore and no obligation.*

Your success is my business. Why Wait? Call me. Right now.

MIT. SM in Management

"The Dr. Spock of the business world" — *National Observer*. "Mother of the 4-day week" — *Newsweek*. Originator of Dial-A-Decision® to give you immediate Results regardless of distance.

Call  now.

**617-868-4447**

Riva Poor, Management Consultant  
73 Kirkland St., Cambridge, MA 02138  
617-868-4447 Dept. TR-3

©1980 Riva Poor.



# A churnful of antiprotons, please

Justin Warner, Washington DC

IN THE *Star Trek* television series, antimatter propels the starship Enterprise to boldly go where no one has gone before. In the real world too, antimatter is a potential source of staggering quantities of energy. But not much effort has gone into exploring its applications for the good reason that, so far, it can only be studied in massive linear accelerators.

Soon, however, scientists may be able to get antimatter delivered to their doorsteps in huge containers resembling milk churns, thanks to the efforts of researchers at Pennsylvania State University and Los Alamos National Laboratory. They have designed a portable antimatter trap the size of a dustbin, which they think could confine the particles magnetically for up to four days before they react with the matter in the trap and disappear.

Antimatter is made of particles that are structurally identical to normal subatomic particles but have opposite fundamental properties. When an antiparticle such as a positron collides with its corresponding matter particle (in this case an electron) they annihilate each other, converting their mass into energy. Because antimatter annihilates so readily, it only exists on Earth when it is artificially generated in high-energy particle accelerators, such as those at CERN in Geneva or Chicago's Fermilab, which cost about \$1 billion to build. So physicists who want to use antiparticles for their experiments have to buy time at these laboratories.

The traps could change all this. According to Gerald Smith, a physicist at Penn State, they could bring antimatter to universities and other research centres that cannot afford to send staff to Fermilab or CERN. They could then use the traps to investigate fundamental theories of physics. Antimatter could even be used by hospitals to treat cancers.

Smith likens his trap to a "big Thermos bottle" about 100 centimetres tall and 50 centimetres in diameter. It weighs 55 kilograms and holds about 10 billion antiprotons. With a handle on top, it could be lugged around like a heavy suitcase.

To prevent the antimatter from coming into contact with air molecules, the trap will be pumped out to leave a very high vacuum in which there are just 100 air molecules per cubic centimetre. Liquid helium insulation in the walls of the trap will maintain an interior temperature only a few degrees above absolute zero. This causes the few remaining air molecules to cling to

the walls, just as a few drops of water will cling to the sides of a test tube. A combination of magnetic fields generated by permanent magnets and electric fields generated by a 10-volt battery will keep antiparticles away from the walls, confining them in a circular orbit within the container.

Smith's team intends to siphon the antimatter from a large "catcher trap" built by Los Alamos physicist Michael Holzshelter and his colleagues. The catcher trap can withstand the energy needed to capture antiprotons directly from the antiparticle

Smith claims that there will not be enough helium in a trap to pose a problem; and that even if the trap failed completely, the 10 billion antiprotons would only produce a dose of radiation comparable to that received from naturally occurring phenomena such as cosmic rays. Smith believes that he will be able to build the traps for less than \$100 000 each, a sum within the reach of major universities' budgets.

Terrence Goldman, a theoretical physicist at Los Alamos, is optimistic about the project, and keen to try one out. "I don't see any problem with portable traps," he says. "I've always been an advocate of them as a way to move higher-energy nuclear research and low-energy particle physics research to universities."

Physicists are keen to find out whether gravity affects antimatter and matter in different ways. If so, it would suggest that gravity is more complex than had previously been suspected, which might explain why grand unification theories have proved to be so unwieldy.

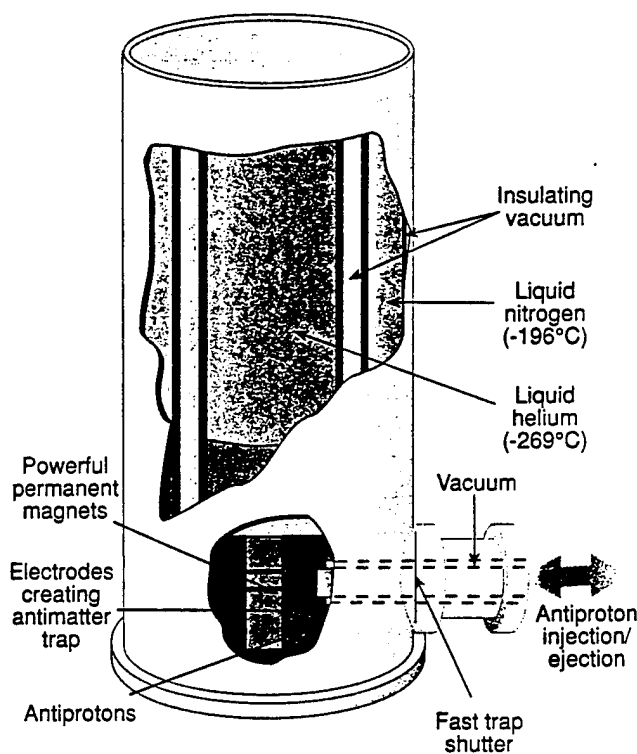
Goldman says that antimatter may also be useful for detecting impurities in manufactured materials such as fan blades for turbines and other aircraft parts. Antimatter produces more focused, specific radiation patterns than X-rays, which reveal more about a substance's chemical properties. Antimatter could also image the human body without delivering as much radiation as conventional X-rays and CAT scans.

Smith would like to bombard water with antiprotons to generate oxygen-15, a radioisotope used in PET scanning that is currently only available in multimillion-dollar reactors. With a portable trap, such

short-lived radioisotopes could be generated cheaply at a patient's bedside, he says.

Theodore Kalogeropoulos, a physicist at Syracuse University in New York state, has proposed using antiproton beams to destroy cancer cells. The antiparticles would deliver concentrated radiation where it was needed, while surrounding tissues would receive only half as much radiation as they would from treatment with other charged particle beams.

The ultimate goal is to create entire antiatoms, made up of antiprotons, antineutrons and positrons. By injecting positrons into a trap full of antiprotons, it might be possible to generate antimatter counterparts of simple atoms such as antihydrogen. If solidified, "antihydrogen ice" could provide an unprecedented source of concentrated energy—perhaps powerful enough to propel a starship Enterprise of the future. □



beam at CERN, but is far too bulky and power-hungry to transport. But by cooling the antiprotons from 20 000 electronvolts to just 10 electronvolts per antiproton, the catcher can prepare them for transport in the simpler, portable trap.

As Smith and his colleagues begin procuring the parts for the traps they face a number of challenges. For example, they hope to make the transfer of antiprotons into the catcher trap ten times as efficient as the present system, which uses thin foils to slow down the antiparticle beam. Instead they plan to use electrostatic forces to prevent the antiprotons scattering as the beam approaches the catcher trap.

Smith mentions two areas where safety could be a problem. One concerns cryogenic liquids such as helium, which can cause asphyxiation if they boil off. The other is the radiation produced as antiprotons escape and annihilate. However,

## Tank circuit model applied to particles in a Penning trap

X. Feng

*Institute of Physics and Astronomy, Aarhus University, DK-8000 Aarhus, Denmark*

M. Charlton

*Department of Physics and Astronomy, University College London, London WC1E 6BT, United Kingdom*

M. Holzscheiter

*Los Alamos National Laboratory, Los Alamos, New Mexico 87545*

R. A. Lewis

*Pennsylvania State University, State College, Pennsylvania 16802*

Y. Yamazaki

*University of Tokyo, Tokyo 153, Japan*

(Received 18 July 1995; accepted for publication 12 September 1995)

The equivalent circuit model is used to describe analytically the coupling process of the center of mass motion of a cloud of particles in a Penning trap. From the response of this coupled circuit to white noise a way of nondestructively diagnosing the number of trapped particles is given which is valid for all values of this quantity. Experimental results are presented and compared with this analysis. © 1996 American Institute of Physics. [S0021-8979(96)01701-0]

### I. INTRODUCTION

Ion traps provide a very clean, virtually background free environment, long sampling times and ultra-low particle energy. Benefiting from these advantages many unprecedented experiments with very high precision have been performed in the fields of laser and microwave spectroscopy, mass measurements and atomic and molecular collisions. In recent years this technique has also been applied to the trapping and manipulation of antimatter. A few antiprotons have been stored in a Penning trap for longer than three months<sup>1</sup> and the proton and antiproton mass ratio has recently been measured with ppb precision.<sup>2</sup> Another experiment, aimed at storing many antiprotons in a Penning trap, has successfully caught about one million antiprotons from a single fast-extracted pulse from the low energy antiproton ring at CERN.<sup>3</sup> The use of trapped antiprotons as an ultra-low energy antiproton reservoir is of interest to various groups for research in atomic, nuclear and fundamental physics, such as comparing gravitation between matter and antimatter and producing antihydrogen. For these purposes a primary question is to diagnose the number of trapped particles continuously and nondestructively.

Wineland and Dehmelt<sup>4</sup> have studied a practical way to determine the number of trapped charged particles by measuring the separation of two resonant peaks when an external "tank" circuit is coupled to their center-of-mass (CM) motion. Thereafter this method has been used widely mostly to determine "small" numbers of trapped particles. In this paper we report on the use of this method to estimate the number of electrons which are present in our cylindrical Penning trap to cool the antiprotons, and its comparison to the number measured by ejecting them onto a foil using appropriate bias voltages. It was thus found that the measured values differed from those derived from Ref. 4 when the number of particles becomes large. We studied this problem by deducing an analytical solution for the equivalent circuit model de-

scribing the coupling of the trap and the electron cloud and found that the equivalent resistance, which expresses the damping of the CM motion of a cloud of particles, plays an important role in this relationship.

In Sec. II we construct the equivalent circuit model in a fully analytical way, and in Sec. III we analyze its impedance which is used to deduce the spectral response to white noise and to find the dependence of this spectrum on the number of trapped electrons. In Sec. IV, we present our experimental results and discuss them within the framework of our analysis.

### II. EQUIVALENT CIRCUIT

Particles are stored in a cylindrical Penning trap with a laboratory inductor connected to the two correction electrodes as shown in Fig. 1. The potentials on the different electrodes were chosen according to the condition given in Ref. 5 to tune out the higher order anharmonic terms in the trapping field. Near the center of the trap the potential can be expressed, for a particle of charge  $q$  and mass  $m$ , as

$$\Phi(r, z) = \frac{m\omega_z^2}{4q}(2z^2 - r^2), \quad (2.1)$$

where  $r$  and  $z$  are cylindrical coordinates, and  $\omega_z$  is the frequency at which a single trapped particle (or the CM of a cloud of particles) oscillates along the  $z$  axis. When the effects of induced charges in the electrodes can be neglected this frequency is given by

$$\omega_z = \sqrt{\frac{V_0 q C_2}{m d^2}}, \quad (2.2)$$

where  $V_0$  is the trapping potential,  $d$  is the characteristic distance defined as  $d^2 = \frac{1}{2}(z_0^2 + \frac{1}{2}r_0^2)$  (see Figure 1) and  $C_2$  is a dimensionless parameter dependent on the trap geometry and in our case is equal to 0.5449

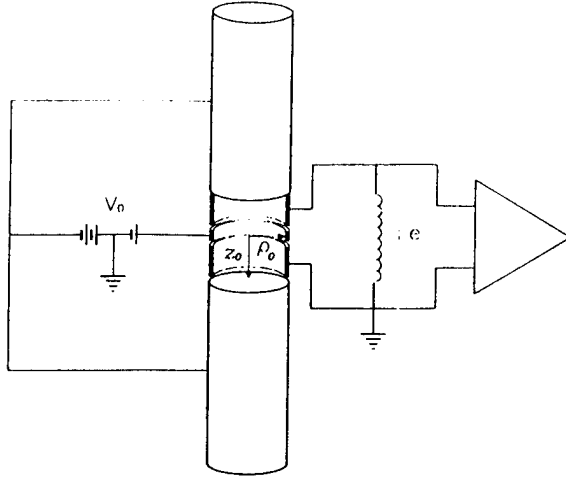


FIG. 1. Open geometry cylindrical trap and typical detection circuit. Here  $\rho_0$  is the inner radius of the trap and  $z_0$  is the dimension from the center of trap to the end of the compensation electrodes. The trapping potential is denoted by  $V_0$  and the inductor  $L_e$  forms part of the tank circuit.

Shockley<sup>6</sup> demonstrated that a charged particle at position  $\mathbf{r}$  which moves with a velocity  $\mathbf{v} = d\mathbf{r}/dt$  in an interelectrode region induces currents in these electrodes. The current flowing from the electrode  $k$  through an external circuit to ground can be expressed as  $i_k = q\mathbf{v} \cdot \mathbf{E}_k(\mathbf{r})$ , where  $\mathbf{E}_k(\mathbf{r})$  is the electric field at position  $\mathbf{r}$  when the electrode  $k$  is at unit potential and the other electrodes are grounded. The current flowing between the two correction electrodes via the external inductor induced by the oscillation of a single trapped particle can then be written as

$$i_c = q\mathbf{v}_{particle} \cdot \mathbf{E}_c(\mathbf{r}), \quad (2.3)$$

where  $\mathbf{v}_{particle}$  is the velocity of the trapped particle and  $\mathbf{E}_c(\mathbf{r})$  is the electric field near the center of trap when one of the correction electrodes is at unit potential and all others are grounded. This can be given in terms of the potentials applied to the trap electrodes with symmetric and antisymmetric configuration under reflection across the  $z=0$  plane as shown in Fig. 2. Solutions of the Laplace equation near the

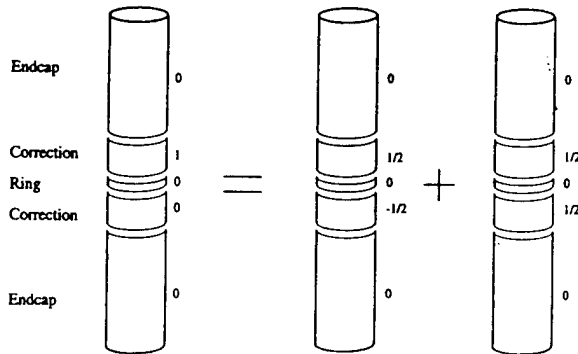


FIG. 2. The sum of the symmetric and antisymmetric configurations of a trap which forms the unit potential at one correction electrode and zero potential at the others. The solutions for the potential near the trap center are given by Eqs. (2.4) and (2.5).

center of the trap can be expanded in Legendre polynomials as<sup>5</sup>

$$\Phi_{sym}(\mathbf{r}) = \frac{1}{4} \sum_{k=even} D_k \left( \frac{r}{d} \right)^k P_k(\cos \theta) \quad (2.4)$$

and

$$\Phi_{anti}(\mathbf{r}) = \frac{1}{2} \sum_{k=odd} d_k \left( \frac{r}{z_0} \right)^k P_k(\cos \theta), \quad (2.5)$$

and  $\mathbf{E}_c(\mathbf{r})$  can be expressed as

$$\mathbf{E}_c(\mathbf{r}) = \nabla[\Phi_{sym}(\mathbf{r}) + \Phi_{anti}(\mathbf{r})] \quad (2.6)$$

which to first order can be approximated by

$$\mathbf{E}_c(\mathbf{r}) = -\frac{d_1}{2z_0} \hat{e}_z. \quad (2.7)$$

According to Eq. (2.3) the oscillation of a single particle in a Penning trap induces a current

$$i_c = -\frac{qd_1\dot{z}}{2z_0} \quad (2.8)$$

in the correction electrode. If there is a potential difference  $V$  across these two correction electrodes the motion of the particle is modified by the electric force induced by this voltage and the induced current is changed. In this case we write the equation of motion of a single particle in the  $z$ -direction in a Penning trap as<sup>4</sup>

$$\ddot{z} = -\omega_z^2 z - \gamma \dot{z} - \frac{qd_1 V}{2mz_0} + \frac{F_{ind}}{m}, \quad (2.9)$$

where  $\omega_z^2$  denotes the harmonic restoring strength given by the trapping field,  $\gamma$  is the cooling rate of the motion of the particle,  $-qd_1 V/2z_0$  is the electric force due to the potential difference between the two correction electrodes, and in the last term  $F_{ind}$  is the Coulomb attraction force due to the image charge in the electrodes induced by the trapped particle. This term is negligibly small in the single particle case. From Eqs. (2.8) and (2.9), and by neglecting the last term in Eq. (2.9), we find the dependence of the voltage  $V$  on the induced current  $i_c$  can be written as

$$V = l_s \frac{di_c}{dt} + \frac{1}{c_s} \int i_c dt + r_s i_c, \quad (2.10)$$

where we define

$$l_s = \frac{4mz_0^2}{q^2 d_1^2}, \quad c_s = \frac{q^2 d_1^2}{4kz_0^2},$$

and

$$r_s = \frac{4\gamma m z_0^2}{q^2 d_1^2}.$$

For the many particle case the motion of the CM of a cloud of particles induces a current

$$I_c = \frac{nq d_1 \dot{Z}}{2z_0}, \quad (2.11)$$

where  $Z$  denotes the coordinates of the CM and  $n$  is the number of particles. We can write the equation of motion of the CM in  $z$  direction in a Penning trap as

$$\ddot{Z} = -\omega_z'^2 Z - \gamma' \dot{Z} - \frac{qd_1 V}{2mz_0}, \quad (2.12)$$

where  $\omega_z'^2$  expresses the harmonic restoring strength given by the trapping field modified by the Coulomb attraction force due to the total image charge.  $\gamma'$  is the damping rate of the CM motion which includes cooling of the CM motion by transferring the energy of the CM to an external reservoir, and the diffusion of the CM motion which transfers the energy of the CM motion into the internal mode. Within the first order approximation the effect of image charges on the axial CM motion of a cloud of trapped particles can be expressed as a shift of the axial oscillation frequency of that motion. From Eqs. (2.11) and (2.12) the analogous relation to Eq. (2.10) in the case of many particles in the cloud is

$$V = l_n \frac{dI_c}{dt} + \frac{1}{c_n} \int I_c dt + r_n I_c \quad (2.13)$$

with

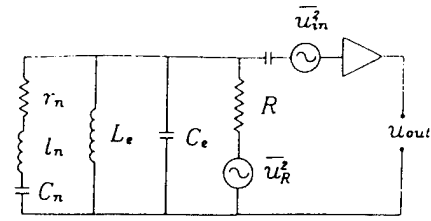
$$l_n = \frac{4mz_0^2}{nq^2 d_1^2}, \quad c_n = \frac{q^2 d_1^2}{4nkz_0^2}$$

and

$$r_n = \frac{4\gamma' m z_0^2}{nq^2 d_1^2}.$$

The voltage-current relations given by Eqs. (2.10) and (2.13) mean that the circuit response of a single particle or a cloud of particles in a Penning trap is equivalent to a  $l_n, c_n, r_n$  circuit with a resonant frequency of the oscillation of a single particle or the CM of a cloud of particles, respectively.

From this relation we can draw the equivalent electrical representation of the external "tank" circuit formed by a laboratory inductor  $L_e$  and the trap parasitic capacitance  $C_e$  coupled to the motion of the CM of a cloud of trapped particles as in Fig. 3(a), where  $R$  presents the resistance of the external "tank" circuit and  $u_R$  denotes the Johnson noise of this resistor. In Fig. 3(b) we present this circuit in an equivalent way to represent the Johnson noise voltage source as a



(a)

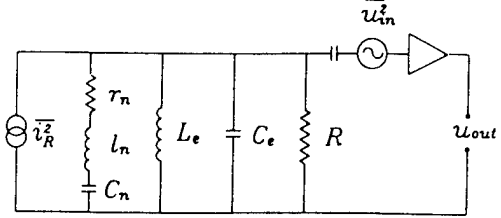


FIG. 3. The equivalent circuit represents an external tank circuit coupled to the motion of the center of mass of a cloud of ions. The Johnson noise is expressed in (a) and (b) as voltage and current sources respectively.

current source. In this equivalent representation we do not include the Johnson noise of the resistor  $r_n$  because it is normally much smaller than  $R$  and the input noise of the preamplifier is ignored since it only increases the amplitude of the white noise background in this case.

### III. CIRCUIT ANALYSIS

The frequency response of the equivalent circuit shown in Fig. 3(b) is described by its impedance

$$Z(\omega) = \frac{1}{\frac{1}{r_n + j\omega l_n + (1/j\omega c_n)} + \frac{1}{R} + \frac{1}{j\omega L_e + j\omega C_e}}. \quad (3.1)$$

Using an amplitude-tracking detector, such as a spectrum analyzer, the measured output spectrum of this circuit for a white noise input source is proportional to the amplitude of its impedance. When  $\omega_z = 1/\sqrt{L_e C_e}$ , the amplitude of the impedance in Eq. (3.1) can be written as

$$|Z(\omega)| = \sqrt{\frac{R^2 l_n^2 \omega^2 (\omega^2 - \omega_z^2)^2 + R^2 r_n^2 \omega^4}{\omega^4 (R + r_n)^2 + 4[l_n^2 + (r_n^2 R^2 / \omega_z^4 L_e^2) - (2l_n R^2 / L_e \omega_z^2)] \omega^2 (\omega^2 - \omega_z^2)^2 + (l_n^2 R^2 / \omega_z^4 L_e^2) (\omega^2 - \omega_z^2)^4}}. \quad (3.2)$$

Eq. (3.2) indicates that the spectrum consists of one dip at  $\omega = \omega_z$ , since the CM motion of the trapped particles oscillates in resonance and shunts the external circuit by its equivalent resistance  $r_n$ , and two peaks. The latter are caused by the resonant peak of the external tank circuit, being shifted by the additional inductance  $\pm 2il_n|\omega - \omega_z|(1 + 1/Q_{particle}^2)$  due to the CM motion of trapped particles.

Here  $Q_{particle}$  expresses the ratio of the energy deposited in the CM motion to that dissipated due to relaxation into the internal mode and coupling to the external reservoir. We recall the definition of  $l_n = l_s/n = (4mz_0^2/nq^2 d_1^2)$ . From this relationship it is clear that the size of the shift of the RCL parallel resonance peak induced by the trapped particles is related to their number.

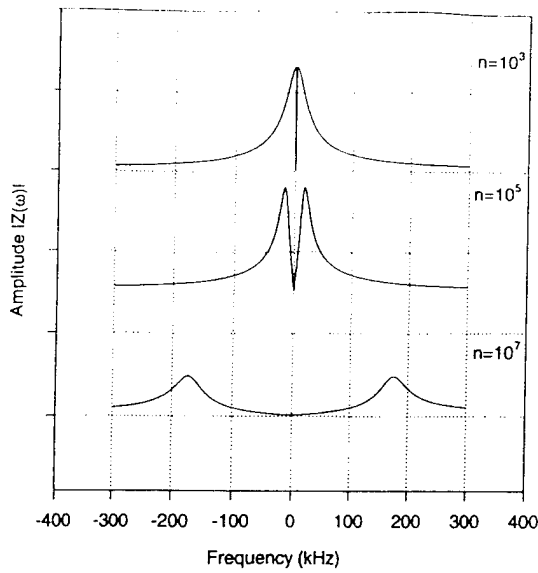


FIG. 4. Calculation of the shifted  $RCL$  resonance peaks due to coupling to the CM motion of different number of trapped electrons. The amplitude denotes  $|Z(\omega)|$  from Eqs. (3.2).

Let us now consider the parameters actually present in our experiment. We stored electrons in an open geometry cylindrical trap with  $z_0=17.9$  mm,  $\rho_0=19.05$  mm and  $d_1=0.8994$ . With  $V_0=30$  V the axial frequency is  $\omega_z=2\pi\times 17.5$  MHz. A normal copper inductor with inductance  $L_e=2.2$   $\mu$ H connects the two correction electrodes. Shunted with the parasitic capacitance  $C_e=37.6$  pF of the trap's electrodes this forms a tank circuit with a  $Q$  value of about  $Q_e=550$ , equivalent to a pure resistance of  $R=133$  k $\Omega$  at the center of the resonance of the tank circuit. Spectra calculated using these parameters are shown in Fig. 4 for different numbers of trapped electrons, from which it is clear that measuring the separation of the two peaks offers a practical way of estimating this number. The relationship of the separation of the two peaks to the number of trapped electrons and the equivalent resistance  $r_n$  is shown in Fig. 5. This indicates that the equivalent resistant  $r_n$  plays an important role with increasing numbers of trapped electrons. From the viewpoint of the equivalent circuit the  $Q_{particle}$  is defined as  $(\omega_e l_s / nr_n)$  which decreases with the increase of the number of trapped particles if  $r_n$  keeps constant. As a result the contribution of the term which proportional to  $1/Q_{particle}^2$  in the inductance  $\pm 2il_n|\omega - \omega_z|(1 + 1/Q_{particle}^2)$  is increased, which is added to the external circuit due to the coupling of the trapped particles. When this term plays an important role in this expression, the increasing of the separation of the two resonant peaks is slowed down and even reversed with the increasing of the number of trapped particles as shown in Fig. 5.

In order to obtain the analytical relationship between the peak separation  $\Delta\omega$  and the number of trapped particles we assume  $|\omega - \omega_z| \ll \omega_z$ . With this approximation we find

$$\left(\frac{\Delta\omega}{\omega_z}\right)^2 = \frac{nL_e}{l_s} \sqrt{1 + \frac{2r_n}{R} + \frac{2r_n^2 n}{\omega_z^2 l_s L_e}} - \frac{r_n^2 n^2}{\omega_z^2 l_s^2} \quad (3.3)$$

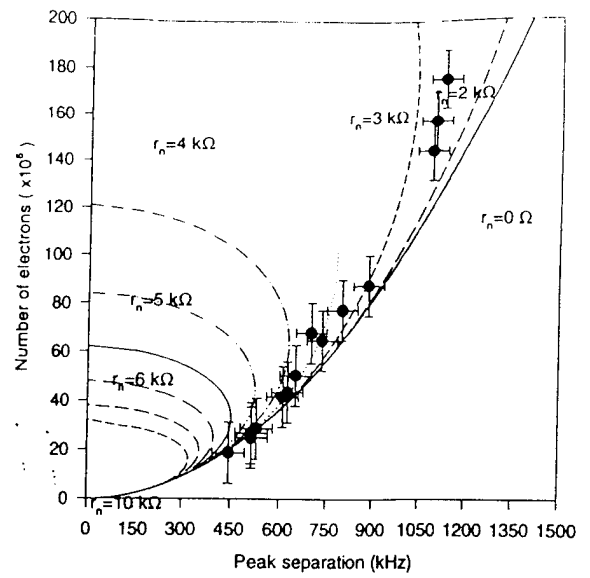


FIG. 5. The results of the numerical calculation of the separation of the two resonant peaks for different numbers of trapped electrons and different equivalent resistance. The experimental results are also shown. The dashed lines are from this work and the solid one shows the formula  $n = (\Delta\omega^2 l_s / \omega_z^2 L_e)$  for  $r_n=0$ .

From this expression we can see that the separation of the two resonant peaks increases with the number of trapped particles as long as the first term increasing faster than the last term. If  $r_n$  keeps constant with the increasing of the number of particles, this situation will be inverted and the separation is decreased. Finally when the first term is smaller than the last term these two peaks are merged together. This inverting point strongly depends on the equivalent resistance  $r_n$ . Numerically we found that at this inverting point the  $Q_{particle}$  was very small (for example when  $r_n=4$  k $\Omega$  and with our experimental parameters  $Q_{particle} \approx 10$ ) and so that the amplitudes of the two resonant peaks were very small and the linewidths of them were very broad.

We confirmed this relation by comparing it to the numerical results presented in Fig. 5 and found good agreement. In the case of  $r_n=0$  Eq. (3.3) gives  $(\Delta\omega/\omega)2 = nL_e/l_s$  which is the relation given in Ref. 4. Here we should point out that Eq. (3.3) is valid for all ranges of numbers of trapped particles and  $\Delta\omega$  is in fact the separation of the two maximum points on both sides of the central dip in the spectrum. When the number of trapped particles is too small the two parallel  $RCL$  resonant peaks can not be resolved, but due to the central series  $RCL$  resonant dip the separation of the two maximum points in the spectrum curve can still be used to deduce the number of trapped particles.

The equivalent resistance  $r_n$  is related to the damping of the CM motion of the trapped particles. Generally the damping rate  $\gamma'$  includes the contribution of the resistive cooling of the CM motion,<sup>7</sup> and the coupling of the CM motion to the internal mode motion which depends on the anharmonicity of the trapping field. With small numbers of trapped particles (i.e.,  $n < l_s/L_e Q_e^2$ ),  $r_n$  is dominated by the resistive cooling effect and can be expressed as  $R$ . In this case Eq. (3.3) can be simplified as

$$\left(\frac{\Delta\omega}{\omega_z}\right)^2 = 1.73 \frac{nL_e}{l_s} \left(1 - 0.122 \frac{nL_e Q_e^2}{l_s}\right)^2 \quad (3.4)$$

If  $n$  is much less than  $l_s/(L_e Q_e^2)$  this formula can be further simplified as

$$n = 0.58 \frac{l_s}{L_e} \left(\frac{\Delta\omega}{\omega_z}\right)^2 \quad (3.5)$$

Eqs. (3.4) and (3.5) are very useful to estimate the number of trapped particles when the number is not as large. With the trapping and electronics parameters used above, the restriction on  $l_s/L_e Q_e^2$  gives about  $10^5$  for electrons and  $10^8$  for protons and antiprotons.

$$n = \frac{l_s}{L_e} \left\{ \sqrt{\left[\left(\frac{\Delta\omega}{\omega_z}\right)^2 + \frac{1}{Q_{\text{particle}}^2}\right]^2 + \left(\frac{1}{Q_{\text{particle}}^2} + \frac{1}{Q_e Q_{\text{particle}}}\right)^2} - \left(\frac{1}{Q_{\text{particle}}^2} + \frac{1}{Q_e Q_{\text{particle}}}\right) \right\}, \quad (3.6)$$

where we remind that  $Q_e$  is the  $Q$  value of the external tank circuit. When  $Q_{\text{particle}} \gg \omega_z/(\Delta\omega)$  and  $\sqrt{Q_{\text{particle}} Q_e} \gg \frac{\omega_z}{\Delta\omega}$  this formula simplifies to  $n = (l_s/L_e)(\Delta\omega/\omega_z)^2$ .

#### IV. EXPERIMENTAL RESULTS

The trap used for these experiments was an open end-caps cylindrical Penning trap which has been used to catch antiprotons.<sup>3</sup> This Penning trap was immersed in a 3.8 T homogeneous magnetic field and thermally connected to the cryogenic bore of the superconducting magnet. The large cryosorption rate of the liquid-helium cooled walls maintained the vacuum inside the trap at a level believed to be at or below  $10^{-11}$  Torr. The trap was loaded with low energy secondary electrons produced when a 200 eV electron beam aligned along the  $z$  axis ionized the residual gas atoms which were temporarily released from an Al foil at one end of the trap as it was struck by the beam. The electrons were first trapped in the long anharmonic trap formed by the Al foil and an exit electrode which was designed for the future extraction experiments as shown in Fig. 6. Electrons lose energy very effectively by synchrotron radiation in the 3.8 T magnetic field and after a few minutes electron-electron collisions bring the plasma to thermal equilibrium with the ambient temperature, around 15 K. In this case the Debye

length with a plasma density  $n_0$  ( $\lambda_d = \sqrt{KT/4\pi n_0 q^2}$ ) is around  $40 \mu\text{m}$ , which is much smaller than the dimension of the cloud of electrons. This cold electron plasma can be modeled as a uniform density spheroid which rigidly rotates about the  $z$  axis with a sharp boundary at which the density drops to zero within a few Debye lengths.<sup>8</sup>

The trap voltage is adjusted so that the oscillation frequency of the CM motion of the cloud of electrons is coincident with the resonant frequency of the tank circuit. The impedance of the tank circuit incorporating the equivalent  $r_n c_n l_n$  circuit, which describes the dynamic behavior of the trapped electrons, can be expressed as in Eq. (3.2). The output of this circuit was coupled by a 10 PF capacitance to the input stage of a preamplifier which was at room temperature. Thus the noise of the preamplifier concealed the Johnson noise feature of the tank circuit at 15 K such that broadband white noise was applied to the tank circuit which was equivalent to raising the temperature of the resistance  $R$ . A

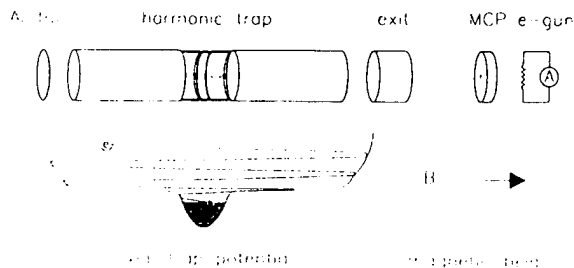


FIG. 6 Schematic illustration of the experimental setup

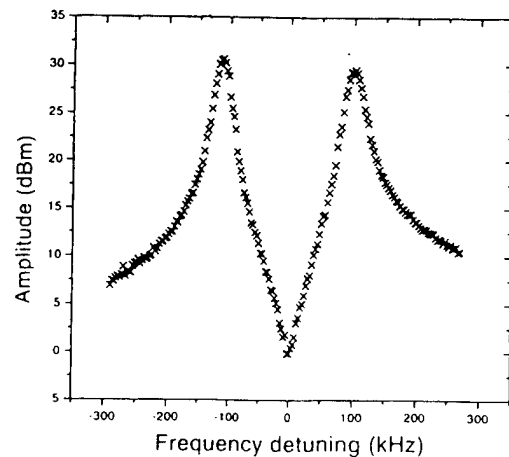


FIG. 7 A typical noise spectrum of the coupling of the external tank circuit with the CM motion of a cloud of electrons in our Penning trap. In this example the trap contained a few million electrons

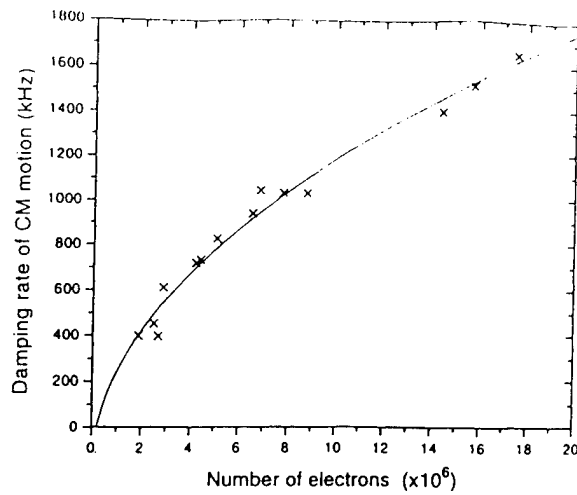


FIG. 8. The behaviour of the damping rate  $\gamma'$  for different numbers of trapped electrons. The solid line is fitted by the square root of the number of electrons.

HP8590B spectrum analyzer was used to collect the spectra of this noise.

The number of the stored electrons was controlled by changing the loading time and electron gun current. In the first 10 minutes after loading the separation of the two resonant peaks increased and the center of these two peaks shifted from lower frequency to the frequency of the oscillation of the CM motion of the trapped electrons when the density distribution of the electron plasma was concentrating in the central harmonic trap and they coupled to each other due to synchrotron radiation cooling and binary collisions. When the electrons reached thermal equilibrium with the ambient temperature this process stopped and a typical spectrum is shown in Fig. 7. The separation of the two peaks was measured and soon afterwards the electrons were dumped onto the Al foil and the number derived by measuring the charge accumulated on this foil with a Keithley electrometer. The results are shown, along with the calculation, in Fig. 5. It can be clearly seen that the divergence of the measured number of electrons from the value predicted from the formula  $^4 (\Delta\omega/\omega)^2 = nL_e/l_s$  increases when the number of trapped electrons is large. From the definition of  $r_n$  and Eq. (3.3) we get the damping rate  $\gamma'$  for different numbers of trapped electrons as shown in Fig. 8. From these data and the analysis in the last section we find that the damping rate increases approximately with the square root of the number of electrons. The damping rate was also increased when we pro-

duced a much larger electron cloud by shifting the electron gun off the trap axis. In this case the unharmonic terms of the trapping field made important contribution to the damping rate  $\gamma'$ . With the increase of the size of the electron cloud, the two resonant peaks became smaller and broader and finally could not be resolved by the spectrum analyzer. This phenomenon qualitatively agreed with our analysis in Section III where we discussed the spectra around the inverting point. The damping rate  $\gamma'$  is a direct measurement of the energy transfer rate from the CM motion to the external reservoir and the internal motion of trapped particles. More work is needed to study this in detail.

## V. CONCLUSIONS

In this paper the coupling of the CM motion of a cloud of particles trapped in a Penning trap to an externally connected tank circuit has been studied. Both the number of trapped particles and the damping of their CM motion play an important role in this process. These results give us a way to continuously, non-destructively and passively diagnose the number of trapped particles, which is valid for clouds of any number, and observe some of the dynamic characteristics of the CM motion.

## ACKNOWLEDGMENTS

We would like to thank J. Rochet for providing technical support during the construction and operation of the experiment and Dr. T. Otto for preparing the experiment in the early stages. X. F. is grateful for financial support from the Danish National Science Foundation. This work was partially supported by the US Department of Energy under contract W7405 ENG-36 and also by the U.S. Air Force Office of Scientific Research under Grant No. F49620-94-1-0223 (Pennsylvania State University) and Jet Propulsion Laboratory (U.S. National Aeronautics and Space Administration).

<sup>1</sup>G. Gabrielse, X. Fei, L. A. Orozco, R. L. Tjoelker, J. Haas, H. Kalinowsky, T. A. Trainor, and W. Kells, *Phys. Rev. Lett.* **65**, 1317 (1990).

<sup>2</sup>G. Gabrielse, D. Phillips, W. Quint, H. Kalinowsky, G. Rouleau, and W. Jhe, *Phys. Rev. Lett.* **74**, 3544 (1995).

<sup>3</sup>M. M. Nieto and M. H. Holzscneider, *Appl. Phys. B* **60**, 103 (1995).

<sup>4</sup>D. J. Wineland and H. G. Dehmelt, *J. Appl. Phys.* **46**, 919 (1975).

<sup>5</sup>G. Gabrielse, L. Haarsma, and S. L. Rolston, *Int. J. Mass Spectrom. Ion Processes* **88**, 319 (1989).

<sup>6</sup>W. J. Shockley, *J. Appl. Phys.* **9**, 635 (1938).

<sup>7</sup>If we consider the effect of resistive cooling of the CM motion in the  $z$  direction of a cloud of particles in a Penning trap as a dissipative force from a voltage between the two correction electrodes due to the induced current of a charged particle of mass  $nm$  and charge  $nq$ , the resistive cooling rate can be expressed as  $nd_1^2q^2R/4z_0^2m$  where  $R$  is the resistance in the external circuit.

<sup>8</sup>See, for example, S. A. Prasad and T. M. O'Neil, *Phys. Fluids* **22**, 278 (1979); T. M. O'Neil and C. F. Driscoll, *ibid.*, 266 (1979).

## Electromagnetic Implosion of Spherical Liner

J. H. Degnan, F. M. Lehr, J. D. Beason,\* G. P. Baca, D. E. Bell, A. L. Chesley, S. K. Coffey,<sup>†</sup> D. Dietz, D. B. Dunlap,<sup>‡</sup> S. E. Englert, T. J. Englert, D. G. Gale,<sup>‡</sup> J. D. Graham,<sup>‡</sup> J. J. Havranek, C. D. Holmberg, T. W. Hussey, R. A. Lewis,<sup>§</sup> C. A. Outten, R. E. Peterkin, Jr., D. W. Price, N. F. Roderick, E. L. Ruden, U. Shumlak, G. A. Smith,<sup>§</sup> and P. J. Turchi

High Energy Plasma Division, Phillips Laboratory, Kirtland Air Force Base, New Mexico 87117-5776

(Received 12 April 1994)

We have magnetically driven a tapered-thickness spherical aluminum shell implosion with a 12.5 MA axial discharge. The initially 4 cm radius, 0.1 to 0.2 cm thick,  $\pm 45^\circ$  latitude shell was imploded along conical electrodes. The implosion time was approximately 15  $\mu\text{sec}$ . Radiography indicated substantial agreement with 2D-MHD calculations. Such calculations for this experiment predict final inner-surface implosion velocity of 2.5 to 3 cm/ $\mu\text{sec}$ , peak pressure of 56 Mbar, and peak density of 16.8 g/cm<sup>3</sup> ( $>6$  times solid density). The principal experimental result is a demonstration of the feasibility of electromagnetic-driven spherical liner implosions in the cm/ $\mu\text{sec}$  regime.

PACS numbers: 52.55.Ez, 52.50.Lp

A crucial problem in the creation of high energy density matter is spherically symmetric implosions. Laser techniques become quite expensive at high total energy in the compressed matter. Electromagnetic implosions, on the other hand, require close control of solid state mechanics at high magnetic field values.

Fast solid density shell implosions, particularly in spherical geometry, may be used to obtain physical regimes of 10 to 100 Mbar pressures with 1 to 10 g masses in the laboratory. Such regimes can be useful for studies of equation of state of materials and for applications including magnetized target fusion [1]. We have previously worked on electromagnetically driven solid density shell implosions in cylindrical and conical geometry [2,3]. These experiments agreed well with two-dimensional magnetohydrodynamic (2D-MHD) calculations—which predicted aluminum liner compressions to 10 Mbar,  $3\times$  solid density. We now report on such an experiment in spherical geometry. The experimental results may be useful for comparison with three-dimensional instability theory.

Previous related work by others in cylindrical geometry included that by Alikhanov *et al.* [4], Eskov *et al.* [5], Petrukhin *et al.* [6], Chernyshev *et al.* [7], Turchi *et al.* [8], and Sherwood *et al.* [9]. The deformation of electromagnetically driven cylindrical shells into spheroidal shells has been discussed by Goloviznin *et al.* [10] and by Chernyshev *et al.* [11]. Mokhov discussed 2D-MHD calculations of a spheroidal shell liner driven by an explosive magnetic flux compression generator discharge. Its shape deformed to spherical during the implosion [12]. His publication also showed corroborating radiography from a reduced energy scaled experiment [12]. This achieved a 2 km/sec velocity inferred from comparison of radiography and calculations.

In the work reported here, we used a 12.5 MA, 4.8 MJ capacitor discharge, with current flowing in the polar direction through a spherical aluminum shell between conical electrodes, as illustrated in Fig. 1. This is the first

direct electromagnetically driven spherical liner implosion in the velocity range  $\gg 2$  km/sec. Radiography indicates  $\geq 7$  km/sec of the inner surface at 1  $\mu\text{sec}$  prior to peak compression. 2D-MHD calculations indicate that the liner's peak velocity exceeded 6 km/sec (depth average). The peak inner surface velocity predicted by those calculations is 25 km/sec. The result reported here is also the first example of an electromagnetically imploded liner with an initially spherical shape. The outer surface of the  $\pm 45^\circ$  shell is spherical, with 4.0 cm radius. The thickness is proportional to the cosecant squared of the polar angle as measured from the symmetry axis of the electrodes (colatitude). The thickness at the "equator" is 0.10 cm. Deviation of the actual shell thickness from the intended thickness vs polar angle was  $\leq 5\%$ . The mass was 49 g. The outer surface was polished to a mirror finish. This polar angle variation of thickness causes the ratio of magnetic pressure to shell areal mass density to be independent of polar angle, assuming no polar mass flow. Ideally, this enables the spherical shape to be maintained during the implosion.

To compensate for shell-electrode contact effects, the conical electrodes are overconverged by  $3^\circ$  each. That is, while the zero order design has  $45^\circ$  conical electrodes (whose projected vertices coincide at the origin of the electrode cylindrical coordinate system), the actual design has  $42^\circ$  (with respect to axis) conical electrodes. Their vertices project beyond the midplane from the respective

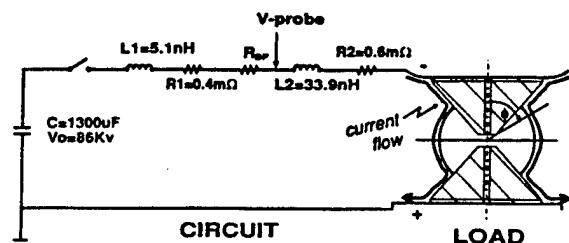


FIG. 1. Circuit diagram and load schematic.



electrodes. These electrodes are truncated at an axial distance of 1 cm from each other (0.5 cm from the origin).

The 1300  $\mu\text{F}$ , 120 kV, 9.4 MJ Shiva Star capacitor bank was used to drive the implosion discharge. The charge voltage and energy were 86 kV and 4.8 MJ. The initial inductance up to the outer surface of the spherical shell was 39 nH. Of this, 33 nH is in a very conservative design vacuum transmission line. This vacuum transmission line inductance can, in principle, be substantially reduced, enabling higher current, faster implosions. The series resistance was approximately 1 m $\Omega$  plus the resistance of a safety fuse [2,3]. This 94 cm long, 2.125 cm<sup>2</sup> cross section aluminum thermister/fuse limits peak discharge current and reversal in the event of an insulator or current feed failure. It has a small but non-negligible effect on a normal discharge. Its resistance during the time of interest ranges from 0.12 to  $\sim 0.5$  m $\Omega$ . The peak discharge current, measured by integrated inductive Rogowski and azimuthal magnetic probes, is  $12.5 \pm 0.5$  MA. The current rise time is 9  $\mu\text{sec}$ . The azimuthal magnetic probes indicated full current delivery in the vacuum section of the transmission line for 16  $\mu\text{sec}$  into the discharge. The vacuum chamber pressure was  $\sim 10^{-6}$  Torr prior to the discharge.

The principal experimental diagnostic was pulsed radiography, taken with 300 kV, 5 kA, and 30 nsec pulse driven x-ray tubes. The tubes have tungsten anodes (9.13° or 14.25° conical tips), carbon felt cathodes, and 3 mm anode-cathode coaxial gaps. They are normally damaged in such experiments, but readily refurbished. Only cylindrical radial views were used. The source to axis distance is 31.3 cm. The axis to film distance is 37.5 cm. The diagnostic x rays pass through a 0.64 cm thick, 10 cm radius cylindrical outer current conductor and through film pack shielding as well as through the spherical shell. The film pack shielding consists of 0.64 cm aluminum, 3.8 cm polyethylene, and 3.8 cm of low density foam. The film is DuPont NDT 57, with NDT 9 front and back screens. There were three x-ray tubes and film packs used on this experiment. Two were fired at 12.7  $\mu\text{sec}$  and one at 14  $\mu\text{sec}$  into the discharge. Collimation shielding and setup shots eliminated possible crosstalk complications. The earlier radiographs, taken with views 60° apart in azimuth, showed essentially identical images. X-ray pulser timing was confirmed using silicon *p-i-n* x-ray detectors.

Radiographs of the implosion taken at  $t = 0, 12.7$ , and 14  $\mu\text{sec}$  into the discharge are shown in Figs. 2 and 3. Also shown are 2D-MHD calculated contours of the inner and outer liner surface. This same calculation was used to generate synthetic radiographs for qualitative comparison with experimental ones. There is good agreement on the experimental and calculated shapes, locations, and timing.

The radiographs show some evidence of short ( $\sim \text{mm}$ ) and long ( $\sim \text{cm}$ ) wavelength nonuniformities. These do not appear to threaten the integrity of the imploding shell. These nonuniformities may be Rayleigh-Taylor instabilities of liquid and plastic portions of the liner.

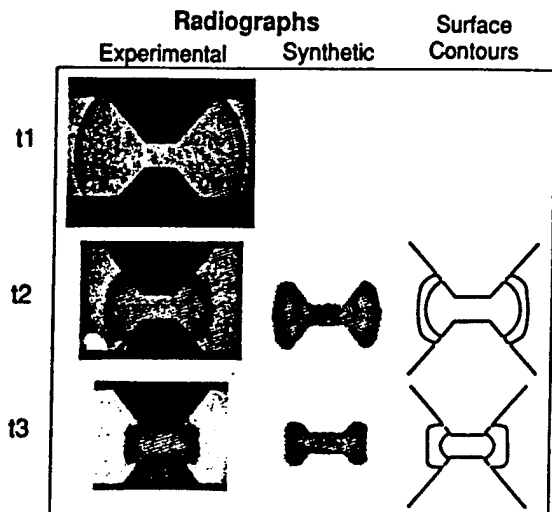


FIG. 2. Radiographs (at  $t_1, t_2, t_3 = 0, 12.7, 14 \mu\text{sec}$ ), 2D-MHD (at  $t_2, t_3 = 12.7, 14 \mu\text{sec}$ ) comparison.

They will be discussed at greater length in a separate paper, for both cylindrical and spherical geometry. The 12.7  $\mu\text{sec}$  radiographs (one shown here) were taken with the sharper 9.13° anode x-ray tubes, which are higher resolution. This may be why the shorter wavelength nonuniformities are more evident than on the 14  $\mu\text{sec}$  radiograph.

The 2D-MHD calculations were done using the CALE code [13,14]. We used version 930313 of this code, with the Steinberg-Guinan elastic-plastic strength model and a 4-phase equation of state for aluminum. We ran this arbitrary Lagrangian-Eulerian (ALE) code in Eulerian mode for  $\sim 1300$  cycles, with 25 axial  $\times$  75 radial zones.

The 2D-MHD calculated synthetic radiographs assume 300 keV monoenergetic x rays and linear film response. The displayed intensities are proportional to chordal path integrals of density times opacity. They may be a more useful comparison to the experimental radiographs than the surface or density contour plots, at least until more complete analysis of the experimental radiographs is accomplished. It should be noted that the experimental radiographs are obtained with a distributed rather than a monoenergetic x-ray spectrum and with nonlinear rather than linear film response. Thus, one expects the synthetic



FIG. 3. Blowup of  $t = 14 \mu\text{sec}$  experimental (left) and synthetic (right) radiographs.

radiographs to be an inexact but useful simulation of the experimental radiographs. Good quantitative agreement on shape and symmetry and qualitative agreement on density distribution between synthetic and experimental radiographs are evident.

There is no substantial deviation of the shape of the outer liner surface from spherical either observed or calculated until late in the implosion ( $t > 12.7 \mu\text{sec}$ ,  $r < 2.3 \text{ cm}$ ). The deviation from spherical shape of the outer surface that then occurs is initially consistent with an approximately incompressible liner material. The liner parameters were chosen so that resistive heating would not cause bulk vaporization prior to the liner reaching the axis. Thus, the bulk of the liner material should be solid (albeit plastically deformed) or liquid prior to self-stagnation. If the liner were incompressible and there were no polar mass flow, the outer surface would not implode to a radius less than 1.67 cm at the "equator," nor to a radius less than 2.1 cm at the electrode polar angle. That is, in this approximation,  $r_2^3 - r_1^3 = K_0 \csc^2 \phi$ , where  $K_0 = r_{20}^3 - r_{10}^3$ , and  $r_{20}, r_{10}$  are the initial outer and inner radii at the equator.

The radius of the liner can be estimated from the circuit inductance. In a low impedance discharge such as this,  $L_p$  vs  $t$  is obtained from the experimental current  $I$  and voltage  $V_p$  vs  $t$ .  $V_p$  is the voltage measured at the (capacitive) voltage probe location, 33.9 nH from the initial liner outer surface position (cf. Fig. 1). We assume that the initial voltage at this position is the inductance ratio (33.9/39) times the charge voltage (86 kV), that is, 75 kV. ( $L_p$  is initially 33.9 nH.) The resistance past the voltage probe,  $R_2$ , is approximately 0.6 m $\Omega$  and assumed constant. This assumption may be incorrect by  $\sim 0.1 \text{ m}\Omega$  over the time of interest.  $L_p$  vs  $t$  is then obtained in the standard way:

$$L_p = \frac{1}{I} \int_0^t (V_p - IR_2) dt. \quad (1)$$

For self-similar implosion geometry (i.e., electrodes not overconverged), the current radius  $r_c$  vs  $t$  is related to  $L_p$  vs  $t$  by

$$\begin{aligned} \Delta L_p &= L_p - L_{p0} \\ &= \frac{1}{I} \int B dA \\ &= 2 \left( \frac{\mu_0}{2\pi} \right) \int_{r_c}^{r_0} \int_{\phi_m}^{\pi/2} \frac{r d\phi dr}{r \sin \phi} \\ &= \frac{\mu_0}{\pi} (r_0 - r_c) \left[ -\ln \left( \tan \frac{\phi_m}{2} \right) \right] \\ &= \frac{\mu_0 g}{\pi} (r_0 - r_c), \end{aligned} \quad (2)$$

where  $\phi_m$  is the (colatitude) polar angle of the electrode,  $r_0$  is the initial outer (spherical) current radius (presumably equal to initial outer liner radius), and  $\mu_0$  is the magnetic permeability  $= 4\pi \times 10^{-7} \text{ H/m}$ . The geometry factor  $g = 0.881$  when  $\phi_m = 45^\circ$ . The relation is slightly more complicated for overconverged electrodes.

In principle, this analysis gives the current radius vs time. In practice, the errors can be large, with uncertainty in  $R_2$  the major source of error. A reasonable value of  $R_2$  (0.6 m $\Omega$ ) gives reasonable  $r_c$  vs  $t$ . Equation (2) is also used to calculate the increasing load inductance (and its derivative  $dL/dt$ ) in the modeling of the capacitor discharge driving the implosion. In this use, the total series resistance matters, but the calculation is not sensitive to the relative portion of the total resistance past the voltage probe. A comparison of the experimental (spherical) current radius vs time with the 2D-MHD calculated inner and outer liner (spherical) radius  $r$  vs time  $t$  is shown in Fig. 4. Since the shape deviates from spherical once the incompressible limiting radius at the electrode polar angle is reached, the calculated  $r$  vs  $t$  is shown for a given polar angle ( $\phi = 90^\circ$  equator). This current radius should correspond more to the outer liner radius than to the inner radius, and this is evident in Fig. 4. In the limit of full diffusion of the current throughout the liner thickness, the current radius would correspond to the mean liner radius. 2D-MHD calculations indicate that this current is predominantly limited to the outer 20% of the liner thickness. The more reliable radiography data points are also shown on this plot.

The degree of agreement between experimental and 2D-MHD calculated results encourages us to extend the 2D-MHD predictions through peak compression. Some principal results for a calculation for this experiment are shown in Fig. 5. These indicate that a large portion of the liner mass is compressed to greater than twice solid density, and on the order of  $10^{-2} \text{ g}$  is compressed to  $\sim 6\times$  solid density, 56 Mbar. The predicted inner surface implosion velocity reaches 2.5 to 3 cm/ $\mu\text{sec}$  at a radius of 0.2 cm. The predicted peak implosion kinetic energy is  $\sim 1 \text{ MJ}$ .

Similar calculations with less conservative electrodes (not overconverged) indicate more distortion of the liner near the electrode, but not enough to cause liner-electrode

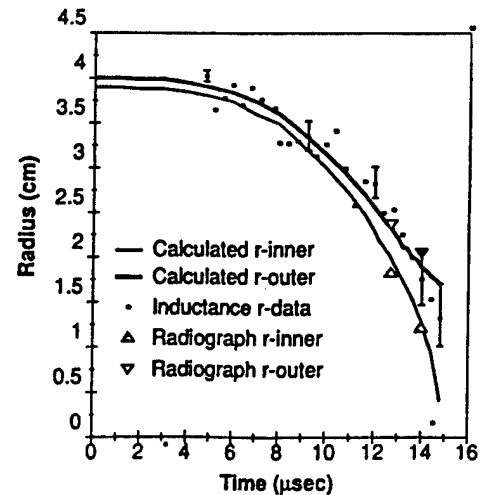


FIG. 4. Calculated, experimental  $r$  vs  $t$ . Error bars are for  $\pm 0.1 \text{ m}\Omega$  tolerance on series resistance  $R_2$  past voltage probe.

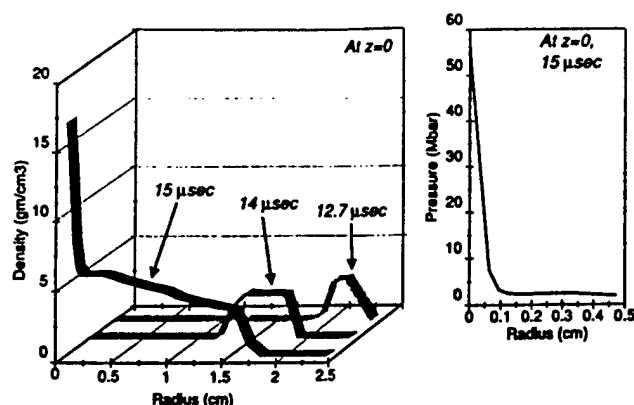


FIG. 5. 2D-MHD calculated density ( $\rho$ ) vs  $r$  at  $z = 0$  for 12.7, 14.0, and 15.0  $\mu\text{sec}$ . 2D-MHD calculated pressure ( $p$ ) vs  $r$  at  $z = 0$  for peak compression (15.0  $\mu\text{sec}$ ).

detachment. Such calculations indicate higher peak compressions,  $\sim 90$  Mbar.

In summary, we have experimentally demonstrated the feasibility of imploding spherical liners with (cylindrically symmetric) magnetic field pressure. This is a basis for creating high energy density matter at high total energy. Experimental results substantially agree with 2D-MHD simulations. Such simulations predict  $>50$  Mbar peak compressions. The degree of agreement with 2D-MHD simulation suggests that three-dimensional instability effects are small.

This research was supported by the Air Force Office of Scientific Research. We would like to acknowledge the support and interest of Dr. W. L. Baker, Dr. B. Godfrey, Dr. R. Kelley, Dr. G. Kiuttu, and Dr. H. Wittmann.

\*Present address: US Air Force Academy, Colorado Springs, CO.

†Present address: Physical Sciences, Inc., Alexandria, VA.

‡Present address: Maxwell Laboratories, Inc., Albuquerque, NM.

§Present address: Pennsylvania State University, State

College, PA.

- [1] I. Lindemuth and R. Kirkpatrick, Nucl. Fusion 23, 263 (1983).
- [2] J. Degnan *et al.*, in *Megagauss Technology and Pulsed Power Applications*, Fourth International Conference on Megagauss Magnetic Field Generation and Related Topics, edited by C. Fowler, R. Caird, and D. Erickson (Plenum Press, New York, NY, 1987), pp. 699–706.
- [3] J. Degnan *et al.*, in *Megagauss Fields and Pulsed Power Systems*, Fifth International Conference on Megagauss Magnetic Field Generation and Related Topics, edited by V. Titov and G. Shvetsov (Nova Science Publishers, Inc., New York, NY, 1990), pp. 623–630.
- [4] S. Alikhanov, V. Bakhtin, and D. Toporkov, in *Ultrahigh Magnetic Fields-Physics, Techniques, Applications*, Third International Conference on Megagauss Magnetic Field Generation and Related Topics, edited by V. Titov and G. Shvetsov (Nauka, Moscow, 1984), p. 213.
- [5] A. Eskov, M. Kitayev, and R. Kurtmullayev, in *Ultrahigh Magnetic Fields-Physics, Techniques, Applications* (see Ref. [4]), p. 204.
- [6] A. Petrukhin *et al.*, in *Ultrahigh Magnetic Fields-Physics, Techniques, Applications* (see Ref. [4]), p. 406.
- [7] V. Chernyshev *et al.*, in *Megagauss Technology and Pulsed Power Applications* (see Ref. [2]), pp. 707–712.
- [8] P. Turchi *et al.*, in *Megagauss Physics and Technology*, Second International Conference on Megagauss Magnetic Field Generation and Related Topics, edited by P. Turchi (Plenum Press, New York, NY, 1980), p. 375.
- [9] A. Sherwood *et al.*, in *Megagauss Physics and Technology* (see Ref. [8]), pp. 391–398.
- [10] V. Goloviznin *et al.*, in *Megagauss Physics and Technology* (see Ref. [8]), p. 415.
- [11] V. Chernyshev *et al.*, in "Sixth International Conference on Megagauss Magnetic Field Generation and Related Topics," edited by M. Cowan and R. Spielman (Nova Science Publishers, Inc., Commack, NY, to be published).
- [12] V. Mokhov *et al.*, Sov. Phys. Dokl. 24, 557 (1979).
- [13] R. Tipton, in *Megagauss Technology and Pulsed Power Applications* (see Ref. [2]), p. 299.
- [14] R. Tipton, *CALE Users Manual* (Lawrence Livermore National Laboratory, Livermore, CA, 1990).



### INTEROFFICE CORRESPONDENCE

Intellectual Property Office  
113 Technology Center

Date: May 16, 1996  
From: D.R. Paterson *[Signature]*  
To: G.A. Smith  
Subject: "Portable Antiproton Radioisotope Generator (PARG)"  
By G.A. Smith  
PSU Invention Disclosure No. 96-1604

This memorandum is to formally acknowledge receipt of the subject invention disclosure. The disclosure is assigned file number 96-1604. To avoid confusion with future invention disclosures you may submit to our office, please use this number in future communications. We forwarded the original Invention Disclosure form to R.C. Meyer for signature.

According to the information contained in the disclosure, a manuscript was published in *Hyperfine Interactions* in 1993, and a presentation is scheduled for June 16-20, 1996 at the 1996 Annual Meeting of the *American Nuclear Society*. If the material published/presented is enabling (i.e. could a person skilled in the art duplicate the invention based on the material you presented/submitted), please consult with me before presenting the information and we can determine how the information relates directly to the subject invention. As you are aware, the ability to obtain patent rights and to maximize the commercial potential of the invention may be compromised by publication or public disclosure.

It is noted that the invention was made with sponsorship from AFOSR Grant No. F49620-94-1-0223 and JPL Contract No. 958301.

Please contact us if you have any questions related to this invention or other matters relating to intellectual property.

DRP/clw

c: R.C. Meyer